NOVA SCHOOL OF SCIENCE & TECHNOLOGY

DEPARTMENT OF MECHANICAL AND INDUSTRIAL ENGINEERING

A COMPUTATIONAL AND DEEP LEARNING FRAMEWORK FOR FLUID-STRUCTURE INTERACTION IN ASCENDING THORACIC AORTIC ANEURYSMS

ANDRÉ FILIPE GERALDES MOURATO

Master in Mechanical Engineering

DOCTORATE IN MECHANICAL ENGINEERING

NOVA University Lisbon
September, 2025

NOVA SCHOOL OF SCIENCE & TECHNOLOGY

DEPARTMENT OF MECHANICAL AND INDUSTRIAL ENGINEERING

A COMPUTATIONAL AND DEEP LEARNING FRAMEWORK FOR FLUID-STRUCTURE INTERACTION IN ASCENDING THORACIC AORTIC ANEURYSMS

ANDRÉ FILIPE GERALDES MOURATO

Master in Mechanical Engineering

Supervisor: José Manuel Cardoso Xavier
Associate Professor, Faculdade de Ciências e Tecnologia, Universidade NOVA de Lisboa

Co-supervisors: Moisés Gonçalves de Brito
Assistant Professor, Faculdade de Ciências e Tecnologia, Universidade NOVA de Lisboa

José Inácio Guerra Fragata
Full Professor, Faculdade de Ciências Médicas, Universidade NOVA de Lisboa

Examination Committee

Chair: Virgílio António Cruz Machado
Full Professor, Faculdade de Ciências e Tecnologia, Universidade NOVA de Lisboa

Rapporteurs: Nele Famaey
Associate Professor, Katholieke Universiteit Leuven

Ana Paula Betencourt Martins Amaro
Associate Professor with Habilitation, Faculdade de Ciências e Tecnologia, Universidade de Coimbra

Supervisor: José Manuel Cardoso Xavier
Associate Professor, Faculdade de Ciências e Tecnologia, Universidade NOVA de Lisboa

Members: Marco Paulo Lages Parente
Associate Professor, Faculdade de Engenharia, Universidade do Porto

Telmo Jorges Gomes dos Santos
Full Professor, Faculdade de Ciências e Tecnologia, Universidade NOVA de Lisboa

Pedro Nuno Martins Pires Coelho
Assistant Professor, Faculdade de Ciências Médicas, Universidade NOVA de Lisboa

DOCTORATE IN MECHANICAL ENGINEERING

NOVA University Lisbon
September, 2025

A Computational and Deep Learning Framework for Fluid-Structure Interaction in Ascending Thoracic Aortic Aneurysms

Copyright © André Filipe Geraldes Mourato, NOVA School of Science and Technology, NOVA University Lisbon.
The NOVA School of Science and Technology and the NOVA University Lisbon have the right, perpetual and without geographical boundaries, to file and publish this dissertation through printed copies reproduced on paper or on digital form, or by any other means known or that may be invented, and to disseminate through scientific repositories and admit its copying and distribution for non-commercial, educational or research purposes, as long as credit is given to the author and editor.

This document was created with the (pdf/Xe/Lua)LaTeX processor and the NOVAthesis template (v7.3.9) [1].

This thesis is dedicated to my family, friends, and colleagues who have supported me throughout my academic journey.

Acknowledgements

It is with great satisfaction that I present this work, the culmination of an almost five-year journey at *Universidade Nova de Lisboa, Faculdade de Ciências e Tecnologia*. This marks the closing of a very important chapter in my life, one that I will always remember with great fondness. Over this time, I have grown both personally and academically, and the following lines aim to express my heartfelt gratitude to all those who have contributed to the successful completion of my PhD thesis.

I would like to express my deepest gratitude to my advisors, *Prof. José Xavier*, *Prof. Moisés Brito*, and *Prof. José Fragata*, for their invaluable guidance, support, and encouragement throughout this journey. Their expertise and insights were instrumental in shaping my research and in helping me overcome the many challenges a PhD poses. I also extend my sincere thanks to *Dr. António Cruz Tomás* for his support in bringing a valuable clinical perspective to my work.

My appreciation also goes to the *AneurysmTool* project (DOI: 10.54499/PTDC/EMD-EMD/1230/2021), which gave me the opportunity to travel across Europe, participate in scientific congresses and summer schools, and meet like-minded people, all of which contributed greatly to my professional growth. I am grateful as well to my PhD scholarship (DOI: 10.54499/UI/BD/151212/2021) funded by the *Fundação para a Ciência e Tecnologia*, which supported my research, allowed me to focus entirely on my studies without financial concerns, and enabled me to spend time abroad. A word of thanks also to *Unidade de Investigação e Desenvolvimento em Engenharia Mecânica e Industrial* and to *Departamento de Engenharia Mecânica e Industrial* for providing the resources and support essential to developing my research.

A highlight of this journey was spending nearly six months at *École des Mines de Saint-Étienne, Sainbiose U1059*, under the supervision of *Prof. Stéphane Avril*. This period was crucial for my growth as a researcher; I had the privilege of observing up close how science is conducted at a renowned European research center. I also met incredible people whose insights enriched my work. I am grateful to the *Institut Français du Portugal* for funding a one-month stay in Saint-Étienne, which complemented this experience.

I also want to thank my PhD colleagues for the many experiences we shared — from Figueira da Foz to Maastricht — for the stimulating discussions about work and much more, and for their patience and camaraderie. Thank you, *Rodrigo Valente*, for the many conversations and shared moments; *Francisco Bernardo*, for your company during the long

hours in our "basement" and for your valuable insights; *Cláudia Almeida* and *Pedro Rendas*, for your friendship, which will always hold a special place in my heart. I also thank *Rafael Louro* and *Sofia Candeias* for the opportunity to assist in their master's thesis work.

Before moving on to my personal acknowledgments, I would like to recognize some professors who have marked my academic journey from my earliest school years through to my master's degree in mechanical engineering: my deepest gratitude to *Prof. Ana Alves*, *Prof. Ruy Costa*, and *Prof. Luis Gil*.

Finally, my most profound thanks go to my family, my parents, brother, uncle, aunt, and grandparents, for their unwavering support and love throughout this journey. To my dearest friends, *Rafaela, Francisco, Pedro F., A. Cavaco, Catarina, Mariana, Iris*, and *Pedro*, thank you for always being there for me, for the laughter, encouragement, and wonderful moments we shared; and to *Sara Fernandes*, who has been by my side for most of these past five years: thank you for your love, patience, and constant support. I am, and will always be, deeply grateful to you.

To all those who, in one way or another, contributed to the success of this work, I offer my sincere thanks. Your support and encouragement have been invaluable to me.

”

“You should enjoy the little detours to the fullest. Because that’s where you’ll find the things more important than what you want.”

— Ging Freecs, Hunter x Hunter
(Fictional Character)

Abstract

According to the World Health Organization (WHO), cardiovascular diseases are the leading cause of death worldwide. Among them, Ascending Thoracic Aortic Aneurysms (ATAAs) have an incidence of 6-10 per 100,000 people per year. Their progression is usually asymptomatic and may lead to fatal events, such as rupture or dissection. Clinical guidelines rely on a geometric criterion to assess risk, but this often fails to predict rupture accurately for all patients, highlighting the need for more robust diagnostic tools.

Numerical models have emerged as a promising tool to support the diagnosis and treatment of ATAAs. Simulating the behaviour of complex systems enables the development of patient-specific virtualizations, providing additional information for clinical decision-making. The literature highlights several approaches, with Computational Fluid Dynamics (CFD), Computational Solid Mechanics (CSM), and Fluid-Structure Interaction (FSI) being the most common. Among these, FSI is considered the *gold standard*. However, its clinical use remains limited due to: (i) the difficulty of building fully patient-specific models; (ii) high computational cost; and (iii) lack of validation against robust datasets.

This thesis addresses the second limitation by asking: "Which numerical approaches offer the best trade-off between accuracy and computational cost?". First, the impact of different prestressing methods in FSI simulations was evaluated. Then, FSI results were compared with more straightforward approaches. Finally, a surrogate model of aortic wall mechanics was developed by combining Deep Neural Networks (DNNs) with CSM simulations.

The aortic wall remains under stress throughout the cardiac cycle. Therefore, its reference configuration is not directly available in medical images. To overcome this, algorithms such as *Zero Pressure Geometry* (ZPG) and *Prestress Tensor* (PT) are commonly used. PT produced pressure fields consistent with ZPG but estimated a stiffer mechanical response. Incorporating regional material properties improved agreement with ZPG in terms of maximum stresses and strains.

As ATAA progresses and stiffness increases, the relevance of FSI decreases. Simpler approaches, such as Reduced Order Models (ROM) and CSM, become suitable alternatives due to their lower computational cost. All methods produced similar pressure fields. However, for estimating Wall Shear Stress (WSS), FSI remained the most reliable. For wall mechanics, coupling CSM with boundary conditions derived from ROM yielded results close to FSI.

Surrogate models have been proposed to reduce the computational burden of simulations. Artificial Intelligence (AI)-based methods have shown promising results in biomechanical modeling. In this work, a DNN was successfully trained using CSM simulation data. The model received as input information on aneurysm anatomy, material properties, and pressure fields, and was able to predict the spatial distribution of stresses and strains with an accuracy above 90 %.

The results of this thesis contribute to bridging the gap between biomechanical modeling and clinical practice. By comparing numerical strategies and introducing efficient *frameworks*, this work identifies potential solutions for integrating patient-specific biomechanical analysis into clinical workflows. The proposed methodologies may improve risk stratification and treatment planning of ATAAs, supporting a more personalized cardiovascular approach.

Keywords: Ascending Thoracic Aortic Aneurysm (ATAA), Deep Neural Networks (DNN), Fluid-Structure Interaction (FSI), Surrogate model, Tissue prestressing

Resumo

De acordo com a Organização Mundial da Saúde (WHO), as doenças cardiovasculares são a principal causa de morte no mundo. Entre estas, os Aneurismas da Aorta Torácica Ascendente (ATAAs) têm uma incidência de 6-10 por 100000 pessoas por ano. A progressão é geralmente assintomática e pode originar eventos fatais, como a rutura ou disseção. As diretrizes clínicas recorrem a um critério geométrico para avaliar o risco, mas este falha em prever com precisão a rutura em todos os pacientes, evidenciando a necessidade de ferramentas de diagnóstico mais robustas.

Modelos numéricos surgiram como uma solução promissora para apoiar o diagnóstico e tratamento de ATAA. A simulação do comportamento de sistemas complexos permite criar virtualizações específicas do paciente, oferecendo informação adicional para a decisão clínica. A literatura mostra várias abordagens, destacando-se Dinâmica dos Fluídos Computacional (CFD), Mecânica dos Sólidos Computacional (CSM) e Interação Fluído-Estrutura (FSI). Entre estas, FSI é considerada o *gold standard*. Contudo, a sua aplicação clínica é limitada por três fatores: (i) dificuldade em obter modelos totalmente específicos do paciente; (ii) tempos de computação elevados; e (iii) falta de validação contra bases de dados robustas.

Esta tese aborda a segunda limitação, investigando: "Quais são as abordagens numéricas que oferecem melhor compromisso entre precisão e custo computacional?". Inicialmente, avaliou-se o impacto de diferentes metodologias de pré-tensão em simulações FSI. Depois, os resultados de FSI foram comparados com abordagens mais leves. Por fim, foi desenvolvido um modelo substituto da mecânica da parede da aorta, combinando Redes Neuronais Profundas (DNNs) e simulações CSM.

A parede da aorta encontra-se sobre tensão ao longo do ciclo cardíaco. Assim, a configuração de referência não é observável em imagens médicas. Para ultrapassar esta limitação usam-se algoritmos como *Zero Pressure Geometry* (ZPG) e *Prestress Tensor* (PT). O uso de PT produziu campos de pressão semelhantes a ZPG, mas estimou uma resposta mais rígida da parede. A introdução de propriedades regionais melhorou a concordância com ZPG em termos de tensão e extensão máximas.

À medida que o ATAA progride e a rigidez aumenta, a relevância da FSI diminui. Abordagens mais simples, como Modelos de Ordem Reduzida (ROM) e CSM, tornam-se alternativas adequadas pelo menor custo computacional. Todas estas produziram campos de pressão semelhantes. No entanto, para estimar as Tensões de Corte na Parede (WSS),

FSI manteve-se a melhor opção. Para a resposta mecânica da parede, acoplar CSM com condições de fronteira de ROM gerou resultados próximos de FSI.

Modelos substitutos têm sido propostos para reduzir custos de simulação. Abordagens de Inteligência Artificial (AI) têm mostrado bons resultados na modelação biomecânica. Neste trabalho, foi treinado um modelo baseado numa DNN com dados de simulações CSM. O modelo recebeu como entrada informações sobre anatomia, propriedades materiais e campo de pressões, prevendo a distribuição espacial de tensões e extensões com uma taxa de acerto superior a 90 %.

Os resultados contribuem para aproximar a modelação biomecânica da prática clínica. Através da comparação de estratégias numéricas e da introdução de *frameworks* eficientes, identificam-se soluções para integrar a análise específica do paciente em fluxos clínicos. As metodologias propostas têm potencial para melhorar a estratificação do risco e o planeamento do tratamento de ATAA, apoiando uma abordagem mais personalizada.

Palavras-chave: Aneurisma na Aorta Torácica Ascendente (ATAA), Interação Fluido-Estrutura (FSI), Modelo substituto, Pré-tensão do tecido, Redes Neuronais Profundas (DNN)

Contents

List of Figures

List of Tables

Acronyms

AAA Abdominal Aorta Aneurysm *(p. 29)*
ACC American College of Cardiology *(p. 2)*
AD Aortic Dissection *(p. 29)*
AHA American Heart Association *(p. 2)*
AI Artificial Intelligence *(p. 4)*
ALE Arbitrary Lagrangian-Eulerian *(p. 57)*
ANN Artificial Neural Networks *(p. 93)*
ATAA Ascending Thoracic Aortic Aneurysm *(p. 2)*
AV Aortic Valve *(p. 33)*

BAV Bicuspid Aortic Valve *(p. 2)*
BC Boundary Condition *(p. 32)*

CFD Computational Fluid Dynamics *(p. 4)*
CSM Computational Solid Mechanics *(p. 4)*
CT Computed Tomography *(p. 32)*
CTA Computed Tomography Angiography *(p. 54)*
CVD CardioVascular Disease *(p. 27)*

DNN Deep Neural Network *(p. 4)*
DNS Direct Numerical Simulations *(p. 44)*
DTAA Descending Thoracic Aortic Aneurysm *(p. 34)*

ECM ExtraCellular Matrix *(p. 17)*
ESC European Society of Cardiology *(p. 2)*

FCT Fundação para a Ciência e Tecnologia *(p. 4)*
FDM Finite Difference Method *(p. 31)*
FEM Finite Element Method *(p. 3)*
FIESTA Fast Imaging Employing Steady-state Acquisition *(p. 55)*
FL False Lumen *(p. 35)*
FSI Fluid-Structure Interaction *(p. 3)*

FVM Finite Volume Method *(p. 3)*

ICP Iterative Closest Point *(p. 95)*

LES Large Eddy Simulations *(p. 41)*

ML Machine Learning *(p. 27)*
MLU Media Lamellar Units *(p. 17)*
MMP Matrix MetalloProteinase *(p. 19)*
MRI Magnetic Resonance Imaging *(p. 16)*

OSI Oscillatory Shear Index *(p. 34)*

PCA Principal Component Analysis *(p. 93)*
PRISMA Preferred Reporting Items for Systematic Reviews and Meta-Analyses *(p. 4)*
PT Prestress Tensor *(p. 4)*
PWS Peak Wall Stress *(p. 34)*
PWV Pulse Wave Velocity *(p. 32)*

RANS Reynolds-Averaged Navier-Stokes *(p. 41)*
RLBM Regularized Lattice Boltzman Method *(p. 31)*
ROM Reduced Order Model *(p. 4)*
RPIM Radial Point Interpolation Method *(p. 32)*
RRT Relative Residence Time *(p. 66)*

SP Source Points *(p. 95)*
SPH Smoothed Particle Hydrodynamics *(p. 27)*
SSM Statistical Shape Model *(p. 95)*
STJ Sinotubular Junction *(p. 33)*

TAA Thoracic Aorta Aneurysm *(p. 2)*
TAV Tricuspid Aortic Valve *(p. 94)*
TAWSS Time-Averaged Wall Shear Stress *(p. 36)*
TL True Lumen *(p. 35)*

VFM Virtual Flux Method *(p. 32)*
VSMC Vascular Smooth Muscle Cell *(p. 17)*

WHO World Health Organization *(p. 2)*
WS Wall Stress *(p. 27)*

WSS Wall Shear Stress *(p. 17)*

XFEM Extended Finite Element Method *(p. 31)*

ZPG Zero Pressure Geometry *(p. 5)*

Symbols

A_0	Initial cross-sectional area *(p. 64)*
A^k	Distance based score *(p. 61)*
α	Transition coefficient from low to high shear rates *(p. 14)*
$\boldsymbol{C}$	Right Cauchy-Green strain *(p. 21)*
C	Artery compliance *(p. 61)*
$\hat{\partial}_t$	Arbitrary Lagrangian-Eulerian time derivative *(p. 57)*
$E_{CAL}{}^j$	Subdomain Young's modulus *(p. 64)*
E_s	Young's modulus *(p. 58)*
E_T	Tangential Young's modulus *(p. 65)*
$\boldsymbol{F}$	Deformation gradient *(p. 58)*
$\vec{F}$	Force *(p. 64)*
$\dot{\gamma}$	Shear rate *(p. 14)*
ε'	Green-St. Venant strain *(p. 64)*
H	Hematocrit *(p. 15)*
$\boldsymbol{I}$	Identity tensor *(p. 58)*
Γ	Fluid-solid interface *(p. 59)*
$\boldsymbol{J}$	Jacobian matrix *(p. 58)*
k	Reversed displacement algorithm parameter *(p. 61)*
κ_s	Bulk modulus *(p. 58)*
σ'	Kirchhoff stress *(p. 64)*
λ	Stretch *(p. 64)*

μ Fluid viscosity *(p. 14)*
μ_0 Viscosity at low shear rate *(p. 14)*
μ_∞ Viscosity at high shear rate *(p. 14)*
μ_p Plasma viscosity *(p. 15)*
μ^s Second Lamé parameter *(p. 21)*

n Power law constant *(p. 14)*
$\hat{\boldsymbol{n}}$ Unit normal vector *(p. 59)*
∇ Gradient operator *(p. 57)*

Ω_f Fluid domain *(p. 57)*
Ω_{im} Image domain *(p. 62)*
Ω_s^j Solid subdomain *(p. 64)*

p Pressure *(p. 57)*
P_{dia} Diastolic hemodynamic loads *(p. 61)*
ν_s Poisson ratio *(p. 58)*

R Pearson's correlation coefficient *(p. 65)*
R^2 Linear correlation coefficient *(p. 67)*
ρ_f Blood density *(p. 14)*
ρ_s Aortic wall density *(p. 58)*
R_p Resistance of smaller arteries and arterioles *(p. 61)*
R_s Resistance of larger caliber arteries *(p. 61)*

$\boldsymbol{S}$ Second Piola-Kirchhoff stress tensor *(p. 58)*
$\boldsymbol{S}_0$ Prestress tensor *(p. 62)*
$\boldsymbol{\sigma}$ Cauchy stress tensor *(p. 57)*
$\overline{\sigma_P}$ Principal stresses average *(p. 64)*
s Standard deviation *(p. 98)*

t Time *(p. 58)*
τ_0 Stress limit for rouleaux formation *(p. 14)*
Γ' Time costant *(p. 14)*
ε User-defined tolerance *(p. 61)*

$\boldsymbol{u}$ Displacement field *(p. 58)*
$\mathbf{U}$ Reference displacement field *(p. 61)*

$\boldsymbol{v}$ Fluid velocity *(p. 57)*

$\boldsymbol{W}$ Strain energy density function *(p. 20)*
$\boldsymbol{w}$ Grid velocity *(p. 57)*

$\boldsymbol{X}$ Reference configuration *(p. 58)*
$\boldsymbol{X}_{0k}$ Candidate reference configuration *(p. 61)*
$\boldsymbol{x}_{0k}$ Candidate reference deformed configuration *(p. 61)*
$\boldsymbol{X}_{\text{im}}$ Image configuration *(p. 61)*
$\boldsymbol{x}_{\text{im}}$ Deformed image configuration *(p. 61)*

Chapter 1

Introduction

Abstract: The implementation of patient-specific computational frameworks into real-life clinical practices may revolutionize the way precision medicine is performed. Improving diagnosis, assisting in surgical procedure planning and contributing to the development and validation of novel medical devices are some examples of how these tools may impact current practices. This thesis aims to explore the numerical techniques that offer the best trade-off between numerical accuracy and reporting time to perform *in silico* analysis of Ascending Thoracic Aortic Aneurysms (ATAAs). In this chapter, the context and motivation of this work are presented, followed by objectives, methodology, relevant publications and thesis outline.

Keywords: Ascending Thoracic Aortic Aneurysm (ATAA), Clinical practices, Computational framework, Patient-specific.

Contents

1.1 Context and motivation

The first records of using techniques and substances to treat illness date back to prehistoric societies. From ancient practices rooted in herbal medicines and spiritual beliefs, to the sophisticated treatments and technologies used in modern practices, medicine has continually advanced. This has contributed to healthier and longer lifespans, eradication of some pathologies and showing an overall remarkable socioeconomic impact. The evolution of medicine has been catalysed by multidisciplinary collaborations with collective knowledge in the fields of, among others, biology, physics, mathematics, informatics, and engineering. The development of vaccines, the discovery of antibiotics, the introduction of minimally invasive surgical procedures or the use of imaging techniques are a few outputs of this kind of collaboration. Ultimately, the progression of medicine is heavily marked by technological evolution, as well as, an increasing understanding of the human body and how we understand and address illness.

Among the registered diseases, cardiovascular diseases are according to World Health Organization (WHO) the leading cause of death worldwide, representing around 32 % of all global deaths in 2019 [2]. Among those, Thoracic Aorta Aneurysm (TAA) have an incidence of at least 6-10 per 100,000 persons per year [3, 4], and around 60 % of those occur in the ascending aorta portion [5, 6], such as Ascending Thoracic Aortic Aneurysms (ATAAs) or sinus of Valsava. According to the American Heart Association (AHA), American College of Cardiology (ACC) and European Society of Cardiology (ESC) guidelines for diagnosis and treatment of TAA, surgical intervention is recommended to patients with a maximum diameter greater than 55 mm [7, 8]. This threshold decreases to 50 mm in patients with Marfan Syndrome or Bicuspid Aortic Valve (BAV) in conjunction with other risk factors such as a growth rate higher than 3 mm/year and family history of aortic dissection or coarction [5, 7]. The clinical management of patients non-elected for a surgical procedure consists of: (i) changes of lifestyle such as moderate exercise and smoking cessation, (ii) reducing the effect of certain risk factors such as hypertension through the administration of antihypertensive drugs and (iii) regular follow-up of the aneurysm growth [9]. The theoretical foundation of the geometrical criterion is Laplace's law which states that the transmural pressure within a tubular structure with constant diameter is directly proportional to the radius and surface pressure, and inversely proportional to the wall thickness of the tubular structure [10]. Also, empirical evidence shows a drastic increase in the risk of acute complications (from 0.6 % to 6.9 %) for aortas with 5 cm and 6 cm diameters [11]. Nonetheless, although still used and efficient, the geometrical criterion is controversial and now extensively recognized as insufficient [12, 13]. Reports show that around 13 % of aortic aneurysms rupture with a maximum diameter less than 5 cm and about 54 % with a diameter over 7 cm do not [14]. There are many possible reasons behind the lack of accuracy of this criterion such as the complex geometry with a variable diameter, the low spatial resolution of the medical imaging exams or the high inter-patient variability [15, 16]. However, the main reason may be attributed the cardiovascular system

has an extremely complex behaviour that is ruled by a strict equilibrium between the hemodynamic, structural and morphological features.

As the complexities of contemporary health challenges continued to be addressed, the need for more robust and efficient diagnosis tools became significant [17–19]. These tools should take into account the complex behaviour of biological systems and the biological variability among individuals. Given this, the concept of creating patient-specific virtual replicas gained relevance. Digital twins assisted by functional imaging, biomechanics, informatics, and clinical and histological data, capable of mimicking the conditions of these systems could revolutionize the way precision medicine is performed [20]. These tools have the potential to improve diagnosis, assist in surgical procedure planning and training, prosthesis design, or even contribute to the development and validation of novel medical devices. Focusing on the issue of the maximum diameter criterion, digital twins could provide additional and otherwise unavailable information such as hemodynamic patterns [21, 22], mechanical response of the vessel wall and estimate the risk of rupture or the growth rate.

One fundamental question dealing with digital twins is how can one accurately simulate the patient-specific conditions of biological systems. Numerical models have been tested and confirmed as a viable solution due to their capability to solve fundamental governing laws of nature. The Finite Element Method (FEM) and Finite Volume Method (FVM) are the most popular numerical approaches for this type of application. However, the introduction of these tools into real-life practices is still limited. One of the main bottlenecks towards the introduction into clinical practices is the extensive reporting time which is a direct consequence of the complexity of the model requiring high computational resources. This topic, in particular applied to the numerical modelling of ATAAs, is the main focus of this thesis where the aim is to identify which numerical approaches yield an optimal trade-off between numerical accuracy and reporting time. Considering this: i) different tissue prestressing methodologies were implemented and analyzed at the level of accuracy and numerical convergence; ii) the results of 2-way Fluid-Structure Interaction (FSI) simulations were compared with the numerical results of more straightforward numerical approaches; and iii) a surrogate modelling framework assisted by clinical and imaging data was developed.

1.2 Objectives and methodology

The research developed in this work aimed to explore one of the main limitations regarding the introduction of computational frameworks into current clinical practices, the extensive reporting time. The main goal is to study the scientific question "What are the numerical approaches that yield an optimal trade-off between numerical accuracy and reporting time?". Also, it is worth mentioning that the work program of this thesis is inscribed in the project PTDC/EMD-EMD/1230/2021 (DOI:10.54499/PTDC/EMD-EMD/1230/2021)

and supported by the PhD grant UI/BD/151212/2021 (DOI:10.54499/UI/BD/151212/2021) which are both funded by the Fundação para a Ciência e Tecnologia (FCT).

1.2.1 Structural objectives

The development of this work imposed a set of scientific challenges. For instance, understanding the theory from engineering, medicine and biology backgrounds, knowledge processing and problem-solving. Additionally, a set of numerical challenges were also faced, such as the post-processing of imaging data, the development of numerical models assisted by patient-specific *in vivo* data, and the coupling of Artificial Intelligence (AI) based techniques with Computational Solid Mechanics (CSM) simulations. Given that, the defined specific structural objectives were:

1. Find what numerical techniques are currently being used to recreate the biomechanics of cardiovascular systems and explore the reasons behind the lack of application into real life clinical practices;

2. Explore different tissue prestressing methodologies and their impact on the numerical results of FSI models;

3. Perform a systematic comparison on the estimated ATAAs biomechanics of a range of numerical models informed by patient-specific data and with varying degree of complexity;

4. Explore the application of AI based tools to perform *in silico* analysis of cardiovascular systems.

To achieve these structural objectives, the following challenges were assumed:

1. Numerically implement the reverse displacement and Prestress Tensor (PT) algorithms;

2. Develop numerical frameworks based on different advanced computational techniques, namely as Reduced Order Model (ROM), Computational Fluid Dynamics (CFD), CSM or FSI, capable of recreating patient-specific ATAAs biomechanics;

3. Develop a Deep Neural Network (DNN)-based surrogate model of ATAA structural mechanics.

1.2.2 Methodology

The starting point was the understanding of all the required theoretical background and a comprehensive systematic review, following the Preferred Reporting Items for Systematic Reviews and Meta-Analyses (PRISMA) methodology, on the literature regarding the numerical modelling of healthy and diseased aortas. Also, a critical discussion of the

results highlighted the lack of accuracy, the extensive reporting time and the lack of validation against large cohorts of patients as the main bottlenecks towards introduction into clinical practices.

The following task consisted of analysing the impact on 2-way FSI simulations of using different tissue prestressing methodologies, namely the Zero Pressure Geometry (ZPG) (reverse displacement algorithm) and the PT algorithms. It was found that the PT contributed to improve numerical convergence. However, also exhibited a stiffer mechanical response of the aortic wall. This issue led to the development of an extension of the PT algorithm, aiming to mitigate. Afterward, the hypothesis that the increased stiffness of ATAAs reduces the relevance of using FSI models was tested. This was done by comparing the results of 2-way FSI simulations with the numerical results of simpler approaches, namely : CFD, ROM and CSM.

Finally, a surrogate modelling framework was developed, coupling CSM and DNN surrogate models, was developed. The use of CSM to estimate the aortic pressure field was a direct conclusion of the previous task since it offered the best numerical efficiency. The surrogate model was developed to recreate the ATAAs wall mechanics and was trained with numerical results of CSM, which also showed good agreement with FSI while requiring less time to compute.

1.2.3 Innovative contributions

The main contributions of this work are a complete review of the numerical methods applied to simulate the biomechanics of arteries, as well as, a critical discussion of the underlying reasons for the lack of application of these solutions in current real-life clinical practices. Furthermore, a database of numerical results, obtained with computational framework based on a coupling of CSM and neural networks, informed by patient-specific clinical and imaging data. Ultimately, this thesis contributed to the expansion of the current knowledge on how to reduce the extensive reporting time of computational frameworks in order to facilitate the introduction into clinical practices.

1.3 Publications in international indexed journals (ISI/Scopus)

In this subsection are listed the scientific outputs published, submitted, or that are currently under preparation for indexed journals and conferences (ISI/Scopus).

1.3.1 Scientific journals

1. **Mourato, A.**, Valente, R., Xavier, J., Brito, M., Avril, S., de Sá, J. C., Tomás, A. C. & Fragata, J. (2022). Computational modelling and simulation of fluid structure interaction in aortic aneurysms: A systematic review and discussion of the clinical potential. Applied Sciences, 12(16), 8049. DOI: 10.3390/app12168049;

2. **Mourato, A.**, Valente, R., Xavier, J., Brito, M., Avril, S., Tomás, A. C., & Fragata, J. (2024). Comparative analysis of Zero Pressure Geometry and prestress methods in cardiovascular Fluid-Structure Interaction. Computer Methods and Programs in Biomedicine, 257, 108475. DOI: 10.1016/j.cmpb.2024.108475;

3. **Mourato, A.**, Valente, R., Xavier, J., Brito, M., Avril, S., Tomás, A. C. & Fragata, J. (2025). Comparison of Numerical Models to Compute Biomechanical Markers in Ascending Thoracic Aortic Aneurysms.;

4. Valente, R., **Mourato, A.**, Brito, M., Xavier, J., Tomás, A. C., & Avril, S. (2022). Fluid–Structure Interaction Modeling of Ascending Thoracic Aortic Aneurysms in SimVascular. Biomechanics, 2(2), 189-204. DOI: 10.3390/biomechanics2020016.

5. Valente, R., **Mourato, A.**, Xavier, J., Sousa, P., Domingues, T., Tavares, P., Avril, S., Tomás, A. C. & Fragata, J. (2024). Experimental Protocols to Test Aortic Soft Tissues: A Systematic Review. Bioengineering, 11(8), 745. DOI: 10.3390/bioengineering11080745

1.3.2 Conference proceedings

1. **Mourato, A.**, Valente, R., Xavier, J., Brito, M., Avril, S., Tomás, A.C., & Fragata, J. (2023). On the Importance of Modelling the Interplay Between the Blood Flow and the Aortic Wall in Ascending Thoracic Aortic Aneurysms. In 10th Congress of the Portuguese Society of Biomechanics (pp. 233-243). Cham: Springer Nature Switzerland. DOI:10.1007/978-3-031-47790-4_22;

2. Valente, R., **Mourato, A.**, Xavier, J., Brito, M., Avril, S., Tomás, A., & Fragata, J. (2023). CFD Model of the Ascending Thoracic Aortic Aneurysms with Patient Wall Deformation. In 10th Congress of the Portuguese Society of Biomechanics (pp. 69-77). Springer, Cham. DOI: 10.1007/978-3-031-47790-4_7;

3. **Mourato, A.**, Valente, R., Brito, M., Xavier, J., Avril, S., Tomás, A., & Fragata, J. (2024). Fluid-Structure Interaction Analysis of Ascending Thoracic Aortic Aneurysms: a Comparison of Prestressing Algorithms. In 9th European Congress on Computational Methods in Applied Sciences and Engineering. CIMNE. DOI: 10.23967/eccomas.2024.264.

1.4 Thesis outline

This thesis is structured in 7 chapters. A summary of the thesis outline and the relation between each chapter is presented in Fig. 1.1. A more detailed description of each chapter is presented below:

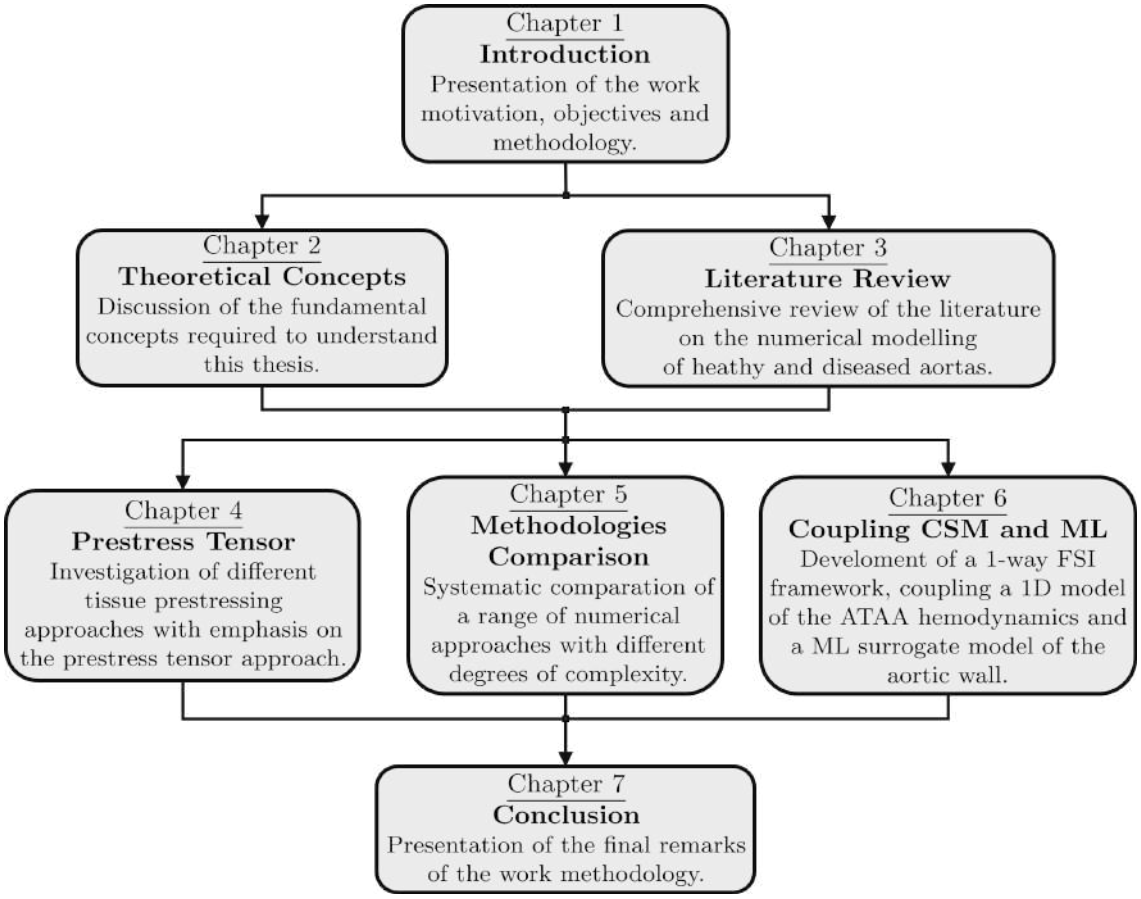

Figure 1.1: Thesis outline and relations between the chapters.

Chapter 2 - Contains a summary of the main fundamental topics required to understand this thesis. It starts with introducing the ascending aorta physiology and follows by exploring hemodynamics and the mechanical response of the aortic wall. To conclude, the natural history, diagnosis and impact on the biomechanics of ATAAs are discussed.

Chapter 3 - Systematic review of the literature using the PRISMA methodology on the numerical modelling of healthy and diseased aortas.

Chapter 4 - Work on the applicability of the PT approach to FSI models. It provides a comparison between the results of the ZPG and the PT methodologies in the context of FSI simulations of ATAAs. Also, suggests an extension of the PT methodology.

Chapter 5 - Comprehensive comparison between 2-way FSI simulations and the numerical results of more straightforward approaches, namely: CFD, ROM and CSM.

Chapter 6 - Details the development and training of a DNN surrogate model of ATAA structural mechanics. Data from CSM simulations was used to construct the training dataset.

Chapter 7 - Provides an overview of the methodology employed in this thesis and presents the main remarks and findings. Also, explores the limitations of this work and future applications.

Chapter 2

Aorta: Anatomy, Physiology, Biomechanics and Aneurysms

Besides complementary studies also cited throughout this chapter, the following bibliography was the fundamental basis:

1. Gasser, T. C. (2021). Vascular Biomechanics: Concepts, Models, and Applications. Springer International Publishing. DOI: 10.1007/978-3-030-70966-2 [23];

2. Hall, J. E., & Hall, M. E. (2020). Guyton and Hall Textbook of Medical Physiology (14). Elsevier Health Sciences. ISBN: 978-0-323-59712-8 [24];

3. Baskurt, O. K., Hardeman, M. R., & Rampling, M. W. (Eds.). (2007). Handbook of hemorheology and hemodynamics (Vol. 69). IOS press. ISBN: 978-1-58603-771-0 [25];

4. Thiriet, M. (2007). Biology and mechanics of blood flow: Part II: Mechanics and medical aspects. Springer Science & Business Media. DOI: 10.1007/978-0-387-74847-4 [26].

Abstract: At first glance, the domains of medicine and mechanical engineering may appear to have no intersection. Beyond this apparent dichotomy lies a symbiotic relationship which is essential for unravelling the complexities of biological systems. For instance, a strong background in continuum mechanics is crucial for developing a greater understanding of the underlying mechanism leading to aneurysms. The multidisciplinary nature of

this subject also requires essential contributions from biology, mathematics, and several other scientific fields. The objective of this chapter is to address the main fundamental concepts across the necessary fields. In particular, the aortic anatomy and physiology, constitution and mathematical modelling of blood and aortic wall, aortic hemodynamics, the mechanical response of the aortic wall, and the pathophysiology of aortic aneurysms are addressed.

Keywords: Aneurysms, Aortic hemodynamics, Aortic wall mechanics, Fundamental concepts.

Contents

2.1 Anatomy and physiology of the aorta

The cardiovascular system is responsible for maintaining a continuous supply of oxygen and nutrients to the necessary regions of the body. Also, it is responsible for removing the residues of metabolic processes and promoting the immune response by delivering leucocytes to regions where pathogenesis is occurring [27]. These substances are transported by the blood, flowing in a network of vessels composed of two main circuits, namely the pulmonary and systemic circulations [28]. In the first, the blood flows from the right ventricle, through the pulmonary artery and is delivered to the lungs, where the carbon dioxide is released, and the oxygen absorbed, returning afterward to the left atrium via the pulmonary veins [29]. In the latter, the blood is ejected from the left ventricle, which acts as a biological volumetric pump, into the main artery of the cardiovascular system, the aorta and is distributed to the entire body, returning to the right atrium through the superior and inferior vena cava (Fig. 2.1-a).

Originating on the aortic root and extending to the abdomen (Fig. 2.1-b), where it splits into two lower calibre arteries (left and right common iliac), the aorta is composed of several segments, namely, the ascending aorta, aortic arch, descending aorta, and the abdominal aorta [30]. Geometrically, it resembles a walking stick and has a variable diameter along its centreline that ranges in healthy subjects from around 3 cm in the ascending portion to about 1.8 cm at the descending aorta. From a mechanical standpoint, is a complex, dynamic and tightly regulated tubular structure [31] with fascinating physiology and properties. It possesses three distinct layers, each with unique constitutions and consequently unique functions [14, 32]. The constitution, alongside the microstructure, dictates the macroscopic mechanical properties [33, 34] of the aortic wall. These, as well as, the thickness are not uniform along the aorta, being the abdominal aorta generally stiffer than the ascending aorta [31], for instance.

Nonlinear elasticity and structural integrity are arguably the most relevant characteristics of the aortic wall which allows the vessel to sustain significant deformation during the cardiac cycle [35]. This deformation momentarily accommodates a certain volume of

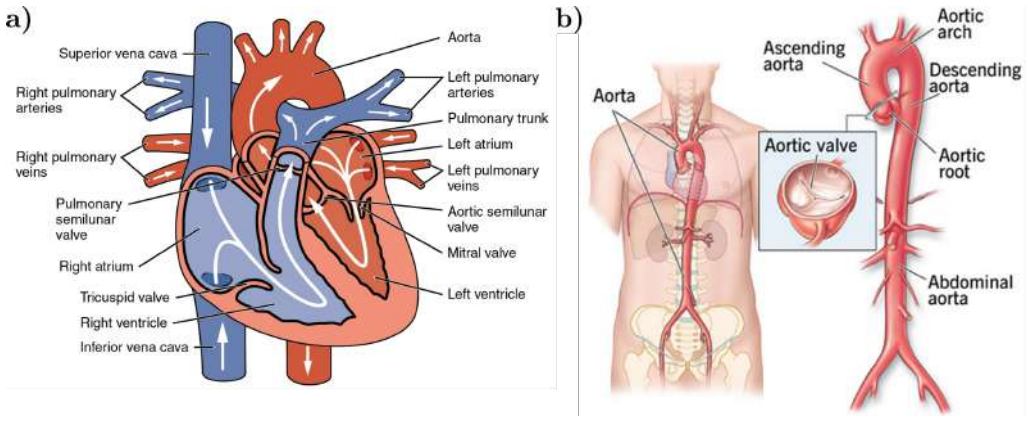

Figure 2.1: a) Heart, major vessels and b) aortic segments.

blood, which is redirected as the aorta returns to its original shape. This phenomenon resembles the effect of a buffering chamber, or a "hemopneumatic" reservoir, and is known as the Windkessel effect contributing to reducing the systolic-diastolic pressure differential and maintaining organ perfusion during diastole [36]. The ascending portion of the aorta, the main focus of this thesis, is where the Windkessel effect is more evident. This region accommodates about 50 % of the total ejected blood during systole [37], and can be better compared to the effect of a second volumetric pump assembled in series with the heart. Additionally, this region is also responsible for converting the heart's pulsatile flow into a continuous flow downstream of the aortic arch [38] and is subjected to axial displacement and torsion imposed by the heart's motion [39, 40].

2.2 Blood, a suspension, a non-Newtonian fluid or neither?

The relation between the constitution, mechanical properties and functions of blood is the starting point in understanding the intricate dynamics within the cardiovascular system. From the macrocirculation to the microcirculation, this one fluid exhibits remarkable adaptability to a wide range of mechanical stimuli, geometrical scales (e.g. 3 cm in the aorta to 5 µm in the capillary) and overall biomechanical conditions to meet the requirements of each circulation.

Blood when analysed from a biological point of view can be interpreted as a tissue constituted by various cells and intercellular fluid [41]. From a rheological standpoint, it can be interpreted as a concentrated solid-fluid suspension of formed elements and plasma [42]. Plasma is a Newtonian fluid as it is an aqueous solution of mostly water (91-92 %) and proteins (8-9 %). Is responsible for controlling osmotic pressure and blood clotting, regulating the fluid content of cells, and enabling immunological response. The formed elements are:

Erythrocytes - or red blood cells, possess a biconcave shape and are fundamentally hemoglobin involved in a thin flexible membrane. The hemoglobin is the carrier of oxygen due to its ability to reversibly bind to this element. The deformability allows the erythrocytes to adopt a bullet-like shape to pass through microvessels [43].

Leukocytes - also known as white blood cells, are eukaryote cells produced by the bone marrow [41]. Leukocytes have distinct phenotypes each with unique functions. They play a crucial role in activation, immune suppression, and modulation of immune surveillance against pathogens and foreign invaders [41, 44].

Thrombocytes - or platelets, are cell fragments involved in blood clotting. They have an average lifetime of 10 days and their activation is highly dependent on the hemodynamic forces.

The formed elements generally occupy 40-50 % of the volume of blood. Leukocytes and thrombocytes occupy together only around 1 % of the volume of blood, which makes

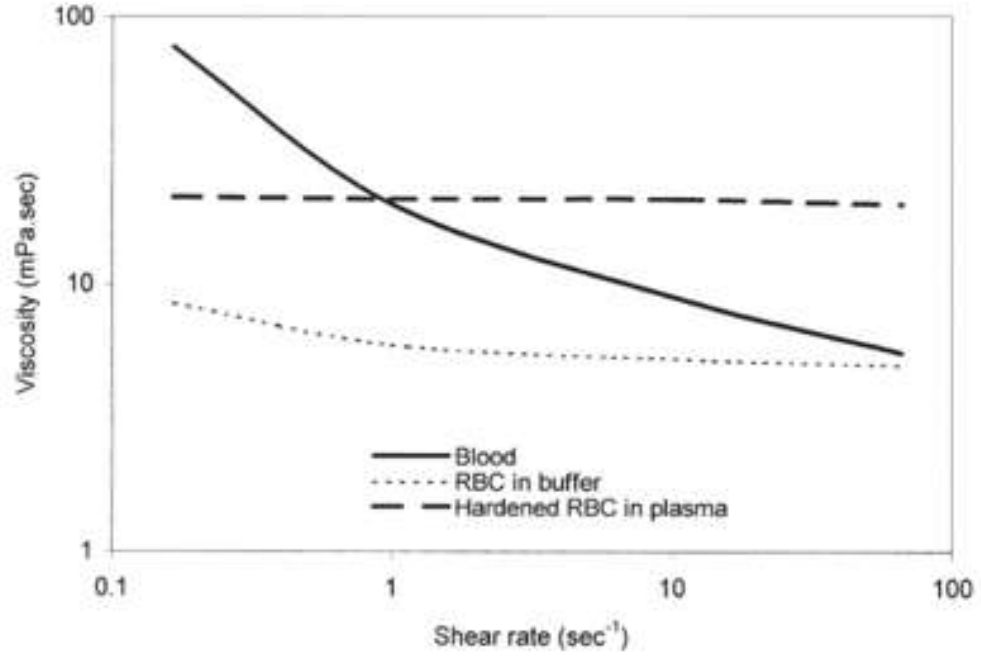

Figure 2.2: Relation between viscosity and shear rate for: regular blood (full line), blood sample where red blood cells aggregation is prevented (dashed lined), and blood sample with rigid red blood cells (pointed line). Adapted from [25].

them insignificant to the hemorheology in the macrocirculation [45]. These become relevant when the size of the vessel is reduced, particularly when the vessel diameter is smaller than the size of the formed elements [42, 46]. The main focus of this section is the hemorheology in the arterial macrocirculation, please consult [43, 47, 48] to further explore the particularities of microcirculation.

Erythrocytes represent at least 98 % of the volume occupied by formed elements. Due to the elevated concentration of these elements, their mechanics on the microscopic level are impactful on the macroscopic mechanical response of the blood [41]. Healthy erythrocytes are flexible and tendentially align with flow streamlines especially when deformed by the action of the shear forces. These two phenomena coupled with the ability to aggregate in stacks (rouleaux) are the main contributors to the shear thinning viscosity (Fig. 2.2), defined as a negative correlation between the shear rate and the viscosity [49]. As the shear rate increases, the red blood cells deform and align with the flow resulting in a reduced apparent viscosity. From a mechanical point of view, this seems to be relevant in high-velocity regions as it reduces the viscous loads, contributing to the energy conservation of the fluid. On the opposite end of the spectrum, the venous blood flow, characterised by low shear rates [50, 51], seems to benefit from higher viscosities as it assists in preventing retrograde flow. Besides the evident shear-thinning behaviour, viscoelasticity, non-zero yield stress and thixotropy are also relevant characteristics of the hemorheology [42]. Several other factors such as temperature, plasma protein concentration, temperature and drugs may influence the mechanical properties of blood [41].

2.2.1 Numerical modelling of blood rheology

On the topic of numerical modelling Ascending Thoracic Aortic Aneurysms (ATAAs) hemodynamics also becomes relevant to understand what mathematical solutions are available to capture the mechanical behaviour of blood. A summary of the most commonly used blood constitutive models to recreate the hemodynamics of large calibre arteries is presented in Table 2.1.

Table 2.1: Common rheological models applied to *in silico* analysis of large calibre arteries hemodynamics.

Model	Viscosity Equation [μ]	Description	References
Newtonian	μ_∞	The most straightforward approach towards modelling the rheology of blood. Defines viscosity as constant and is the most common assumption for aortic hemodynamics.	[39] [52] [53] [54] [55] [56] [57] [58]
Carreau-Yasuda	$\mu_\infty + \frac{\mu_0 - \mu_\infty}{\left(1+\Gamma'\dot{\gamma}^\alpha\right)^{\frac{1-n}{\alpha}}}$	In this approach Γ', μ_0, μ_∞, and n are, respectively, the time constant, viscosity for low and high shear rates, and the power law constant. It is an extension of the Carreau model which considered $\alpha = 2$, being α the coefficient defining the transition between low and high shear rate.	[59] [60] [61] [62] [63] [64]
Casson	$\mu_\infty\left[1 + \sqrt{\frac{\tau_0\rho_f}{\mu_\infty\dot{\gamma}}}\right]^2$	The constitutive parameters of the Casson model are the viscosity at high shear rates, μ_∞, and a phenomenological parameter, τ_0, that denotes the stress above which rouleaux formation is ceased.	[65] [66] [19] [18] [67]

Power-Law	$\mu_0\left(\Gamma'\dot{\gamma}\right)^{n-1}$	This relation is expressed in terms of the viscosity, μ_0, at the shear rate equal to the inverse of the time constant, Γ'. The parameter n defines the type of fluid. For $n = 1$ the behaviour of the fluid is the one of a Newtonian fluid, whilst if $n < 1$ the fluid presents a shear-thinning response.	[65] [68] [69] [70] [71]
Walburn-Schneck	$C_1 e^{C_2 H}\left(\Gamma'\dot{\gamma}\right)^{-C_3 H}$	In this generalization of the Power-Law model, $\mu_0 = C_1 e^{C_2 H}$ and $n = 1 - C_3 H$ are defined trough empirical relations dependent on the hematocrit, $H\ \epsilon\ ]0, 1[$.	[72] [73] [74] [75]
Quemada	$\mu_p\left[1 - \frac{C_1 + C_2\sqrt{\dot{\gamma}/C_3}}{2(1+\sqrt{\dot{\gamma}/C_3})} H\right]^{-2}$	The Quemada model is a semi-phenomenological approach, that defines blood as a suspension of erythrocytes in plasma. The model parameters are the plasma viscosity, μ_p, and the hematocrit. Also, C_1 , C_2 and C_3 are determined through empirical relations.	[27] [76] [77] [78]

The use of each model is dependent on the specific application and methodology. Regarding the numerical simulation of aortic hemodynamics, and in particular for ascending aorta hemodynamics, the common assumption is that in large calibre arteries the shear rate, induced by the high velocities, is above the 100 Hz threshold. Thus, the blood acts mostly as a Newtonian fluid [60, 65, 71, 79]. The use of more complex rheological models becomes relevant for regions with low shear rates [59], which can occur in the aorta in the presence of saccular aneurysms [80] or aortic dissections [81], for instance. Beris et al. [42] provided a complete overview of blood constitutive modelling, including thixotropic, viscoelastic, microscopic, mesoscopic and multiscale models.

2.3 Aortic hemodynamics

Homeostasis is defined as the tendency of living organisms to maintain an internal state of equilibrium through constant regulation and adaptation [82]. Disturbances in this delicate balance are believed to be possible triggers for developing cardiovascular

diseases [18, 83]. Hemodynamics constitute a pivotal aspect contributing to homeostasis and is intricately connected to the local anatomy, vessel wall properties, and blood rheology. Regional variations in these features also promote variations in the local hemodynamics of the cardiovascular system.

Analogous to the mitochondria, the heart serves as the powerhouse of the cardiovascular system. It is a double volumetric biological pump build-up of three layers: i) epicardium, the outermost layer responsible for protection; ii) myocardium, the muscular layer containing cardiomyocytes; and iii) endocardium, the innermost layer of endothelial cells [84]. During a cardiac cycle, the heart receives blood from the venous system in the two upper chambers, the atria, and ejects it into the arterial system through the two lower chambers, the ventricles. Specifically, one may say the cardiac cycle initiates with an isovolumetric relaxation of the ventricles and simultaneous atrial filling. Upon atrial pressure surpassing ventricular pressure, the atrioventricular valves open, permitting blood flow into the ventricles, aided by atrial contraction. The cessation of atrial systole triggers ventricular systole. This phase starts with an isovolumetric contraction, followed by ventricular contraction. The pressure increase eventually causes the opening of the pulmonary and aortic valves and consequent blood ejection into the pulmonary trunk and aorta [84].

The opening of the aortic valve marks the initiation of blood ejection into the ascending aorta. Due to the anatomy of the valve and high blood pressure, a jet flow is formed, propagating towards the outer curvature of the ascending aorta [24, 84]. This flow possesses high momentum which enables it to travel long distances without major energy dissipation. Upon impacting the outer curvature of the aortic wall, the blood is redirected towards the aortic arch, from where it is distributed to the supra-aortic branches (brachiocephalic trunk, left common carotid artery, and left subclavian artery) and descending aorta [52, 60]. In the descending aorta, the blood gradually acquires a parabolic velocity profile, indicative of a developed flow [85]. Nonetheless, it is pertinent to note that the presence of a singular, standardized flow pattern in healthy subjects is not definitive; rather, it is more plausible to consider a spectrum of flow patterns [86].

The analysis of Magnetic Resonance Imaging (MRI) data is crucial to further explore the intricacies of aortic hemodynamics. Studies in this realm have revealed that nearly 80 % of healthy patients exhibit, in addition to the aforementioned characteristics, a right-handed helical flow [85, 86]. Such a phenomenon is common across various regions of the cardiovascular system and plays a significant role in protecting arteries against pathologies, such as atherosclerosis, thrombosis, and intimal hyperplasia [87, 88]. Moreover, the presence of two counter-rotating helices within the ascending aorta is commonly observed which is believed to stem from blood impingement on the aortic wall [60, 89]. Another noteworthy attribute of aortic flow is its predominantly laminar nature [90]. Analysis of the Reynolds number along the aorta corroborates this hypothesis, presenting in the worst-case scenario flow in a transitional regime [90]. However, there is still some discussion regarding the presence and impact of turbulent flow near the aortic root [91, 92].

Pressure field and Wall Shear Stress (WSS) represent two other critical hemodynamic parameters. The pressure field governs vessel wall deformation, with its analysis being integral to understanding acute events such as aortic rupture and dissection [93, 94]. Conditions like hypertension can pose significant risks, particularly as vessel walls stiffen over time [95]. WSS, on the other hand, influences endothelial function, arterial remodelling, atherosclerosis, and aneurysm development [15, 19, 96].

2.4 Aortic wall mechanics

The aortic wall is a complex, tightly regulated and dynamic structure. It is specialized to sustain large deformations under pulsatile flow, store elastic energy, and withstand long-term mechanical fatigue over billions of cycles. These characteristics are a result of the aortic wall composition and microstructure. The understanding of these aspects is essential for accurate modelling of ATAAs biomechanics.

The aortic wall is composed of three distinct layers (Fig. 2.3-a), each with unique constitutions and functions [14]. The innermost layer, tunica intima, accounts up to 5 % of the wall thickness and consists of a single layer of endothelial cells (endothelium) supported by a thin basal membrane. The primary role of the endothelium is regulatory rather than structural. As it deforms due to the effect of WSS, it triggers signalling cascades that mediate metabolic processes. Furthermore, this layer also plays crucial roles in preventing thrombosis and acting as a low-friction barrier between the blood and the vessel wall [32]. The tunica media forms the bulk of the aortic wall thickness (Fig. 2.3-b) and is the principal load-bearing layer. It consists of a 3D network of Media Lamellar Units (MLU), each comprising two elastic lamellae, one Vascular Smooth Muscle Cell (VSMC), and ExtraCellular Matrix (ECM). These components are preferentially aligned in the circumferential direction and one MLU is around 14 μm thick. It is estimated that the ascending aorta has around 60 lamellar units while the abdominal aorta presents about 30 units [97]. From a physiological standpoint, the media is responsible for most of the elasticity of the aortic wall and the main contributor to the Windkessel effect. The tunica adventia is the outermost layer of the aortic wall, composed primarily of collagen, fibrolasts, proteoglycans and connective tissue. Its main functions are to anchor the aorta to the surrounding vasculatures and prevent the other layers from overstretching. Also, in the adventia is possible to find the *vasa vasorum*, a network of small blood vessels that perfuse also to the outer region of the media.

2.4.1 Wall composition and microstructure

The aortic wall can be described as a combination of two main components: the ECM and vascular cells. The ECM provides the structural integrity of the vessel, mediating most of its passive mechanical properties and ensuring overall integrity. The vascular cells are responsible for sensing the mechanical loads and changing the wall accordingly.

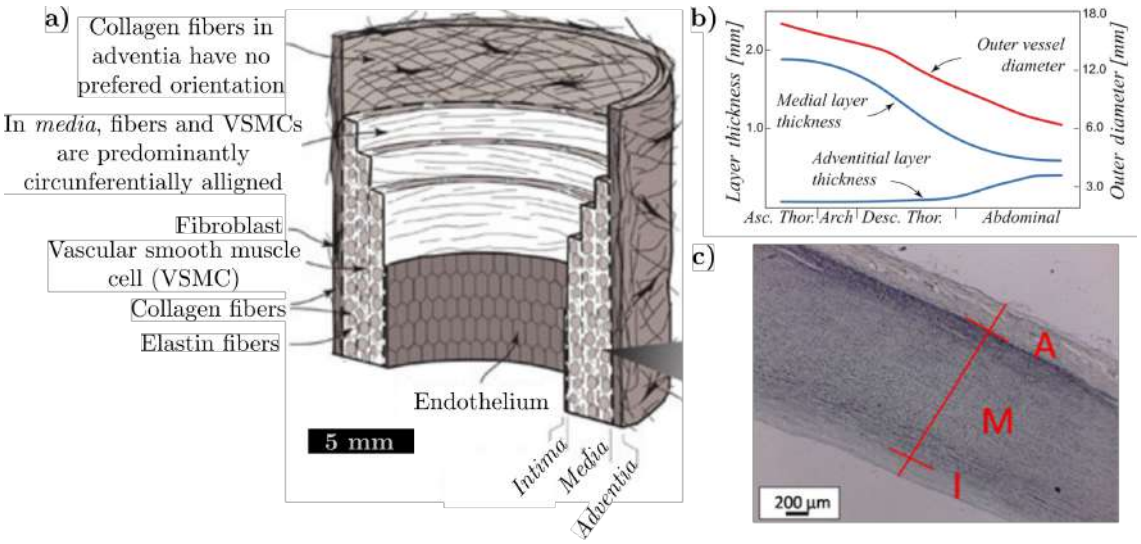

Figure 2.3: The aortic wall: a) layers and histological characterization; b) layer thickness and outer diameter across the aorta; and c) cross-section from human aorta. Adapted from [23, 98].

Additionally, the vascular cells also play a crucial role in stimulating the migration of immune and inflammatory cells to the aortic wall.

The ECM is an organized network of proteins vital to the normal physiology of the aorta. On one hand, acts as scaffold of the surrounding cells. On the other hand, is a structure that mediates the micro and macro mechanical response of the aortic wall. The main components of the ECM are elastin, collagen, proteoglycans, glycosaminoglycans, fribonectin and fibrillin.

Elastin and collagen work in partnership as the two main load-bearing components of the ECM. Elastin is the main structural component of the tunica media layer. Nonetheless, its influence is almost negligible in the adventia. It dictates the mechanical properties at low-strain and is crucial for the elastic recoil (Windkessel effect) during the diastole. Most commonly is found in the aortic wall under the form of sheets that encapsulate MLU. Furthermore, it can also be found in interlamellar fibres and radial struts [99]. Collagen provides stiffness and strength, limiting excessive dilation during the cardiac cycle. At mean arterial pressure only around 6% of the collagen is recruited, being its influence more prominent for higher loads. This occurs due to the collagen being in a wavy state that needs to be fully stretched before bearing the load. The concentration and spatial orientation of collagen fibrils highly impact the mechanical properties of the aorta. In Fig. 2.4 the stress-stretch curves of elastin-rich and collagen-rich samples from human aortic media tissue are presented.

Three main cell types are found in the aortic wall:

Endothelial cells - form an anti-thrombotic and low-resistance surface between the blood flow and the aortic wall. They are mechano-sensitive to WSS and segregate vasoactive agents in response to the mechanical loading [101].

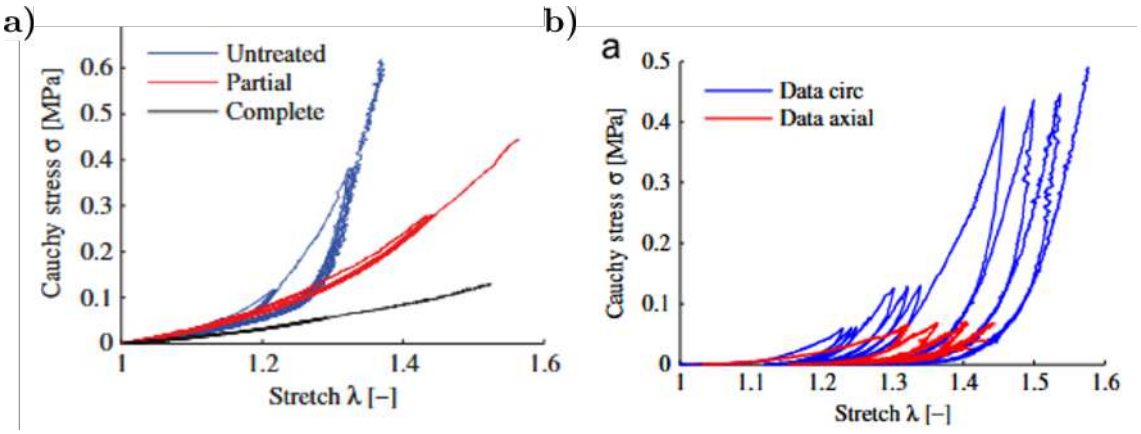

Figure 2.4: Stress-strain results of uniaxial tensile tests on human thoracic aortic samples treated with : a) collagenase; and b) elastase. Adapted from [100].

VSMC - depending on the phenotype these cells may contract in response to stimulli, regulating the vessel diameter and, therefore, impacting flow resistance [102]. Also, if at the synthetic phenotype is able to produce molecules in response to injuries and disease [103]. Abnormal functioning of VSMC contributes the development of vascular diseases.

Fibroblasts - mainly present in the adventia. It is responsible for synthesize ECM constituents, as well as, Matrix MetalloProteinase (MMP) which degrade the ECM.

2.4.2 Mechanical properties of the aortic wall

Arteries are dynamic biological systems that respond to mechanical loading in both passive and active ways. The passive response is directly mediated by the composition and microstructure of the ECM, while the active response is governed by cellular processes such as VSMCs contraction. In this subsection, the focus will be on the passive mechanical properties of the aortic wall.

One crucial property of the aortic wall is the nonlinear stress-strain response. At low strain-rates, predominantly the elastin fibres are being engaged [100, 104]. This provides high compliance, allowing the aorta to expand easily during systole. As the mechanical load increases, collagen fibres (previously is a wavy state) progressively straighten and engage, resulting in a drastic increase in stiffness [100, 105]. This sequential recruitment of ECM components results in the characteristic J-shaped stress-strain curve of vascular tissues (Fig. 2.5-a).

The aortic wall also displays anisotropic and viscoelastic behaviours [105, 107]. Collagen fibres are preferentially oriented in the circumferential direction. Thus, the aorta is often stiffer along the circumferential direction (Fig. 2.5-b). Additionally, the aortic wall also exhibits properties such as creep, relaxation and dissipation of energy during cyclic loading as shown in Fig. 2.5-c.

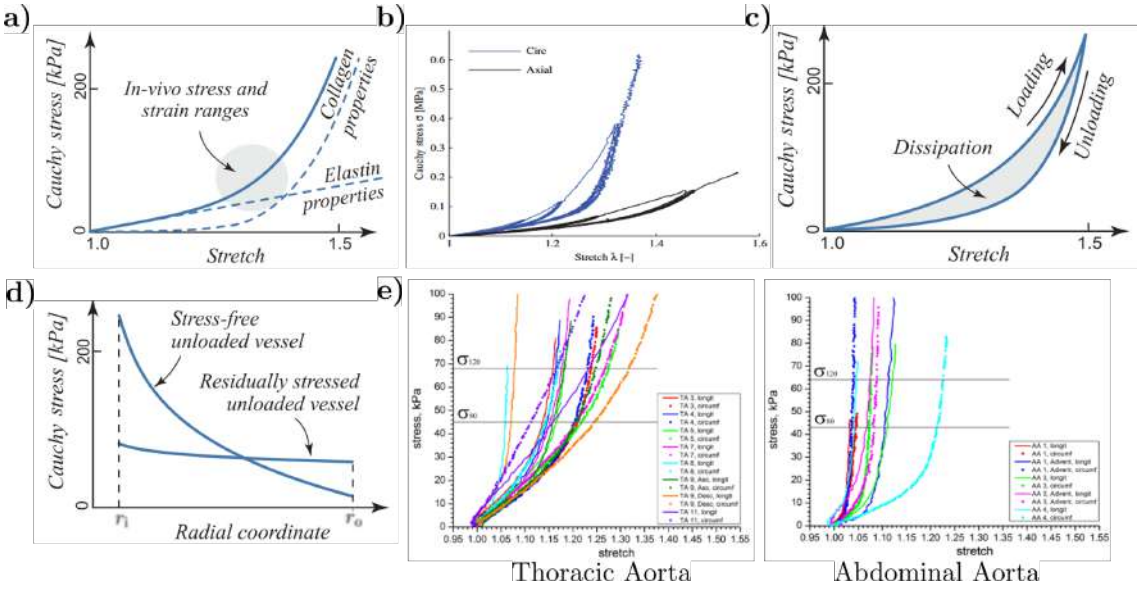

Figure 2.5: Passive mechanical properties of the aortic wall: a) nonlinear stress-strain response; b) anisotropy; c) viscoelasticity; d) presence of residual-stresses; and e) heterogeneity. Adapted from [23, 100, 106].

Another important feature is the presence of residual stresses (Fig. 2.5-d). This occurs due to the turnover of constituents which tends to homogenise the stress within the aortic wall. Opening angle tests may be used to characterise these stresses [108]. Finally, the aortic wall is mechanically heterogeneous (Fig. 2.5-e). Differences exist not only between the intima, media, and adventitia, but also along the length. For instance, the ascending aorta is typically more compliant than distal segments [106], reflecting the specific physiology of this region.

2.4.3 Constitutive models

Constitutive models suggest a strain energy density function, $\boldsymbol{W}$, that recreates the vessel mechanical response. A wide range of constitutive models have been applied to describe the structural mechanics of the aortic wall. These models can be broadly classified into two categories: a) purely phenomenological, and b) histo-mechanical. Purely phenomenological approaches provide a mathematical description that can be tuned to fit experimental data in a straightforward manner. However, they often show limited robustness when used to predict behaviour outside the range of calibration. In contrast, histo-mechanical models explicitly account for the contributions of distinct ECM components, such as elastin and collagen, which are represented by separate terms in the strain energy function. A summary of commonly used constitutive models for simulating aortic structural mechanics is presented in Table 2.2.

Table 2.2: Common phenomenological descriptions of the aortic wall.

Model	Strain energy density function [W]	Description	References
Neo-Hookean	$\frac{\mu^s}{2}(I_1 - 3)$	Specific application of the Yeoh model, considering only one material property. μ^s is the second Lamé parameter and I_1 is the first invariant of the right Cauchy-Green deformation tensor,$\boldsymbol{C}$.	[52] [109] [110] [111] [112] [113] [114]
Demiray	$c_1\left(e^{\,c_1(I_1-3)} - 1\right)$	Isotropic exponential model. Includes an exponential term to model the progressive stiffening. c_1 and c_2 are the material parameters	[115] [116] [117]
Fung	$\frac{c}{2}\left[e^Q - 1\right], \quad Q = a_{ij}E_iE_j$	Phenomenological exponential model with quadratic strain term. Parameters lack direct histological meaning. c and a_{ij} are the model parameters and E_{ij} is the components of the Green-Lagrange strain tensor.	[118] [119] [120] [121]
HGO	$\frac{\mu^s}{2}(I_1 - 3) + \sum_i^N c_{1i}\left[e^{c_{2i}\left(I_{4i}-1\right)^2} - 1\right]$	Fibre-reinforced anisotropic model. Separates elastin and collagen contributions. Widely adopted for arterial wall mechanics. The first term is referent to the elastin (similar to the Neo-Hookean). c_{1i} and c_{2i} are material parameter related to the i-th family of fibres (usually $N = 2$). I_{4i} is the fourth invariant, $I_{4i} = C : A_i$, with A_i representing the spatial organization of the family of fibres.	[122] [123] [14] [124] [125] [126] [127] [128]

In addition to these formulations, the literature also describes constitutive models that extend beyond hyperelasticity. Examples include models that incorporate viscoelastic

effects to capture time-dependent deformation, as well as, growth and remodelling frameworks that describe long-term adaptations of the aortic wall under altered hemodynamic conditions. More recently, approaches capable of accounting for damage and failure have been proposed, aiming to provide a more comprehensive description of the progression toward aortic dissection or rupture.

2.4.4 Aortic reference configuration

To accurately perform structural analyses of the aortic wall, knowledge of the stress-free configuration is required. This poses a challenge in cardiovascular biomechanics because the aorta is always mechanically loaded, by remaining pressurized and axially stretched throughout the entire cardiac cycle. Consequently, geometries obtained from medical imaging correspond not to a stress-free state, but to a pre-deformed configuration. This distinction is particularly important for materials with nonlinear stress-strain behaviour, such as the aortic wall. Different approaches to overcome this issue have been proposed in the literature [129–131] which are discussed in greater detail in Chapter 4.

2.5 Aortic aneurysms

An aortic aneurysm is defined as a permanent, localized dilation of the aorta, typically defined by a growth in diameter greater than 50% in relation to the normal diameter. Factors such as age, smoking, gender and family promote the development of aneurysms. Genetic diseases such as Marfan Syndrome and Loeys-Dietz syndrome are also risk-factors for aneurysm growth. Aortic aneurysms are typically asymptomatic and when left untreated may lead to catastrophic events such as aortic dissection or rupture [132, 133]. Currently, risk stratification of acute complications is performed using the maximum diameter criterion [7, 8], which is based in Laplace's Law and empirical data [133, 134]. However, it is now recognized that this criterion tends to overestimate the risk for larger aneurysms and underestimate it for smaller ones. Furthermore, evidence in the literature suggests that acute complications have occurred in patients with maximum diameters previously considered safe [135, 136]. Hence, although this criterion remains the clinical guideline, it is clearly insufficient for predicting the actual risk of acute events in every patient, as it fails to capture the complexity of the cardiovascular system and inter-patient variability.

At the microstructural level, aneurysm formation is primarily associated with alterations in the ECM and the behaviour of vascular cells. Elastin fragmentation and degradation reduce the vessel's capacity to store elastic energy and is the initial trigger for aortic dilation. The increase in collagen content and collagen synthesis are main contributors to local weakening of the aneurysm wall. Furthermore, the apoptosis of VSMC, excessive inflammatory response and increased oxidative stress are also common pathological features in aneurysms. These changes in the microstructure result in an overall

weakening of the vessel's wall.

The changes in the vessel wall also impacts the hemodynamics. Similarly to healthy patients, it's not evident the existence of one typical flow pattern in ATAAs patients. Nevertheless, is also true that ATAAs patients present a higher variability in flow patterns. Hope et al. [86] analysed the flow in 19 healthy subjects and 13 ATAAs patients. The results suggested a total of five different flow patterns in the patients. On the reverse direction, disturbed hemodynamics may also be the trigger to rearranges in the aortic wall microstructure.

Chapter 3

State of the Art

The work presented in this chapter was published in 2022 by MDPI: **Mourato, A.**, Valente, R., Xavier, J., Brito, M., Avril, S., de Sá, J. C., Tomás, A. C. & Fragata, J. (2022). Computational modelling and simulation of fluid structure interaction in aortic aneurysms: A systematic review and discussion of the clinical potential. *Applied Sciences*, *12*(16), 8049. DOI: 10.3390/app12168049.

Abstract: The diagnosis and treatment of aortic aneurysms is performed according to guidelines which suggest surgical procedure for aneurysms with a maximum diameter above a critical threshold. It is an important cause of death in developed countries, especially for older patients. Despite conservative, this clinical approach is also not able to predict the risk of acute complications for every patient. In the last decade, there has been a growing interest towards the development of advanced in *in silico* aortic models which may assist on clinical diagnosis, on surgical procedure planning or on designing and validation of medical devices. This paper details a comprehensive review on computational modelling and simulation of blood vessel interaction in aortic aneurysms and dissection, following the Preferred Reporting Items for Systematic Reviews and Meta-Analyses (PRISMA). In particular the following questions are addressed: "What mathematical models were applied to simulate the biomechanical behaviour of healthy and diseased aortas?" and "Why are these models not clinically implemented?". Contemporary evidence proves that computational models are able to provide clinicians with additional otherwise unavailable *in vivo* data and potentially identify patients who may benefit from earlier treatment. Notwithstanding, these tools are still not widely implemented primarily due to low accuracy, extensive reporting time and lack of numerical validation.

Keywords: Aortic aneurysms, Advanced *in silico* models, Blood vessel interaction, Fluid-Structure Interaction (FSI).

Contents

3.1 Research contextualization and objectives

The development of patient-specific computational models that could mimic the biomechanical behaviour of CardioVascular Disease (CVD) have been presented as an adding value clinical exam [20, 137]. These models are able to provide clinicians with insightful *in vivo* patient-specific data such as Wall Shear Stress (WSS), pressure distributions, displacement fields, intramural stress state or flow patterns which are otherwise unavailable. Over the last few decades, these advanced computational models and simulation tools have also enabled a better understanding of the underlying mechanisms of a variety of CVD. Several computational techniques, such as the Finite Element Method (FEM), Machine Learning (ML) and Smoothed Particle Hydrodynamics (SPH) have been applied. These techniques spanning the entire range of numerical approaches which encompass Computational Solid Mechanics (CSM), Computational Fluid Dynamics (CFD) to Fluid-Structure Interaction (FSI). CSM is useful to study the Wall Stress (WS) distributions and deformations [32, 138]. CFD solves the governing equations of fluid mechanics and studies hemodynamics patterns and metrics [80, 139]. FSI combines the above-mentioned approaches and simultaneously evaluates hemodynamics and wall motion [113, 123]. Exploring the limitations of current numerical models which are constraining the introduction into clinical practices and provide an extensive overview of the utilized numerical techniques to reproduce aortic biomechanics are the main rationales of this review.

In this chapter, a systematic review following the Preferred Reporting Items for Systematic Reviews and Meta-Analyses (PRISMA) [140] methodology is presented, concerning the computational modelling and simulation of the biomechanical behaviour of healthy and diseased aortas and explore their methodologies, hypothesis, and risk evaluation metrics in view of their usage into clinical practices in order to answer the following scientific questions: "Which numerical models have been applied to simulate the biomechanical behaviour of healthy and diseased aortas?" and "Why are these models not clinically implemented?.

This chapter is organised as follows: Section 3.2 explains how the search, selection and screening processes were performed; In Section 3.3, a summary of the selected articles is presented and in Section 3.4 the raised questions are discussed; and, in Section 3.5 a summary of the systematic review is given.

3.2 Research methodology

3.2.1 Search strategy

This review was guided in accordance to the PRISMA methodology [140]. A comprehensive electronic research was performed in the Scopus electronic database until 23th of February 2022, with no restrictions regarding date of publication and language. This search was performed by combining the search terms: "numerical model" and "aorta".

3.2.2 Inclusion and exclusion selection criteria

In this search, only studies on human healthy and diseased aortas were accepted. Moreover, studies that reported the use of any numerical method to evaluate biomechanical parameters that are not directly accessible through medical imaging exams, such as velocity and displacement fields, WSS and WS distributions or even wall material properties on healthy and diseased aortas were included. Reports of the applicability or development of novel risk indexes were also elected. Lastly, studies that assessed the effect of hemodynamic or mechanical stresses on wall microstructure or used idealized geometries were also included.

The studies that were not included analyzed specific populational groups (*e.g.* pregnant women or newborns); studied the biomechanical behaviour of post-surgery aortas; assessed the efficiency of certain treatment methodologies or focused on undesirable anatomic regions (*e.g.* heart, brain, iliac arteries or bones). Lastly, reviews, comments and conference proceedings were also excluded.

3.2.3 Quality assessment

All gathered results were classified based on the selected method to perform numerical validation following the recommendations of the GRADE handbook [141, 142]. The attributed grades were "high", "moderate" or "low" to works that compared the numerical results with *in vivo* patient-specific data, *in vitro* measurements and other *in silico* results or did not perform any sort of validation, respectively.

3.2.4 Study selection

The screening process of the elected results was performed in two different stages. In the first stage, both title and abstract of all researched works were analyzed and only the ones meeting the selection criteria were elected for the full-text revision. In the second stage, during full-text analysis, the work's compatibility with the inclusion and exclusion criteria is again checked. Also, prior to reading analysis spreadsheets were developed in order to standardize and synthesize the data extraction process.

3.3 Selected articles analysis

3.3.1 Results overview

The complete database contained a total of 214 articles. After the first screening process 63 were excluded. From the remaining 151 articles, 7 were not available to full-text analysis and 29 were excluded during the second screening phase. In the end, the database of articles comprised a total of 115 articles. In Fig. 3.1 the PRISMA flowchart for systematic reviews is presented. This also describes the evolution of accepted articles throughout the several screening stages, where n is the number of available articles.

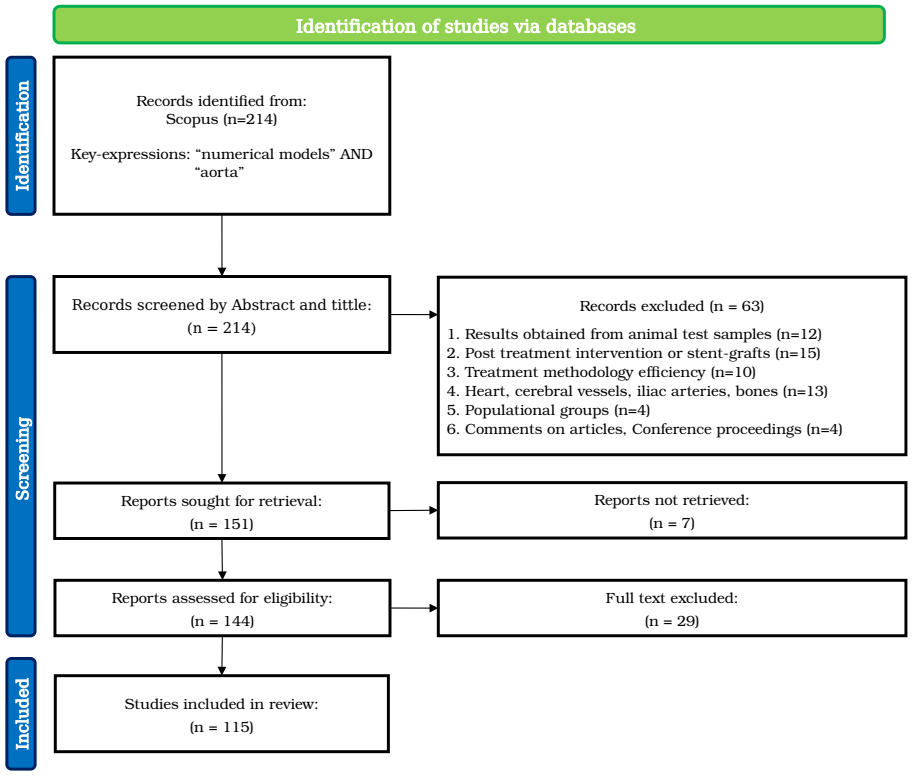

Figure 3.1: PRISMA flow chart of the systematic search strategy.

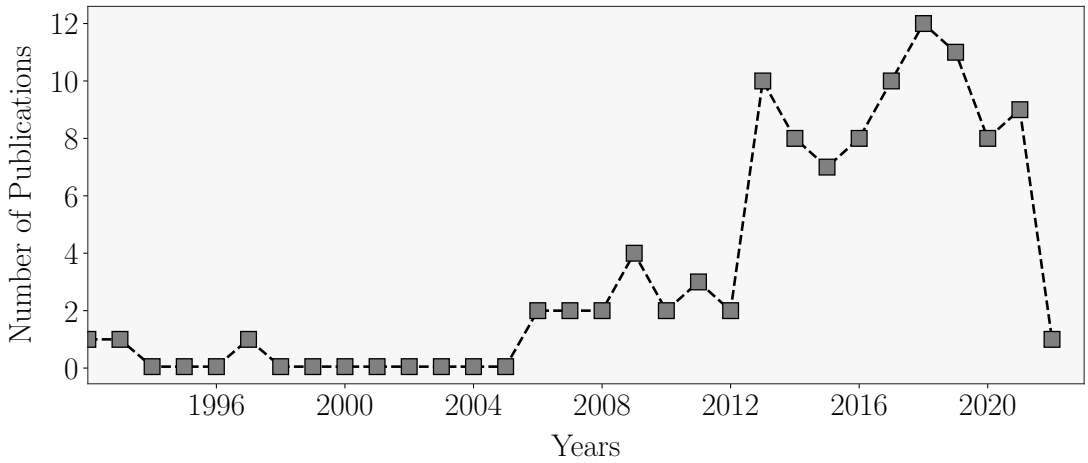

Figure 3.2: Evolution of number of publications per year.

The gathered results evidenced a growing interest in the presented topic over the last few decades (Fig. 3.2). The earliest report on the development of a human aorta numerical model was in 1992 by Owen [111] and until 2005 only two other works were found [143, 144]. From 2006 until the present the remaining 111 reviewed articles were published with 2018 being the year with the highest number of publications (12).

Regarding the studied anatomical region, it is evident a tendency to model either Ascending Thoracic Aortic Aneurysms (ATAAs) [145, 146], Abdominal Aorta Aneurysm (AAA) [147, 148] or Aortic Dissection (AD) [79, 149] since these present higher incidence

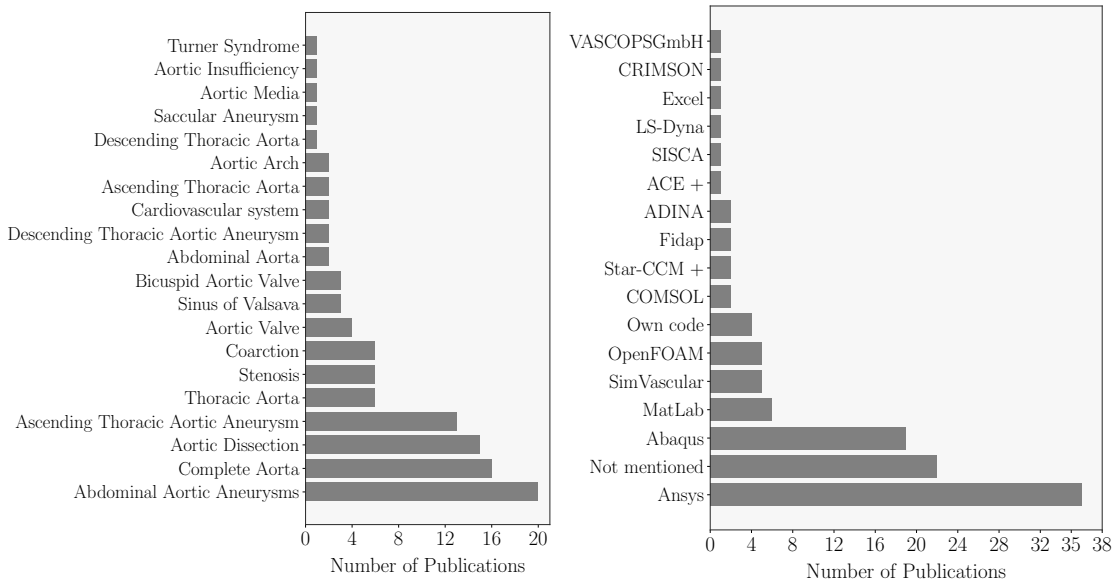

Figure 3.3: a) Studied anatomical regions. b) Selected softwares to perform the numerical modelling.

among aortic diseases and are potentially more catastrophic. Besides, several works recreated the biomechanics of healthy subjects [53, 122, 127] as it is relevant to identify the main differences between sane and diseased states. Regarding the chosen computing platforms, open-source softwares such as OpenFOAM [139] and SimVascular [52] were used around 10 % of the revised papers. The ANSYS finite element software was the preferred choice being used in 40 % of the works, particularly for CFD and FSI simulations. Abaqus was the second most used platform (20 %) being commonly applied to CSM [17, 138] or to FSI [114, 150] studies (coupled with the Abaqus flow module or with ANSYS CFD modules). The entirety of the studied anatomies and the utilized computing platforms are presented in Fig. 3.3.

Among the gathered results on the numerical modelling of human aortas, the authors identified four main search topics which will be discussed in the following order:

1. Biomechanical behaviour of healthy and diseased aortas;

2. Aortic wall characterization;

3. Risk assessment strategies and diagnosing techniques;

4. Numerical modelling augmentation.

For papers that overlapped two or more categories it was decided to address their work on the topic which the contributions were more relevant. Exceptions were made for works that presented important contributions over more than one topic.

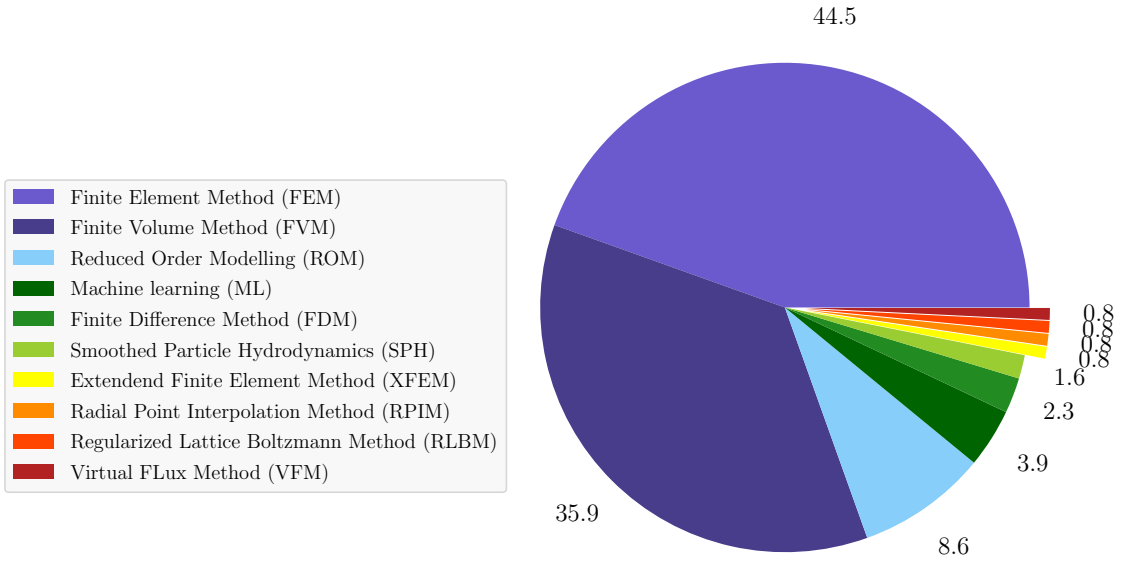

Figure 3.4: Relative frequency (values presented in percentage) of the identified numerical approaches. n = 115 articles.

3.3.2 Numerical approaches to model healthy and diseased aortas

Regarding the utilized numerical methods, our analysis revealed the usage of 12 different techniques. These and their relative frequency are depicted in Fig. 3.4. The vast majority of the reviewed works resorted to the FEM and FVM which are grid-based methods to solve partial differential equations and allows the calculations of CSM [33, 125, 151], CFD [17, 21, 152] and FSI [67, 145, 153] simulations. FEM solves the differential equation by diving the analysed systems into finite elements and their predominance can be supported by several aspects. The main reasons are the wide implementation in computational platforms, the ability to handle complex geometries and as today represents the preferred choice to perform CSM simulations. Also, it was reported the use of FEM in CFD simulations (Garlekin Method) [154, 155]. FVM integrates over finite-volumes the system governing equations and using the divergence theorem converts these volume integrals into surface integrals. Therefore, the physical properties in interest can be assessed as flux on the cell's surface which is meant to improve convergence. This fact explains the recurrent choice of Finite Volume Method (FVM) to develop CFD simulations. In Fig. 3.3, the top 5 reported platforms (Abaqus, ANSYS, SimVascular, MatLab, OpenFOAM) all primarily resort to FEM and FVM techniques to develop the available modules.

Several other grid-based methods were reported. Finite Difference Method (FDM) similarly to FEM and FVM also aims to solve partial differential equations, in this case by approximation to finite differences [143, 156, 157]. Extended Finite Element Method (XFEM) combines the formulations of generalized FEM and Partition of Unity Method and is mainly used in situations where grid refinement is not enough to achieve convergence. This feature is highly desirable in crack propagation simulations and coincidentally was used only in one work [158] to study the progression of AD. Regularized Lattice Boltzman

Method (RLBM) and Virtual Flux Method (VFM) were the only Cartesian grid methods depicted in our summary [159]. The last, virtually calculate fluxes to impose pressure conditions on body surfaces being able to reproduce their motion and the first represents a set of methods for CFD simulations. These techniques were combined by Fukui and Morinishi [159] to model the AV leaflets motion (VFM) and the transvalvular flow (RLBM).

The second most used technique was Reduced Order Model (ROM). Combining the works that resorted to 0D (4) [160, 161], 1D (6) [112, 162] and 2D (1) [163] models to recreate the hemodynamics of diseased and healthy aortas comprised a total of 12 reports. ROM techniques are useful to surpass computational complexity related problems by reducing the model degrees of freedom. In comparison with FEM or FVM simulations which can easily take days or even weeks to conclude, these techniques allow for accurate computations in a few minutes or even seconds of incomplete characterizations of flow fields and WSS distributions. The 0D models also known as electric analogues are often used in *in silico* simulations of the cardiovascular system as Boundary Condition (BC) that recreates the compliance and resistance of arterial blood flow. The 1D models are mainly used to study Pulse Wave Velocity (PWV) which is an important metric to assess aortic stiffness, as recommended in clinical guidelines [7]. These models have been applied in FSI simulations to estimate the hemodynamics [63, 164]. The 2D models are nowadays less utilized as 3D simulation became more accessible due to improvements in computer processing and the availability of 3D solvers. ML models have been growing in popularity over the last decades due to their capabilities of efficiently analysing data. Another advantage of ML tools is that they can be used in a wide range of applications. Our summary gathered seven reports where ML tools were developed. Regarding the use in cardiovascular medicine we found applications of these tools to improve the reporting time of Computed Tomography (CT) scans [16], estimate aortic reference configurations [122], act as wall constitutive model [165], predict the local strength of ATAAs tissue [166, 167] and evaluate the propensity to rupture of aortic tissue [168].

There were other two reported numerical techniques and both were meshfree methods which represent a new field of research opportunity as these methods eliminate the necessity of grid generation which can often be time-consuming and troublesome. One example is SPH that was used in 2 works and is a meshfree Lagrangian approach which discretizes the fluid as a set of moving particles and solves the governing equations for each of these particles [55, 169]. This method is suited to model large boundary displacements which may be useful to model aortic wall dynamics [55, 169]. Garlekin weak formulation and polynomial shape functions are used to develop Radial Point Interpolation Method (RPIM) models [170]. These also do not require grid generation as the polynomial functions are created based on a group of arbitrary nodes distributed along the computational domain. In Table A.1 are presented among the most relevant numerical results which are adequate to be calculated with each technique and their main advantages and limitations.

3.3.3 Biomechanical behaviour of healthy and diseased aortas

The study of the biomechanical behaviour of healthy and diseased aortas is an important research topic in the scientific community. To improve risk predictions of acute complications such as AAA [62, 171], AD [21, 57, 149], ATAAs [66, 172, 173], abdominal and aortic stenosis [69, 174], coarction [175, 176] or Sinus of Valsalva [159] and improve diagnose efficiency, a deep understanding of its development and growth is mandatory. To the date, the real pathophysiology of acute aortic complications is still not fully fathomed. It is expected that computational analyses could provide novel insights in this topic, as they enable access to complementary indices to quantity the risk of rupture such as WSS and WS distributions or other relevant metrics. The works that have been gathered in this subsection are focused on studying the characteristic hemodynamic and structural features of healthy and diseased subjects. In Table A.2 a summary of the analysed articles is presented.

3.3.3.1 Healthy aorta

The first work from the selected database reporting numerical modelling in healthy aortas was in 2006 by Del Gaudio, Morbiducci, and Grigioni [68]. In this work, CFD simulations considering a non-Newtonian fluid were performed on idealized geometries. The aim was to elucidate how numerical tools can be used to recreate the hemodynamics on the aortic arch. Their findings on the axial flow profiles revealed complex temporal variances and skewness towards the inner curvature of the arch. They also postulated that vascular geometry (*e.g.*, branching, non-planar, curvature, asymmetry) as it highly influences local fluid dynamics, could be the primary cause in the development of atherosclerosis. Later on 2011, Lantz, Renner, and Karlsson [177] reported the development of FSI simulations on Magnetic Resonance Imaging (MRI) driven geometric models. Patient-specific velocity profiles were used as an inlet BC and the external pressure exerted by surrounding vessels (*e.g.* pulmonary trunk and superior vena cava) was modelled as a linear elastic support BC on the outer wall. The model proved to be able to reproduce physiologically admissible flow patterns that presented close agreement with MRI data for lower velocity regimes. Marom et al. [178] also resorted to FSI simulations specifically to model the leaflet motion of the Aortic Valve (AV). The left ventricle and the aorta were modelled as rigid cylindrical tubes and the blood was considered slightly compressible to improve numerical convergence. The results evidenced that higher stresses appeared on collagen fibres and that Bicuspid Aortic Valve (BAV) induced flow turbulence and led to higher velocities and WSS magnitudes. Moosavi et al. [179] also used FSI formulations to simulate the blood flow on the Sinotubular Junction (STJ). A rigid model of the aorta and valve leaflets (peak systolic configuration) coupled with a contractile left ventricle mimicked the blood ejection into the aorta. Among their findings was the evidence of turbulence created at the left ventricle that traveled towards the aorta and higher WSS were found in the aorta. Šeta, Torlak, and Vila [61] performed patient-specific CFD simulations using FVM

to calculate the hemodynamics of the aortic arch. Larger velocities near the inner wall and the presence of clockwise helical flow and recirculation zones was evidenced. Chen and Luo [164] also performed FSI simulations on AV virtualizations but in this particular case, the blood flow was modelled with a ROM (1D). A good agreement was found with regular FSI simulations and showed that increased bending stiffness reduces the opening area and considerably increases flow resistance. On the other hand, excessively low values of bending stiffness are also not desirable as the leaflets may present flapping oscillation. Totorean et al. [56] performed CFD analysis on patient-specific models of the abdominal aorta and its branches. The geometries were reconstructed via CT data segmentation and comprised a total of 16 outlets. The authors postulated that the flow was almost entirely stable upstream of the abdominal aortic bifurcation. Downstream of the bifurcation, secondary blood flow with recirculation zones was formed. Also, WSS analysis revealed distributions with low, high and supra physiological magnitudes during the cardiac cycle and particles that presented long residence time near the wall, which is known to be a contributing factor to atherosclerosis.

3.3.3.2 Aortic aneurysms

Our database revealed that 12 works focused on studying the biomechanical behaviour of aortic aneurysms (*e.g.*, ATAAs, AAA, Descending Thoracic Aortic Aneurysm (DTAA) and saccular aneurysms). Gasser, Auer, and Biasetti [62] developed both CFD and CSM models based on FEM technique, to study the hemodynamics and structure of patient-specific AAA. Their results highlighted the existence of recirculation zones and increased WSS which was not found in healthy patients. Structurally-wise, it was shown that patients with a known rupture appeared to have superior Peak Wall Stress (PWS). Molony et al. [145] improved the methodology described in the previous work by developing a two-way FSI simulation, using partitioned schemes. Cong, Wang, and Liu [171] also developed two-way FSI to assess the effects of dilatation and aspect ratio on the hemodynamics of idealized models of AAA. The numerical results showed the formation of two vortices which were appointed as the dominant aspect of fluid dynamics. Moreover, elevated Oscillatory Shear Index (OSI) which is highly correlated with endothelial malfunctioning was also found. Callaghan et al. [173] performed CFD simulations in patient-specific geometries. The hemodynamics of saccular transverse aortic aneurysms was analysed. Higher WSS magnitudes and increased turbulence (vortices and recirculation) at the dilated region.

Pasta et al. [153] explored the differences in hemodynamics and WS induced by BAV using a two-way FSI approach and structured meshes. Evidence of an intrinsic disturbed blood flow was found in BAV patients, this contributes to an asymmetric and elevated WSS distribution. The inner layer was submitted to significantly higher principal stress and a greater inner-outer wall pressure gradient was found on the STJ area, supporting the

hypothesis that this region is the most susceptible to dissection. This was later also postulated by Numata et al. [58], where CFD simulations highlighted that abnormal WSS distributions promote medial degeneration which may be one of the main causes of AD development and that the STJ presented with higher values of OSI and WSS. Prahl Wittberg et al. [27] evaluated the influence of anatomical features on aortic hemodynamics. A two-phase mixture model to measure the evolution of red blood cells on the blood flow, Quemada non-Newtonian rheological model and 4 different groups (healthy, BAV, aneurysm and elongated transverse aorta) were considered to perform the CFD simulations. It was showed that anatomical variations had a great impact on flow patterns. On some occasions recirculation zones, characterized by lowered blood cells concentration and elevated WSS were found, in which the non-Newtonian behaviour of blood significantly altered the results. Jalalahmadi, Linte, and Helguera [172] following an approach similar to Prahl Wittberg et al. [27] investigated the influence of several geometrical factors (thickness, maximum diameter, turtuosity and asymmetry) on WS distribution of ATAAs. Several sets of idealized distinct geometries were generated to study each factor individually. They assessed that PWS increases with higher maximum diameter, asymmetry and turtuosity and decreased thickness. Yeh, Rabkin, and Grecov [22] performed patient-specific FSI simulations under normative and hypertensive conditions. The presented results implied that wall motion was highly influenced by blood pressure and local geometrical characteristics and that WS distribution were highly inter-patient heterogeneous. Campobasso et al. [66] also developed a two-way coupled FSI model to study the influence of peripheral vascular resistance and wall mechanical properties on WS. Their findings suggested that aortic stiffening contributed to abnormal WS distributions and predisposed the aortic wall to rupture. The increase of peripheral resistance translated into elevated blood pressure which makes the aortic wall more susceptible to rupture as well [22]. García–Herrera, Celentano, and Herrera [115] were interested in studying ATAAs biomechanics in Marfan syndrome patients, as this syndrome is known for weakening the aortic wall. CSM simulations were performed on idealized geometries resorting to a house build code, in which incremental homogeneous inner pressure (120–160 mmHg), aortic root motion and prestress BC were applied. The numerical results evidenced that Marfan syndrome presence induced significant changes in WS due to material properties degradation. Furthermore, the stress field was mainly circumferentially oriented which is justified by the spatial distribution and orientation of collagen fibres.

3.3.3.3 Aortic dissection

The real pathogenesis of AD is still an open debate. Several numerical models provided great contributions towards a better understanding of the main contributors to the development and progression of AD. Cheng et al. [76] evidenced that AD induced abnormal hemodynamics with the presence of recirculation zones both in True Lumen (TL) and False Lumen (FL). Geometrical features were also identified as a primary

cause of disturbed hemodynamics. Zhang et al. [21] focused on studying the underlying hemodynamics responsible for the longitudinal propagation of AD by developing CFD models with pulsatile flow-conditions. Tear[1] size and location impacted the FL blood flow patterns. Transmural pressure gradient, specifically in the circumferential direction, was suggested as one of the mechanisms responsible for the cleavage of lamellar units. Abnormal WSS distributions were proposed as the main cause of intimal tear initiation justified by the elevated values of Time-Averaged Wall Shear Stress (TAWSS) found near the tear. Ahmed, Dillon-Murphy, and Figueroa [180] studied the influence of anatomical risk factors in 14 idealized models of AD (tear size and location, number of entries and FL location). Evidence pointed out that FL increases flow resistance and revealed significant differences in the hemodynamics between the TL and FL. These differences diminish with the increase of the tear size. Shi et al. [149] also assessed the influence of tear location on hemodynamics with CFD simulations on patient-specific geometric models. Their results proved that aortic root proximity induces more turbulence in the FL. Pressure and WSS distributions seem to be well correlated with tear location since the tear usually occurred in regions where these quantities presented higher magnitude. Long Ko et al. [57] also investigated the hemodynamics of pulsatile flow on AD. Their results suggested that high WSS gradient between TL and FL acts as the main contributor to layer delamination and consequent AD progression and that high vorticity may be associated with intimal tear initiation and growth. Brunet, Pierrat, and Badel [158] investigated the most influential factors in AD propagation. CSM simulations on idealized models with two uniform thickened layers (media and adventia layers) were accomplished. Failure criteria based on Hashin failure theory, hyperelastic anisotropic constitutive models, and residual and prestresses were considered. The authors postulated that initial tearing is correlated with tissue fatigue and that tissue ultimate tensile stress can be achieved during intense workouts (*e.g.* weight lifting). Media layer strength appeared as a fundamental factor to AD propagation and the shear fracture was identified as a key process in delamination. Wan Ab Naim et al. [181] published a comprehensive overview on the topic of AD numerical modelling with focus on the biomechanical factors leading to the initial tear.

Besides the study on the effects of AD in the hemodynamics, the interaction between the blood flow and tear is also important as it may provide further insight into the mechanisms that induce the development of AD. Chen et al. [182] applied FSI simulations to study this interaction in an idealized aortic model that included the TL and FL was applied. The hemodynamic parameters at the TL and FL tend to homogeneity as the FL increase in size. Smaller FL presents lower velocities and may be stagnant. Also, stress analysis around the flap evidenced an elevated concentration of stress which may lead to AD progression.

[1] Entry point towards the FL

3.3.4 Aortic wall characterization

This section included the works with a focus on studying materials that can mimic the behaviour of biological tissues, studying the microstructure of the aortic wall and exploring methods to non-invasively estimate wall properties. The results of this analysis are summarized in Table A.3.

3.3.4.1 Cardiac phantom materials

Human and diseased aortas present complex anatomy and mechanical behaviours (*e.g.* heart motion, anisotropic hyperelastic wall, heterogeneity of wall properties and thickness, active contraction of the vascular smooth muscle cells within the aortic media layer). Access to materials able to mimic cardiovascular tissue is relevant for clinicians to practice, plan surgical procedures and validate devices or techniques. There is an ongoing quest to develop such materials, known as Cardiac Phantom Materials, that are capable of representing patient-specific human aortas.

Following this rationale, Cloonan et al. [183] performed experimental (Uniaxial, tear and dynamic tests) and *in silico* FSI tests on different cardiac phantoms. These phantoms had the particularity of allowing to measure results with PWV. The results suggested that the tested materials presented similar mechanical properties and similar pulse wave propagation. Nonetheless, the materials appeared to be less stiff under dynamic loading where the viscoelastic effects are more prominent. Moreover, the authors presented two different techniques to produce these cardiac phantom materials (investment casting process and 3D printing) and postulated that these materials have great potential to improve computational modelling approaches, clinical imaging modalities, and medical device design and bench testing. Comunale et al. [127] intended to answer the following questions: "Can a silicone prototype suitably mimic a biological aorta?"; "To what extent do the anatomical characteristics have to be detailed?". The differences in considering patient-specific geometries and material properties were assessed by implementing FSI simulations. It was assessed that geometrical factors highly influence the hemodynamic patterns and wall compliance was the dominant factor for the overall mechanical behaviour. They recommended both patient-specific geometries and material properties should be considered.

3.3.4.2 Wall microstructure

The aortic wall is a complex structure constituted by three distinct layers with distinct material properties, microstructure and morphology and adaptative to the mechanical environment. For instance, older patients present stiffer aortas resulting from increased collagen content and reduced elastin content. Another example of the nuances of this structure is how elevated WSS magnitude deregulates Matrix MetalloProteinase (MMP) synthesis which contributes to the cleavage of collagen fibres and consequent weakening

of the wall. Henceforth, studying the effects of the mechanical environment on the wall microstructure is relevant to better understanding the underlying mechanisms of the development of acute complications.

In 2008, Helderman et al. [148] developed a CSM model using FEM that aimed to estimate aneurysmal diameter growth. They chose an adaptative constitutive model which considered collagen degradation in regions where the stress surpassed a certain threshold. Although the elevated clinical interest in the presented model, no relevant results were presented due to the excessive number of limitations. Taghizadeh, Tafazzoli-Shadpour, and Shadmehr [125] created an aortic media lamellar model, constituted by adjacent stripes that alternated between representing elastic lamellae and the constituents comprised of two elastic laminas *e.g.*, collagen fibres and vascular smooth muscle cells. For hypertensive pressure conditions (160 mmHg), the results suggested elastin as a major load-bearing component in lower strain regimes. Increased strain induces the engagement of collagen fibres evidencing that these are the primary load-bearing component for higher strains. Also, the authors postulated that wall thickening and alteration of the microstructure promoted higher blood pressure. Thunes et al. [184] assessed the changes in the aortic wall microstructure, especially on collagen fibres, by imposing BC that recreated uniaxial tensile tests. CSM simulations on representative volumes of the aortic media were calculated. Mechanical properties heterogeneity were found to increase with stretch, mainly due to the spatial orientation of collagen fibres and activation. In 2017, the same group [138] suggested that under these conditions, aortic tissue failure is governed by cleavage of collagen fibres as they are stiffer and present inferior maximum stretch. Elastin fibres are more compliant, thus being the main contributor to hyperelastic behaviour of the aortic wall. Gültekin et al. [32] implemented an extension-inflation-torsion *in silico* test which intended to study the underlying mechanisms of development and progression of AD. The numerical model used an anisotropic wall constitutive model and failure criterion. In-plane shear stress originated by the heterogeneity of aortic wall mechanical properties was found to be the main contributor to initial tearing [158] and the second blood flow on the FL the main contributor to AD progression. Similar to Thunes et al. [138], Maiti et al. [185] developed a CSM virtualization of a mechanical test (biaxial tensile). The results also suggested cleavage of collagen fibres as the main contributor to the failure of the aortic wall. Under biaxial conditions collagen fibres in both directions were similarly loaded and that rupture is likely to occur in any direction as well. Wang et al. [99] simulated peeling and direct tensions tests aiming to study the effect of glycation[2] on the interlamellar bonding properties of medial elastin which is often compromised on CVD. The motivation behind this study was the reports of reduced risk of AD in patients with diabetes. Their findings suggested that glycation of arterial elastin reduces the risk of AD since it significantly increased the peeling force and interlamellar strength. Ban, Cavinato, and Humphrey [119] studied the effect of circulating blood flow on the propensity to dissect of different

[2]Covalent attachment of sugars, usually glucose to a protein or lipid.

regions and for that created a model that simulated a fluid injection on idealized volumes of the aortic media. Ultimate tensile stress was found to be highly dependent on local geometry and material properties. It was remarked that intramural swelling can lead to delamination and radially oriented structural components are extremely relevant to the delamination process, either to allow or arrest it.

3.3.4.3 Non-invasive estimation of wall material properties

When the interest of the simulation requires modelling the aortic wall, a suiting wall constitutive model needs to be chosen and calibrated. However, patient-specific materials properties are not directly available and are very challenging to estimate, and since the numerical results are highly dependent on these parameters, an accurate estimate is vital to produce accurate results. Estimating wall properties in a non-invasive way is still a challenge and further developments are needed. Our research gathered 8 works where methodologies to estimate *in vivo* or *ex vivo* mechanical properties were presented. Azadani et al. [120] implemented a MatLab methodology that adjusted the parameters of a bidimensional Fung Strain energy constitutive model to experimental stress-strain data obtained from the peel and direct tension tests performed on human ascending aorta and aortic sinuses test samples. Yang et al. [186] presented a novel method to estimate aortic wall compliance. This method resorted to uncoupled FSI simulations to estimate PWV. The cardiac circle was divided into 5 time steps and for each one, the following steps were executed and repeated until no significant differences were found: (i) the governing equations of the fluid domain are solved considering steady flow; (ii) the results of these simulations are updated on the solid domain (iii) and CFD simulations are newly performed with an updated computational domain accordingly to the previous structural analysis. The results suggested close agreement in the estimated PWV, according to what was expected in this particular case (552 $cm\,s^{-1}$). Therefore, the authors affirmed that this methodology could be a promising metric to assess if the used material parameters are adequate and may also be used to inversely estimate wall compliance. The group of Liu, Liang, and Sun [187] also developed a method to non-invasively estimate wall properties. In their first work [187] the multi-resolution direct search approach was presented which aimed to efficiently solve optimization problems.multi-resolution direct search was used to estimate a set of constitutive parameters (Holzapfel-Gasser-Ogden model) that best represents the patient-specific structural behaviour by minimizing the node to node differences between estimated (via CSM simulations) and synthetic "real" geometries. In the second work [188], the multi-resolution direct search approach was combined with CT data and the preliminary results were relatively close with experimental stress strain curves. Farzaneh, Trabelsi, and Avril [189] estimated local aortic stiffness from CT scans and found higher stiffness in ATAAs when compared to healthy subject. The inverse methodology applied in this work also allowed to identify of regional gradients of material properties which greatly impacted the numerical results.

3.3.5 Risk assessment strategies and diagnosing techniques

As mentioned in Section 3.1, current clinical guidelines for aortic disease diagnosis and treatment are fallible and unreliable which creates an urgent need for more robust risk assessment and diagnosing techniques. This section presents a summary of 16 works that explored the potential of numerical models to act as complementary tools of clinical diagnosis [190], and assessing the risk of acute complications by exploring their correlation with numerically obtained metrics such as PWS [151], WSS [19] or transvalvular pressure gradient [191]. The modelling option and results of the analysed articles are summarized in Table A.4.

3.3.5.1 Mathematical models as tools to assist clinical diagnosis

According to current clinical guidelines, PWV[3] is a useful metric to estimate aortic stiffness, cardiac output and even the presence of aneurysms and AD as they induce wave reflection and consequent changes in normal PWV. Therefore, this metric may be used as a diagnosis methodology. Numerically, excluding a few exception [183, 186] all the works that aimed to estimate this metric resorted to ROM as allows the computation of accurate and time-efficient results. Babbs [121] developed 0D models of the systemic circulation to measure cardiac output. The results presented a close agreement with *in vitro* data when constant wall compliance was considered. The introduction of nonlinear effects led to overestimations of wall compliance for higher pressure ranges. Sazonov et al. [162] aimed to develop cost-effective aneurysm diagnosing techniques, based on assessable measurements and pressure and/or velocity waveforms obtained via 1D modelling. This 1D model was validated with a representative experimental model of blood vessels and aimed to assess the changes in PWV between healthy and diseased subjects. Compliance gradients were appointed by the authors as the only parameter assessed via 1D modelling able to efficiently indicate aortic wall strength. Kizilova and Mizerski [163] developed a 2D numerical model of the aorta using tapered tubes to estimate PWV. The model was able to predict high reflection sites that are potentially damaging to the aortic wall.

Badeli et al. [192] applied FEM modelling to simulate the propagation of electrical currents across the thorax and identified trans-thoracic impedance in order to diagnose AD. The numerical results were analysed by Bayesian stochastic models. The model virtualized an impedance cardiography exam[4] and the results proposed that the Bayesian approach outperformed conventional impedance cardiography multi-sensors technique.

Aneurysmal growth [193], intimal tearing initiation [184] and even propensity to rupture [19] were closely correlated with abnormal WSS distributions and large magnitudes. The group of Bopp et al. [28] developed an experimental facility where flow measurements could be obtained with MRI technology and *in vitro* CFD models. The

[3]Measures how the shock wave generated by the closing of AV propagates along the aorta.

[4]Measures how changes in aortic blood volume and flow influence transmission of a known electrical current across the thorax.

objective was to provide an extensive reference database of aortic hemodynamics obtained with validated numerical simulations. Therefore, improving the accuracy on WSS calculations of magnetic resonance velocimetry as it assists in surpassing limitations related with MRI low spatial resolution. In their first work [194] a comparison between laser Doppler velocimetry, magnetic resonance velocimetry and CFD estimation of WSS was performed. Bauer et al. [194] suggested that laser Doppler velocimetry technique could indeed be the gold-standard to WSS estimation. Despite that, it is still limited by the low spatial resolution of MRI.

Afterwards Bopp et al. [28], assessed the differences in flow measurements obtained via magnetic resonance velocimetry and CFD. The turbulent nature of the blood flow was better captured by magnetic resonance velocimetry. Bopp et al. [28] addressed the fact that using more robust turbulence models (*e.g.*, Large Eddy Simulations (LES) rather than Reynolds-Averaged Navier-Stokes (RANS) equations) may overcome this limitation. The group of Sotelo et al. [155] developed a novel method to estimate WSS distributions, that consisted in post-processing velocity fields (obtained with MRI) resorting to CFD models. In this work, evidence that wall motion highly impact WSS distribution was presented. Later on 2017 [154], this methodology was augmented by allowing the calculation of different WSS components.

The last two works focused on improving the efficiency of maximum diameter measurements [16] and auscultation exam [190]. Rueckel et al. [16] suggested an ML tool that estimated the diameter in nine important anatomic locations automatically using CT data. This tool obtained results similar to specialists with a considerable reduction in reporting time (13 to 2 min) and may be useful to assist clinicians with aneurysm diagnosis. Murmur properties were correlated with pathological states by Zhu, Seo, and Mittal [190] through the analysis of CFD simulations. Murmurs are caused by flow abnormalities and can be detected with stethoscopes. Thus, understanding the correlations between murmurs and different pathologies can improve auscultation capacity to diagnose CVD.

3.3.5.2 Risk estimation of aneurysm rupture

The rupture phenomenon of aneurysms was studied in six different works [19, 124, 151, 195]. Doyle et al. [195] experimentally (silicone test samples) and *in silico* tested idealized models of the abdominal aorta until rupture. Inflation tests were virtualized resorting to CSM simulations. The aim was to identify the probable location of rupture in AAA using Von-Mises Stress and PWS criteria. Material properties were identified by fitting different constitutive models with uniaxial tensile test data. Third-order Ogden model was found to be the constitutive model that produced better approximations ($R^2 = 0.9812$). Numerical results showed that higher stress appeared at regions of higher strains rather than higher diameter. The PWS rupture criteria presented a good agreement with experimental data. Shang et al. [151] performed CSM simulations on patient-specific DTAA models with the objective of assessing the correlation between aneurysm growth and PWS. This

metric presented a stronger correlation with aneurysm growth than maximum diameter and was suggested as a possible indicator of acute complications. Condemi et al. [18] developed a numerical model using CFD assisted by MRI data to assess the influence of abnormal hemodynamics on rupture risk. They analysed both numerical results and experimental data from bulge inflation tests. Higher flow eccentricity was correlated with higher and more disturbed WSS distributions. The areas of higher WSS were coincident with the region of flow impingement and also correlated with higher values of TAWSS and OSI which were previously correlated with a high probability of rupture [58]. However, a direct correlation between WSS and wall strength was not found, possibly suggesting that further structural analysis is also required. On the 31 analysed patients with CFD simulations by Pasta et al. [193] it was found higher WSS magnitude and pressure index in all ascending aorta for BAV patients and evidence of PWS being a great candidate to predict the risk of ATAAs rupture. Also, Pasta et al. [19] assessed correlations between biomarkers (*e.g.*, MMP, TIMP and miRNA), WSS (obtained via CFD) and aortic strain (obtained from post-processing CT data) in ATAAs. Evidences of higher WSS and wall strain from the STJ to the mid ascending aorta were presented. The increase of WSS was correlated with higher MMP synthesis which can deregulated the homeostasis of the aortic wall and promote elastin and collagen degradation. A combination of biomarkers (extracted from blood samples) and non-invasive evaluation of WSS distributions may assist in rupture risk assessment of ATAAs.

The use of ML tools to estimate rupture risk in ATAAs was reported in three articles. Luo et al. [168] used a similar technique to Azadani et al. [120] and Doyle et al. [195], in order to fit constitutive models to tension-strain data from bulge inflation tests. The estimated material parameters and geometric parameters were analysed by the developed ML tool that classified the data into rupture and non-rupture groups. This analysis suggested that the members of the ruptured group presented similar material properties. One important remark is that were identified strong correlations between tissue strength and pre-rupture response features. He, Avril, and Lu [167] developed two ML models which were also trained with tension-strain data collected through *ex vivo* inflation tests on ATAAs tissue samples (rupture was ensured). The first aimed to identify the locations of higher tension buildup along the aortic wall. The second estimated ultimate tensile stress in the identified regions. The results suggested that local rupture strength can be reliably estimated from the pre-rupture features as postulated by Luo et al. [168], matching 13 out of 15 estimated rupture sites with experimental data [166]. Liu et al. [124] identified the regions more prone to rupture through the implementation of ML tools trained with CSM driven systolic and diastolic geometries. For that, CSM driven systolic and diastolic geometries were used to train the ML tool whose objective was to act as rupture criteria. The presented results showed that this tool outperformed other rupture risk estimation methods on the available and limited sample.

3.3.6 Numerical modelling augmentation

Numerical modelling also presents some limitations that limits it's introduction into clinical practices. This section compile the results from 48 articles that implemented new techniques to reduce reporting time or improve accuracy (18), assessed if certain physiological features such as turbulence or the non-Newtonian behaviour of blood (25) are relevant to be considered and studied the sensitivity of the numerical results to inlet conditions (6). The results are summarized in Table A.5.

3.3.6.1 Relevance of modelling certain physiological features

The results we gathered mainly focused on determining wall motion, patient-specific material properties, turbulence and non-Newtonian blood behaviour impact on the numerical results.

The aortic wall possesses hyperelastic properties mainly due to the presence of elastin fibres [138] which allows the aorta to expand and contract during the cardiac cycle. This effect is known as the Windkessel effect and contributes to reducing the differential between systolic and diastolic pressures, as well as, assisting with blood flow. Given that, two questions arise from this rationale. Firstly, diseased aortas usually present stiffer aortas and lower diameter variations over the cardiac cycle. The studied group by Mendez, Di Giuseppe, and Pasta [123] presented an average variation of 4.2 ± 2.4 %. It may be not significant to consider as it introduces complexity to the model without relevant impact on the numerical results. On this topic, Lantz, Renner, and Karlsson [177] compared the results of CFD and FSI simulations and found that instantaneous WSS are extremely influenced by wall motion. However, averaged values like TAWSS and OSI seem to not be significantly influenced by FSI simulations. Marom et al. [196] performed the same comparison on idealized models of the aortic root and concluded that aortic compliance did not impact the transvalvular hemodynamics. Alimohammadi et al. [64] noticed a 15 fold increase in reporting time from CFD to FSI models. They also found that FSI driven WSS distributions presented a closer agreement with *in vivo* patient-specific data. Wolański et al. [113] found that rigid wall simulations tend to overestimate blood pressure and WSS magnitude. Mendez, Di Giuseppe, and Pasta [123] also assessed the differences between CSM, CFD and FSI simulations. Their results suggested that both WSS and WS presented significant differences between the simplest approaches (CSM and CFD) and FSI models. As reported by Nowak et al. [67] these differences were greater for more compliant aortas. Bäumler et al. [79] studied the importance of modelling realistic wall and tear motion to AD hemodynamics and also found that FSI simulations contributed to improving the agreement of numerical results with MRI data.

Assuming that wall motion is indeed relevant to the model, it becomes necessary to choose a wall constitutive model which requires the estimation of material properties. The assessment of these parameters is still a challenging objective to fulfil and to this date, there is still no gold-standard methodology to perform this task. Thus, it became

relevant to study the impact of considering populational averaged values. Doyle et al. [146] developed CSM models with patient-specific geometries of AAA. The objective was to evaluate the numerical variations when patient-specific constitutive parameters are used instead of averaged values. The results evidenced significant differences, namely increased PWS by 67 %, wall strain by 320 % and displacement by 177 %. Another interesting finding was that several constitutive models overestimated the ultimate tensile strength of the tissue. Lucio et al. [14] tested the relevance of considering the three aortic wall layers in particular if the intima layer also has a considerable load-bearing effect by developing CSM digital twins of uniaxial tensile tests. Their analysis showed that the intima layer is stiffer among the layers and contributes significantly to the load-bearing of the wall. Significant differences were found in considering three or just one layer, about 30 % concerning the stresses and a maximum of 53 % in displacements.

On the topic of aortas blood flow, there are also open questions regarding the modelling of flow rheology and turbulence in large arteries. Although blood presents non-Newtonian behaviour which more evident for lower velocity regimes, we found contradictory evidence in our research regarding this topic. For instance, in the works of Lou and Yang [143], Mourato et al. [60] and Carneiro et al. [147] the authors depicted that using rheological models not significantly altered the numerical results in ATAAs, AAA and healthy aortas. Alimohammadi et al. [64] and Febina, Sikkandar, and Sudharsan [80] studied the same topic in AD and saccular aneurysms and found that modelling the non-Newtonian behaviour of blood impacted the numerical results. This evidence suggests that the pseudoplastic and viscoelastic features of blood are only relevant for lower shear rates which are uncommon in large arteries but that do occur in stagnant flow and recirculation zones. Regarding turbulence, the vast majority of numerical models opted for imposing laminar flow. However, it is known that in diseased and healthy (although rare) aortas turbulent flow may occur during instances of the cardiac cycle. Zhu, Seo, and Mittal [190] and Chen et al. [139] used Direct Numerical Simulations (DNS) to model the turbulence in abdominal aortic stenosis and idealized geometries and found no significant differences in the numerical results. The group of Khanafer et al. [81] developed CFD models using the Galerkin method and suggested that the turbulence had a significant impact on pressure distributions [197]. Also, Lantz et al. [198] used LES modelling to study the correlation between turbulent kinetic energy and abnormal flow on stenosed models. They found variations of around 15 % on turbulent kinetic energy estimations and good agreement with MRI data when turbulence was modeled.

3.3.6.2 Novel numerical techniques

Despite the capabilities of numerical modelling to predict the behaviour of complex biomechanical systems, their implementation into clinical practices is still very limited with few examples of success. Possible reasons for this fact are presented and discussed below. Here is presented works aiming at the development of numerical models using

innovative computational techniques (*e.g.*, SPH, ML, ROM) and exploring new methods to improve the efficiency of FEM modelling.

Respecting to FEM modelling improvements, in our research we found efforts on developing novel and more realistic BC, more robust methods to model the aortic wall and develop new meshing processes. Starting with BCrelated works, Stevens, Lakin, and Goetz [199] developed an equation that modelled the cardiac output towards the ascending aorta. The numerical results presented a close agreement with *in vivo* data after calibration. Aboelkassem, Savic, and Campbell [160] created a simplistic mathematical model aiming to recreate the coupling between the left ventricle and the ascending aorta by recreating the dynamics of the AV. Koltukluoğlu and Blanco [200] applied optimization algorithms to estimate inlet and outlet BC. The proposed approach provides a systematic strategy to improve the model predictions regarding clinically relevant hemodynamic data. The method provided physiological flow patterns with reduction of 4-D flow MRI measurements noise and outperformed regular CFD simulations. Attaran, Niroomandoscuii, and Ghalichi [201] proposed a novel outlet BC for compliant arteries. This BC consisted of the addition of a tube composed of porous media at the outlets. This condition aimed to recreate the reflection of pulse wave promoted by the downstream vasculatures and presented higher computational efficiency than (1D-3D) models.

Liang et al. [122] developed an ML tool trained with CSM data to estimate the zero-pressure geometries of patient-specific aortas. Aortic reference configurations are important to accurately represent the complex stress state of deformed aortas. Ben-Or Frank et al. [33] used second-harmonic imaging microscopy data to assist a new micromechanical model with patient-specific data of collagen fibres orientation, to better predict the mechanical response of the aortic wall. They postulated that the developed methodology can capture the overall response of soft tissue by resorting to fewer constitutive parameters. It was also found that increased stiffness for larger strains (j shaped curve) and bad approximations for the supra-physiological loading range. Liu, Liang, and Sun [165] presented an ML tool surrogate of traditional wall constitutive models. This tool was trained with data from 63 ATAAs human samples and outperformed well-recognized models such as the Holzapfel-Gasser-Ogden model.

On meshing related topics, Santis et al. [202], Suito, Ueda, and Sze [156] and Bols et al. [114] explored the application and generation of structured grids on patient-specific aortic models. Silva et al. [170] compared the results of RPIM and FEM models of AAA. The results of both approaches were very similar. However, the meshing process in RPIM is less complex which constitutes an advantage to the approach. Capellini et al. [17] presented a mesh morphing technique to assist and facilitate the meshing process for FEM simulations. Valente et al. [52] developed a new method to assist the construction of both solid and lumen domains for FSI analysis, using SimVascular. The opportunity to independently choose element size and the introduction of prestress methods contributed to a reduction in computational effort.

Regarding the development of new techniques, there were several examples of works

focusing on developing and improving previously developed ROM. In 1992 we found the first reference to these applications. In this work, Owen [111] developed a 1D model of the aorta and AV. At the inlet, a pressure evolution over time was applied to mimic cardiac pulse. At the outlet, the flow was calculated using a resistance BC. They reported results on blood pressure, PWV, wall properties and axial velocity and radius variations which presented a good agreement with theory and empirical data. Geertsema et al. [161] presented an electric analogue of the cardiovascular system (0D model) and found good agreement with *in vivo* data on the numerical results. Matthys et al. [110] compared *in vitro* measurements on a silicone model with results obtained from 1D models of the cardiovascular tree. The main purpose was to study the effects on pulse wave propagation of energy dissipation at vessel bifurcations. The numerical model presented small errors in pressure and flow measurements, thus proving to be able to accurately capture the main hemodynamic features. Salvucci et al. [203] estimated planar WSS using 1D models of the thoracic aorta. The group of Bollache et al. [112] developed 1D models based on patient-specific data obtained via CT and MRI scans. The purpose of both works [112, 204] was to estimate PWV which may be used to assess aortic wall compliance. The results were in a good agreement with *in vivo* data. Chen and Luo [164] coupled a 1D model of the trans valvular aortic flow with a FEM model of the leaflets and compared the results with a regular FSI simulations. The proposed 1D model presented good accuracy while reducing the computational time. Biancolini et al. [63] performed the same analysis for ATAAs models and found similar conclusions. Hackstein, Krickl, and Bernhard [54] developed 0D models of the cardiovascular system to extract correlations between model parameters (estimated with AutoRegressive Moving-Average models) and pathological flow conditions.

Besides ROM, two other works from Arico et al. [55] described the use of innovative techniques. These works resorted to SPH technique to model AAA hemodynamics. Interestingly, although the aortic wall was not considered, a displacement field obtained via CT Angiography was applied to the outside surface of the lumen. The results showed that velocity fields in rigid wall simulations underestimated blood pressure and overestimated velocity magnitude. Maximum WSS was similar but differed in distribution [169].

3.3.6.3 Sensitivity analysis

Accuracy is crucial for biomechanical applications of numerical models. Thus, it is of great relevance to perform sensitivity analysis to understand how the conditions we are choosing in developing numerical models impact the results. He and Li [157] evaluated that in CFD simulations using pulsatile inlet conditions produce better results and suggested that these should be as physiologically accurate as possible. Taelman et al. [150] performed FSI simulations on idealized aortic models and studied the effect of grid spatial resolution. They suggested that the undesirable effects of numerical dissipation and diffusion are mainly ruled by spatial discretization. Mesh sensitivity analysis are

recommended in FEM modelling and was also suggested that higher-order discretization schemes assist on accuracy improvement. Nisco et al. [152] studied the influence of inlet BC on Low-Density Lipoproteins (LDL) transport and found that realistic inlet BC produced a closer agreement with *in vivo* data. Mariotti et al. [53] focused on studying the numerical results sensitivity of CFD and FSI simulations to the inlet waveform (cardiac cycle duration and stroke volume). The results proved that stroke volume strongly influenced the numerical results. Contrary to the stroke volume, the period of the cardiac cycle had a moderate impact and the interacting effect of the two was insignificant. Ascending aorta presented less sensitivity to period and stroke volume than the aortic arch and descending aorta. Also, when the wall motion was considered the standard deviation was not significantly changed. The same group published two other works one the same thematic where they studied the influence of inlet waveform uncertainties [205] and spatial distribution of inlet velocity fields [206].

3.4 Numerical modelling applied to clinical practices

The present systematic review followed the PRISMA guidelines with the objective of understanding which numerical techniques have been applied to simulate the the blood and aortic wall interaction in healthy and diseased aortas. Furthermore, the intrinsic reasons behind the lack of implementation of these models in real-life clinical practices were explored.

The gathered results support the ability of numerical models to provide novel insightful information on the development and growth of several pathological conditions such as ATAA [53, 80] or AD [32, 57, 99]. Numerical simulations assisted by medical imaging data showed capabilities of estimating *in vivo* aortic wall material properties [120, 187], WS [22, 154] and WSS distributions [122, 153]. Furthermore, several groups proved that simple geometrical criterions can not reliably predict the risk of acute events [17, 63] and suggested stronger hemodynamic [19, 58] and structural [18, 21] based metrics for the risk assessment of acute complications. However, these tools are not widely implemented in clinical practices and three aspects were identified as the most relevant to lack of presence in real-life medical applications of numerical modelling.

The first aspect is the need for higher levels accuracy on the numerical results. Numerical modelling is highly impacted by the chosen initial conditions (*e.g.* initial geometric model, definition of the fluid and solid domains) and applied BC. To systematically produce proper results these conditions must be rigorously selected and as approximated as possible to the *in vivo* patient-specific conditions. This necessity was evidenced by He and Li [157], Taelman et al. [150] and Mariotti et al. [53] which have shown that numerical results are significantly affected by slight variations on inlet BC, either on spatial or time distributions. Comunale et al. [127] and Wolański et al. [113] proved that patient-specific constitutive parameters induce closer agreement between numerical results and *in vivo* data. On one hand, is still missing a concrete understanding of which biomechanical

features of diseased and healthy aortas are relevant to be modelled. For instance, on Subsection 3.3.6 was discussed the contradictory evidence that was found on what respects to modelling the flow rheology [60, 147], turbulence [60, 139, 198] and wall dynamics [67, 177]. Another contributor to inaccuracies is the often disregard of features that may significantly impact the numerical results such as wall thickness and mechanical properties heterogeneity, aortic root displacement and external pressure exerted by surrounding vasculatures (*e.g.* pulmonary trunk and superior vena cava). For instance, evidences of increased longitudinal stress at the ascending aortic outer curve when modelling realistically heart motion were presented by Mendez, Di Giuseppe, and Pasta [123]. Nonetheless, more work is needed to address the real impact of including such simplifications. On the other hand, to this day is still hard to estimate *in vivo* patient-specific parameters required to model the structural behaviour of the aortic wall, as well as, inlet and outlet BC. Hence, it represents a complex task to assist numerical calculations with accurate initial conditions which is crucial to achieving good numerical results. Great efforts have been presented to improve the accuracy of numerical models and one common idea is to allow the model to estimate these requirements through the use of optimization algorithms. Take as an example the works of Liu et al. [188] and Koltukluoğlu and Blanco [200] that implemented inverse methodologies to estimate aortic material properties and inlet and outlet BC from MRI data, respectively. MRI and CT data usually present noise and suffer from low time and spatial discretization which also act as a source of uncertainties in the results. Therefore, even using these inverse methodologies which nowadays seem to represent the best solution can still lead to an offset between the estimated and real parameters.

The second major limitation is the elevated reporting time most of the identified techniques require to produce the numerical results. In common clinical practices, often clinicians deal with time-sensitive situations, where the mortality rate increases rapidly [138] and there is no option to wait for days or weeks to generate results. Biancolini et al. [63] also have pointed the high computational cost required to perform viable simulations as one of the biggest bottle-necks towards clinical implementation. Mesh generation is often one of the most time-consuming steps in grid-based models such as FEM or FVM. Furthermore, in 2D and 3D simulations, the calculation itself is also a highly time-consuming step due to the elevated amount of performed calculations and domain subdivisions. Also, these models regularly deal with convergence related problems and the patient to patient adaptability usually requires time-consuming calibration processes. Still regarding the reporting time, as expected we found evidence that computational effort grows with model complexity. For instance, laminar simulations take less time to compute results than turbulent simulations. FSI simulations can lead to a 15 fold increase in computational time as reported by Alimohammadi et al. [64]. This also enhances the need for studying the equilibrium between model complexity and simulation time. On this topic, there also have been great efforts to improve the efficiency of numerical models. Santis et al. [202], Suito, Ueda, and Sze [156] and Bols et al. [114] explored the application of

structured grids which are known for reducing computational effort as it requires fewer elements to achieve convergence. Aricò et al. [169] and Silva et al. [170] implemented meshless models and reported significant reduction in computational effort. ROM was also suggested as efficient techniques to estimate hemodynamics accurately and reduce reporting time [161, 164, 203, 204]. Liu, Liang, and Sun [187] proposed a new optimization method (Multi-Resolution Direct Search) designed to reduce the high computational effort inherent to inverse methodologies. Also, Liang et al. [122] suggested the use of GPU (instead of CPU) based methods such as SPH [55, 169]

Lastly, the third major limitation and possibly the most relevant is the lack of extensive clinical trials that prove the efficiency of these tools to precisely predict the development of severe pathological conditions. Studies on large patient cohorts are still needed and essential to the implementation of numerical models in clinical guidelines. Only 12 % of the works analysed in this review performed numerical validation with patient-specific *in vivo* data and the majority (76 %)did not present a meaningful validation process which also contributes to the lack of proof of numerical modelling efficiency.

To end with, it is pointed out that the present systematic review was limited to only one electronic database with the exclusion of MSc and PhD thesis. In future analyses one may extend the selection of databases where the initial research is realized and include MSc and PhD thesis. Also regarding future works, the authors will seek to further understand the biomechanics of the most common aortic diseases (ATAAs, AAA and AD) and explore which rheology and turbulence models, BC and numerical techniques and approaches produce better results.

3.5 Main remarks

From this systematic review the following remarks can be drawn:

- Among the relevant data numerical models can provide it is highlighted: (i) the WSS and WS based metrics which were strongly correlated with aortic microstructure (mys)functioning and elevated propensity to rupture; (ii) PWV due to its ability to evaluate aortic stiffness by clinical guidelines; (iii) and wall strain;

- 1D modelling and ML were the next most selected techniques. 1D model proved to allow quick computations of PWV on a patient-specific basis. ML presented a wide range of applications that outperformed usual methods while reducing the computation time;

- From the review, FEM and FVM are the two preferred techniques to perform CSM and CFD patient-specific simulations, respectively. These techniques were collectively chosen in around 80 % of the analyzed works, are widely implemented in commercial and open-source computing platforms and allow the use of complex geometric models such as diseased aortas.

- The general consensus is that the gold standard technique to model the hemodynamics and structure dynamics of the aortic wall is the FSI approach, which has the limitation of high compuational cost.
- Accuracy, computing time and lack of validation were the main identified contributors to the lack of application of numerical models in real-life medical applications. Accuracy issues are mostly correlated with poor selection of rheological, turbulence or wall constitutive models and difficulties in correctly assessing the *in vivo* patient-specific parameters for these models and patient-specific geometric models or BC. Excluding ROM, computing 3D hemodynamics or structural data can easily take days or even weeks, particularly in grid-based methods, which is not suited for time-sensitive situations. Also, there is a lack of both numerical validations as assessed by the GRADE approach (only 12 % of the total works presented numerical validation against *in vivo* patient-specific data) and extensive clinical trials;
- To this date, there is still a lack of reports on the bibliography of studies on the impact of considering wall thickness and material properties heterogeneity, surrounding aortic structures, internal pressure of the human body, calibration of impedance based outlet conditions and aortic root motion on the numerical results.

Chapter 4

Comparison of Zero Pressure Geometry and Prestress Methodologies in Cardiovascular Fluid-Structure Interaction Analysis

The work presented in this chapter was published in 2024 by Elsevier: **Mourato, A.**, Valente, R., Xavier, J., Brito, M., Avril, S., Tomás, A. C., & Fragata, J. (2024). Comparative analysis of Zero Pressure Geometry and prestress methods in cardiovascular Fluid-Structure Interaction. *Computer Methods and Programs in Biomedicine*, *257*, 108475. https://doi.org/10.1016/j.cmpb.2024.108475.

Abstract: Modelling patient-specific aortic biomechanics with advanced computational techniques, such as Fluid-Structure Interaction (FSI), can be crucial to provide effective decision-making indices to enhance current clinical practices. To effectively simulate Ascending Thoracic Aortic Aneurysms (ATAAs), the stress-free configuration must be defined. The Zero Pressure Geometry (ZPG) and the Prestress Tensor (PT) are two of the main approaches to tackle this issue. However, their impact on the numerical results is yet to be analysed. Computed Tomography Angiography (CTA) and Magnetic Resonance Imaging (MRI) data were used to develop patient-specific 2-way FSI frameworks. Three models were developed considering different tissue prestressing approaches to account for the reference configuration and their numerical results were compared. The selected approaches were: (i) ZPG, (ii) PT and (iii) a combination of the PT approach with a regional mapping of the material properties (PTCAL). The pressure fields estimated by all models were equivalent. The estimation of Wall Shear Stress (WSS) based metrics revealed good correspondence between all models except for the estimated Relative Residence Time

(RRT). Regarding ATAA wall mechanics, the proposed extension to the PT approach presented a closer agreement with the ZPG model than its counterpart. Additionally, the PT and PTCAL approaches required around 60 % fewer iterations to achieve cycle-to-cycle convergence than the ZPG algorithm. Using a regional mapping of material properties in combination with the PT method presented a better correspondence with the ZPG approach.

Keywords: Ascending Thoracic Aortic Aneurysm (ATAA), Fluid-Structure Interaction (FSI), Prestress Tensor (PT), Zero Pressure Geometry (ZPG).

Contents

4.1 The role of the stress-free configuration

The formulation of FSI models for simulating Ascending Thoracic Aortic Aneurysms (ATAAs) biomechanics involves a pivotal step addressing the unavailability of the stress-free configuration [207]. This limitation stems from the continuous loading of the aorta throughout the cardiac cycle, making the reference configuration absent from *in vivo* imaging data. To overcome this challenge, two of the main tissue prestressing methodologies reported in the literature, are the Zero Pressure Geometry (ZPG) [122, 208, 209] and Prestress Tensor (PT) [52, 79, 115]. The former has a wide range of proposed algorithms that solve minimisation problems to estimate the stress-free configuration, i.e., the configuration that yields the image configuration when the diastolic hemodynamic loads are applied. Some examples are the reverse displacement algorithm proposed by Raghavan, Ma, and Fillinger [130] and the modified updated Lagrangian formulation suggested by Gee, Förster, and Wall [210], which are capable of completely describing the initial stress-strain state albeit the intricacy to implement. The latter, proposed by Hsu and Bazilevs [129], uses an additive decomposition to split the second Piola-Kirchhoff stress tensor into the stresses induced during the cardiac cycle and the stresses balancing the diastolic hemodynamic loads. While generally more straightforward to implement than ZPG algorithms, this methodology focuses only on the stresses neglecting any insights into the pre-deformation.

Despite their shared purpose, these approaches may result in varying outputs in ATAA simulations. However, the impact of employing ZPG or PT methodologies remains unclear in the current literature. This chapter provides a comprehensive systematic comparative analysis of quantitative parameters associated with different prestressing algorithms and their effects on the numerical results obtained with 2-way Fluid-Structure Interaction (FSI) models. Three ATAA patients were considered, and three simulations were performed on each segmented anatomy, differing on the used prestressing methodology: (i) ZPG; (ii) PT; and (iii) a novel suggested approach combining the PT algorithm and a regional mapping of calibrated material properties (PTCAL). These models were implemented in SimVascular [211]. The impact of resorting to different tissue prestressing algorithms was evaluated on: (i) the pressure field, as it is the major contributor to the hemodynamic loads on the aortic wall; (ii) Wall Shear Stress (WSS), due to the known impact on the development and progress of cardiovascular diseases; and (iii) the maximum principal strains and stresses, which are relevant to the estimation of rupture risk.

This chapter is organized as follows: in Sections 4.2 and 4.3 the development of the FSI model and the numerical implementation of the tissue prestressing methods are presented; the numerical results are presented in Section 4.4 and discussed in Section 4.5; lastly, in Section 4.6 the main remarks of this work are summarized.

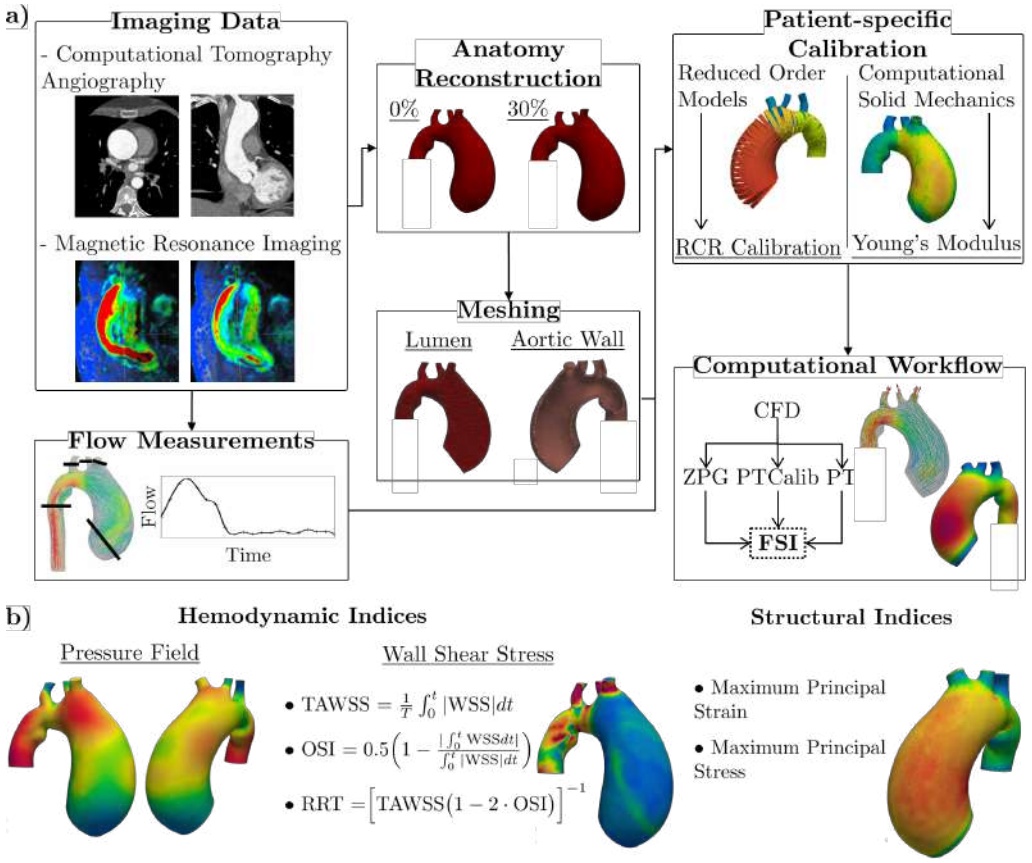

Figure 4.1: Schematic chart of the employed methodology to study the influence of different tissue prestressing methods on the results of FSI simulations of ATAAs. a) CTA and MRI data were used to extract the geometrical model and inform boundary conditions. This information assisted the development of a FSI computational framework on which the ZPG, PT and PTCAL methods were applied. b) The influence of these methods on the numerical results was investigated by the analysis of hemodynamics indices and structural indices.

4.2 Fluid-structure interaction model

An overview of the computational FSI framework adopted here, as well as, the proposed analysis are presented in Fig. 4.1. Two females and one male patients of 69, 48 and 70 years old with ATAA were considered under the scope of the AneurysmTool project (DOI: 10.54499/PTDC/EMD-EMD/1230/2021). Additionally, two of the studied patients (A and C) presented a bovine aortic aorch which is a common variation of the aortic arch characterized by the brachiocephalic trunk and left common carotid artery sharing the same origin.

4.2.1 Clinical data

Following the research protocol approved by the review board of the *Unidade Local de Saúde São José* and with the patient's written informed consent, each subject underwent a Computed Tomography Angiography (CTA) used to recreate patient-specific anatomy.

Moreover, a 4D flow Magnetic Resonance Imaging (MRI) was conducted to provide blood flow data, which was used to inform the inlet and outlet boundary conditions. A summary of patient-specific data regarding demographics, aortic diameters, valve type and heart function is presented in Table 4.1.

4.2.1.1 Computed tomography angiography

The CTA data acquisition of the thorax was performed on a revolution CT scanner (GE Healthcare, Milwaukee, WI, USA) and with the administration of iodinated contrast agent (Ultravist 370, Bayer, Leverkusen, Germany). The complete CTA dataset for each patient comprises 21 ECG-gated acquisitions, taken through the ECG R-R interval with a fixed time step, allowing the sampling of cardiac phases with a 5 % resolution. Each acquisition consisted of $512 \times 512 \times 292$ voxels, at a resolution of 0.63 mm $\times$ 0.63 mm $\times$ 0.63 mm. CTA images of the three subjects evidenced the presence of ATAA in different stages of progression, being that two of them had a maximum diameter (44.2 mm and 49.4 mm) below the clinical threshold for surgical intervention and the remaining had a diameter above this limit (63.3 mm).

4.2.1.2 4D flow magnetic resonance imaging

The 4D flow MRI acquisition was performed on a 3T scanner (Signa, GE Healthcare, Milwaukee, WI, USA) with no contrast medium. Imaging resolution (RL-AP-SI) was 2.0 mm $\times$ 2.0 mm $\times$ 2.4 mm and 20 instances of the cardiac cycle were captured. Velocity encoding was set to 1.9 m s^{-1}. Arterys software (San Francisco, CA, USA) was used for semi-automated eddy current correction and data analysis, allowing the extraction of flow rate time series in five different locations (sinotubular junction, brachiocephalic trunk, left common carotid artery, left subclavian artery and descending thoracic aorta). This data guided the prescription of patient-specific inlet boundary conditions and the calibration of three-element Windkessel models applied at the outlets. It is worth mentioning that (i) the measured flow did not respect the mass conservation law and (ii) the total cardiac output did not match the cardiac output measured by the disk method using Fast Imaging Employing Steady-state Acquisition (FIESTA) images of the heart. To overcome this issue, the inlet flow rate was scaled to match the cardiac output measured with FIESTA imaging

Table 4.1: Patient-Specific demographics, valve type, heart function and wall thickness.

Patient	**Age**	**Sex**	**Valve**	**MaxD** [mm]	**CardOut** [L min^{-1}]	**EjecFra** [%]	**Hrate** [bpm]	**Thick** [mm]
A	70	M	TAV	44.2	5.4	57.0	67.0	1.4
B	69	F	BAV	62.3	4.7	61.0	65.0	1.0
C	48	F	BAV	49.4	4.0	65.0	72.0	1.8

BAV = Bicuspid aortic valve, CardOut = Cardiac output, EjecFra = Ejection fraction, F = Biological female, Hrate = Heart rate, M = Biological male, MaxD = Maximum diameter, TAV = Tricuspid aortic valve.

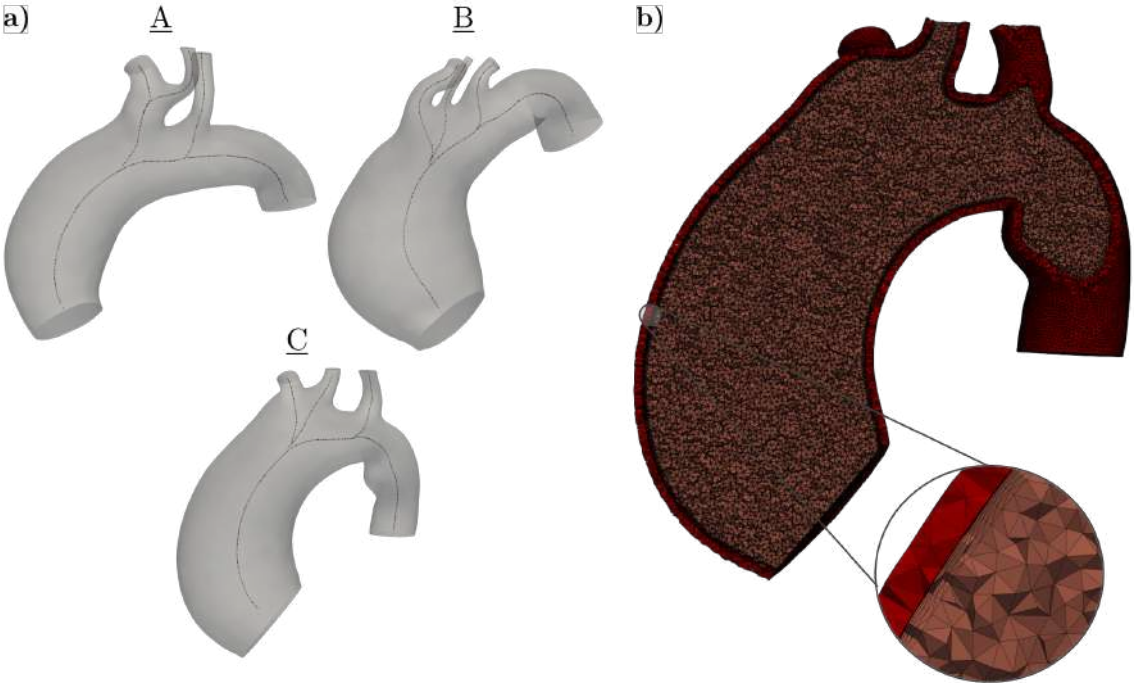

Figure 4.2: a) Final lumen virtualizations of patients A, B and C and b) representative finite element mesh of the fluid and solid domains used to perform FSI simulations of ATAA.

and then the outlet flows were scaled to respect mass conservation. Also, the inlet flow rate was interpolated using a cubic spline interpolation with a time resolution of 10^{-2} s.

4.2.2 Anatomy segmentation and mesh generation

The segmentation of patient-specific anatomic models was performed on open-source software 3D Slicer [212]. Two instances of the cardiac cycle, namely at 0 % and 30 %, were segmented. The former was used to perform the biomechanical simulation of ATAA, while the latter was used as a reference to calibrate aortic wall properties. After segmentation, the patient-specific anatomy of both domains was meshed within SimVascular [211].

4.2.2.1 Aneurysm virtualization

The virtualization of the lumen domain required a combination of segmentation techniques. Threshold segmentation was utilized to generate a rough approximation of the ATAA. This approximation was then used as input on a region growing algorithm that generated the final segmentation. Finally, the extremities of this segmentation were sliced to simplify the mesh generation process. The results of the segmentation process are presented in Fig. 4.2a. The aortic wall is around 1.0–2.5 mm thick which translates to 3–5 pixels. Although CTA spatial resolution is higher than other imaging modalities, it is still challenging to directly extract the solid domain from the CTA images. Hence, the solid domain was generated considering the lumen virtualization and a uniform thickness.

4.2.2.2 Meshing

The mesh elements of both domains were produced using the Tetgen Libraries tools embedded into SimVascular [211]. Initially, a surface and volumetric mesh with 4 boundary layers was generated in the fluid domain. Afterward, the mesh of the fluid domain at the fluid-solid interface was imported into the Blender software (https://www.blender.org/) where the solid domain was generated with a uniform thickness. This step allowed the attribution of different element sizes to the fluid and solid meshes, which is not possible using only SimVascular [52]. Lastly, the solid domain was imported into SimVascular and only a volumetric mesh was generated to ensure a nodal correspondence at the fluid-solid interface. In Fig. 4.2b an example of the generated mesh is presented.

The mesh sensitivity analysis was presented in our previous work [52] which revealed that the ideal finite element mesh was composed of about 1.1×10^6 and 1.6×10^5 elements in the fluid and solid domains, respectively. In this study, the same values were used as reference due to the similarity in geometries and boundary conditions.

4.2.3 Numerical modelling

4.2.3.1 Fluid domain

Blood, an incompressible solution of plasma and blood cells, exhibits distinctive rheological properties, namely shear-thinning viscosity and viscoelasticity. Despite this, the consensus for large calibre arteries is to model blood as a Newtonian fluid [56, 79, 127, 194]. Also, it is widely accepted to model the blood flow inside the aorta as laminar [18, 54, 155, 181]. The Navier-Stokes and continuity are the governing equations of the fluid domain dynamics, which written in the Arbitrary Lagrangian-Eulerian (ALE) formulation are as follows:

$$\begin{matrix} \rho_\mathrm{f} \left[\hat{\partial}_t \boldsymbol{v} + (\boldsymbol{v} - \boldsymbol{w}) \cdot \nabla \boldsymbol{v} \right] - \nabla \cdot \boldsymbol{\sigma}_\mathrm{f} = 0 \\ \nabla \cdot \boldsymbol{v} = 0 \end{matrix}, \text{ in } \Omega_\mathrm{f} \tag{4.1}$$

The ALE formulation of the fluid domain, Ω_f, takes into account the wall movement via grid velocity, $\boldsymbol{w}$, and the ALE time derivative, $\hat{\partial}_t$, which resorts to the generalized-α scheme applied to FSI models proposed by Bazilevs et al. [213] to solve time integration. The Cauchy stress tensor, $\boldsymbol{\sigma}_\mathrm{f}$, is dependent on the fluid velocity, $\boldsymbol{v}$, fluid pressure, p, and fluid viscosity, μ and given as $\boldsymbol{\sigma}_\mathrm{f} = \mu(\nabla \boldsymbol{v} + \nabla \boldsymbol{v}^\mathrm{T}) - p\boldsymbol{I}$. The operator ∇ represents the gradient operator and ρ_f is blood density. Fluid viscosity and density are the two only necessary parameters to completely describe the behaviour of a Newtonian fluid and the values used in this work are presented in Table 4.2.

As initial conditions of the fluid domain, the PT and PTCAL FSI simulations considered an initial pressure and velocity fields which were obtained from CFD analysis. In contrast, for the ZPG simulations, zero pressure and velocity fields were employed.

Table 4.2: Mechanical properties of the fluid and solid domains.

Property	Symbol	Units	Value	References
Blood density	ρ_f	$kg\,m^{-3}$	1060	[53, 173, 180]
Viscosity	μ	Pa s	4×10^{-3}	[179, 180, 182]
Aortic wall density	ρ_s	$kg\,m^{-3}$	1120	[153, 201]
Poisson ratio	ν_s	—	49×10^{-2}	[79, 189]

4.2.3.2 Solid Domain

During the cardiac cycle the ATAA undergoes significant nonlinear deformation. For each material particle, the information regarding the deformation in the vicinity of that particle is stored in the deformation gradient, $\boldsymbol{F} = \boldsymbol{I} + \partial \boldsymbol{u}/\partial \boldsymbol{X}$, which is a function of the displacement field, $\boldsymbol{u}$, and time, t. The stress state of the same material particle, when "pulled back" to the reference configuration, $\boldsymbol{X}$, is defined in terms of the second Piola-Kirchhoff stress tensor, $\boldsymbol{S}$. The Cauchy momentum equation, which serves as the governing balance equation for the solid domain and represents the application of Newton's second law to continuum mechanics, can be expressed with respect to the reference configuration of the solid domain, Ω_s^0, as follows:

$$\rho_s \frac{\partial^2 \boldsymbol{u}}{\partial t^2} + \nabla \cdot [\boldsymbol{F}\boldsymbol{S}] = 0, \text{ in } \Omega_s^0 \tag{4.2}$$

The aortic wall also exhibits distinctive mechanical behaviour similar to an anisotropic, hyperelastic and viscoelastic material. These attributes stem from its intricate microstructure, composed of a variety of constituents such as elastin, collagen and smooth muscle cells [128]. In this work, the ATAA wall was modelled as a monolayer, isotropic, incompressible and Neo-Hookean material [214], which holds the following second Piola-Kirchhoff stress tensor:

$$\boldsymbol{S}_{NH} = \mu^s \boldsymbol{J}^{-\frac{2}{3}} \left(\boldsymbol{I} - \frac{1}{3} \operatorname{tr} \boldsymbol{C}\boldsymbol{C}^{-1} \right) + \frac{1}{2}\kappa_s \left(\boldsymbol{J}^2 - 1 \right) \boldsymbol{C}^{-1} \tag{4.3}$$

where is the identity tensor; $J = \det(\boldsymbol{F})$ denotes the Jacobian; $\boldsymbol{C} = \boldsymbol{F}^T\boldsymbol{F}$ is the right Cauchy-Green deformation and $\operatorname{tr} \boldsymbol{C}$ denotes the trace of the tensor $\boldsymbol{C}$; μ^s and κ_s are the second Lamé parameter and bulk modulus, respectively, which are defined using Young's modulus, E_s, and Poisson ratio, ν_s:

$$\mu^s = \frac{E_s}{2\,(1+\nu_s)} \tag{4.4}$$

$$\kappa_s = \frac{E_s}{3\,(1-2\nu_s)} \tag{4.5}$$

The values chosen for the solid domain density and Poisson ratio are presented in Table 4.2 and were obtained from the available literature. To find a patient-specific estimation of the Young's modulus, a simple iterative methodology was employed. The volume

of the segmentation at 30 % of the cardiac cycle was the target value for this calibration process. Computational Solid Mechanics (CSM) simulations considering different Young's modulus and a pressure boundary condition equivalent to the hemodynamic loads at the same time instance, were performed until the estimated volume matched the reference value within a margin of error below 5 %. The final values of the Young's modulus were 1.93 MPa, 5.18 MPa and 0.95 MPa for patients A, B and C, respectively.

4.2.3.3 Blood-aortic wall interface

The interaction between the blood and the aortic wall occurs at the interface, Γ, between the domains, in which, the hemodynamic loads are transferred to the solid domain and the displacement field of the aortic wall updates the fluid domain mesh. SimVascular resorts to a monolithic approach to solve the FSI problem. During mesh generation, at the fluid-solid interface, a nodal correspondence between both domains was ensured. Hence, fulfilling kinematic and dynamic boundary conditions are given by:

$$\begin{aligned} \boldsymbol{w} &= \frac{\partial \boldsymbol{u}}{\partial t} \\ \boldsymbol{\sigma}_{\mathrm{f}}\hat{\boldsymbol{n}}_{\mathrm{f}} + \boldsymbol{\sigma}_{\mathrm{s}}\hat{\boldsymbol{n}}_{\mathrm{s}} &= 0 \end{aligned} \quad , \text{ in } \Gamma \tag{4.6}$$

where $\boldsymbol{\sigma}_{\mathrm{s}}$ is the Cauchy stress tensor and $\hat{\boldsymbol{n}}_{\mathrm{s}}$ is the unit normal to the surface, both in the solid domain and σ_{f}, $\hat{\boldsymbol{n}}_{\mathrm{f}}$ are the counterparts for the fluid domain.

4.2.4 Boundary conditions

Three different boundary conditions were used to develop the FSI model: (i) patient-specific inlet flow rate at the sinotubular junction; (ii) three-element Windkessel models at the outlets (descending thoracic aorta, brachiocephalic trunk, left common carotid and left subclavian) and (iii) zero displacements in the axial direction at the solid domain extremities while allowing movement in the radial direction. These boundary conditions are presented in Fig. 4.3.

At the fluid domain inlet, a Dirichlet time-dependent boundary condition was prescribed, by assigning to each node a specific velocity vector. The velocity vector was calculated using the prescribed patient-specific flow rate, obtained via MRI, and assuming a parabolic velocity profile.

The outlets were coupled with zero-dimensional three-element Windkessel models, also known as RCR models, which are electric analogs of the blood flow. These models estimate the outlet pressure by accounting for the impedance of the downstream vasculatures [215]. The patient-specific coefficients for each three-element Windkessel model are reported in Table 4.3. These were calibrated, using reduced order models implemented in SimVascular, to fit a diastolic systolic pressure variation of 80-120 mmHg.

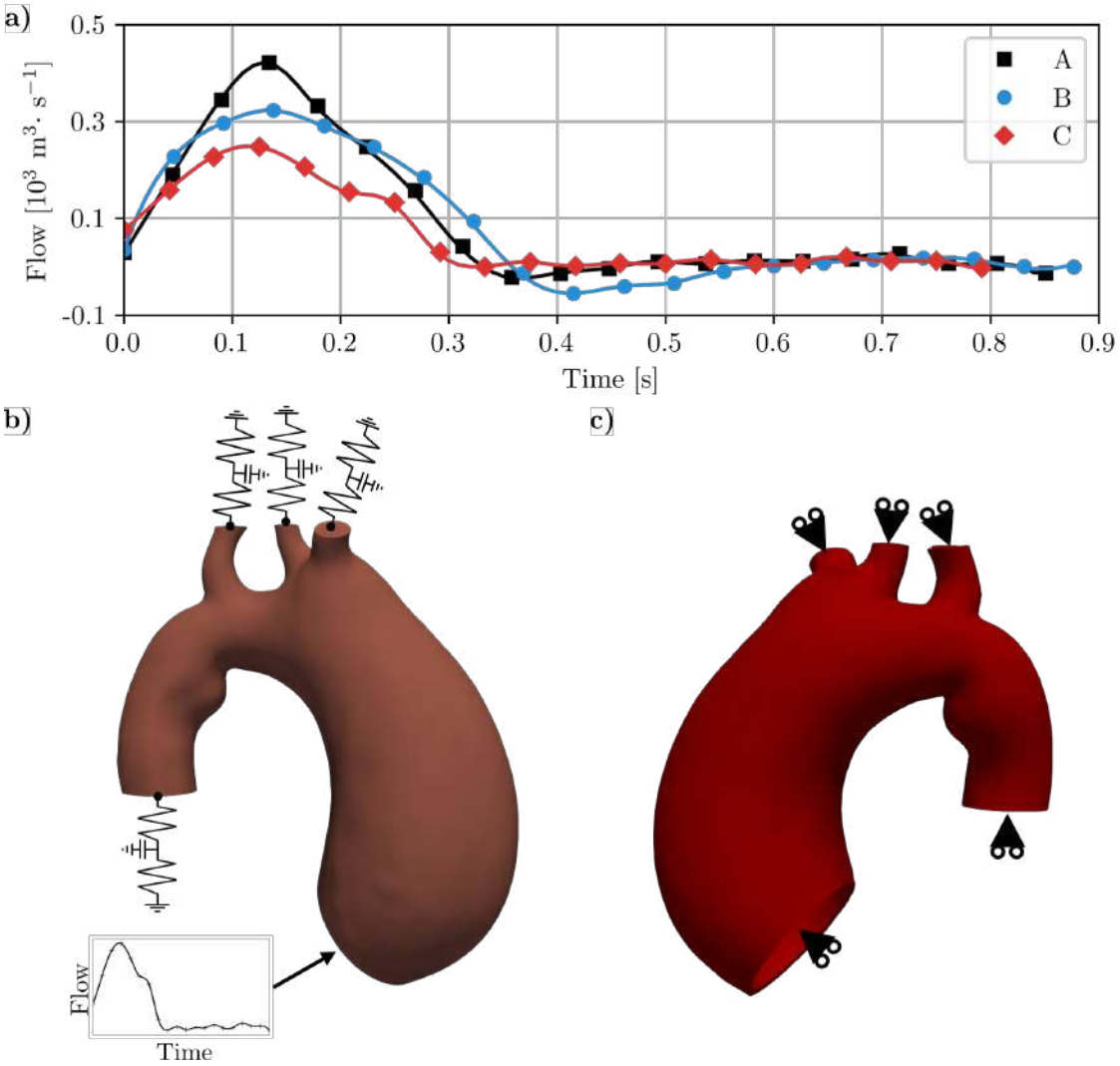

Figure 4.3: Boundary conditions of the fluid and solid domains: a) flow rate applied at the inlet (sinotubular junction) for patients A, B and C; b) three-element Windkessel models at the outlets and c) domain extremities are fixed in the normal direction to the plane.

4.3 Tissue prestressing methods

The ATAA is constantly loaded during the cardiac cycle by blood pressure and viscous forces. Hence, the image configuration available in CTA data already has a non-zero stress state. The fact that the image configuration does not match the reference configuration negatively impacts the accuracy of the numerical results, mainly due to the nonlinear deformation of the aortic wall. In this work, the ZPG and PT methodologies were implemented, as well as, a novel method that couples the PT approach and a regional mapping of calibrated material properties. This method updates the local Young's modulus of the model to account for the deformation between the reference and image configurations.

Table 4.3: Patient-specific three-element Windkessel models parameters.

Patients	**A**			**B**			**C**		
Outlet	R_s	C	R_p	R_s	C	R_p	R_s	C	R_p
Descending aorta	6	7500	160	13	6500	180	15	4000	300
Brachiocephalic trunk	50	1100	1130	50	1100	1300	50	700	850
Left common carotid	110	800	2800	110	900	2200	90	600	2000
Left subclavian	120	1800	2575	120	1500	2400	70	1000	1700

R_s = Resistance of larger calibre arteries in MPa s m^{-3}, C = Artery compliance in m^3 Pa^{-1}, R_p = Resistance of smaller arteries and arterioles in MPa s m^{-3}.

4.3.1 Reverse displacement algorithm

A wide range of methods based on the ZPG approach are available in the literature. In this work, the reverse displacement algorithm proposed by Raghavan, Ma, and Fillinger [130] was implemented (Fig. 4.4a). The main principle is to estimate a parameter, k, that is related to the pre-deformation between the reference and image configurations. This parameter is calculated by solving a minimisation problem of a distance score which quantifies the differences between a deformed candidate reference configuration, yielded from applying the diastolic pressure field on a candidate reference configuration, and the image configuration. The minimisation problem was solved using the Nelder–Mead method which is often applied to nonlinear problems which the derivatives may not be known. In summary, the numerical implementation of this algorithm requires the following four main steps [130] (Fig. 4.4a):

1. Estimate the diastolic hemodynamic loads, P_{dia}, by performing a Computational Fluid Dynamics (CFD) analysis on the image configuration (0 % of the cardiac cycle), $\boldsymbol{X}_{im}$, using the boundary conditions described in Subsection 4.2.4.

2. Calculate the reference displacement field, $\mathbf{U}$, estimated by finding the deformed image configuration, $\boldsymbol{x}_{im}$, which is the result of applying P_{dia} on $\boldsymbol{X}_{im}$.

3. Perform CSM analysis in order to find the candidate reference configuration, $\boldsymbol{X}_{0k}$, that minimizes the differences between $\boldsymbol{X}_{im}$ and the deformed candidate configuration, $\boldsymbol{x}_{0k}$, yielded by applying P_{dia} on $\boldsymbol{X}_{0k}$. To find the solution, the following steps are repeated until the distance score, A^k, is below a user-defined tolerance, ε:

   (a) Create $\boldsymbol{X}_{0k}$ by applying $\mathbf{U}$ reversed and scaled by a scalar quantity, k (ranging from 0.7-1.2), on $\boldsymbol{X}_{im}$;

   (b) Consider $\boldsymbol{X}_{0k}$ stress-free and apply P_{dia} in order to estimate the deformed candidate configuration, $\boldsymbol{x}_{0k}$;

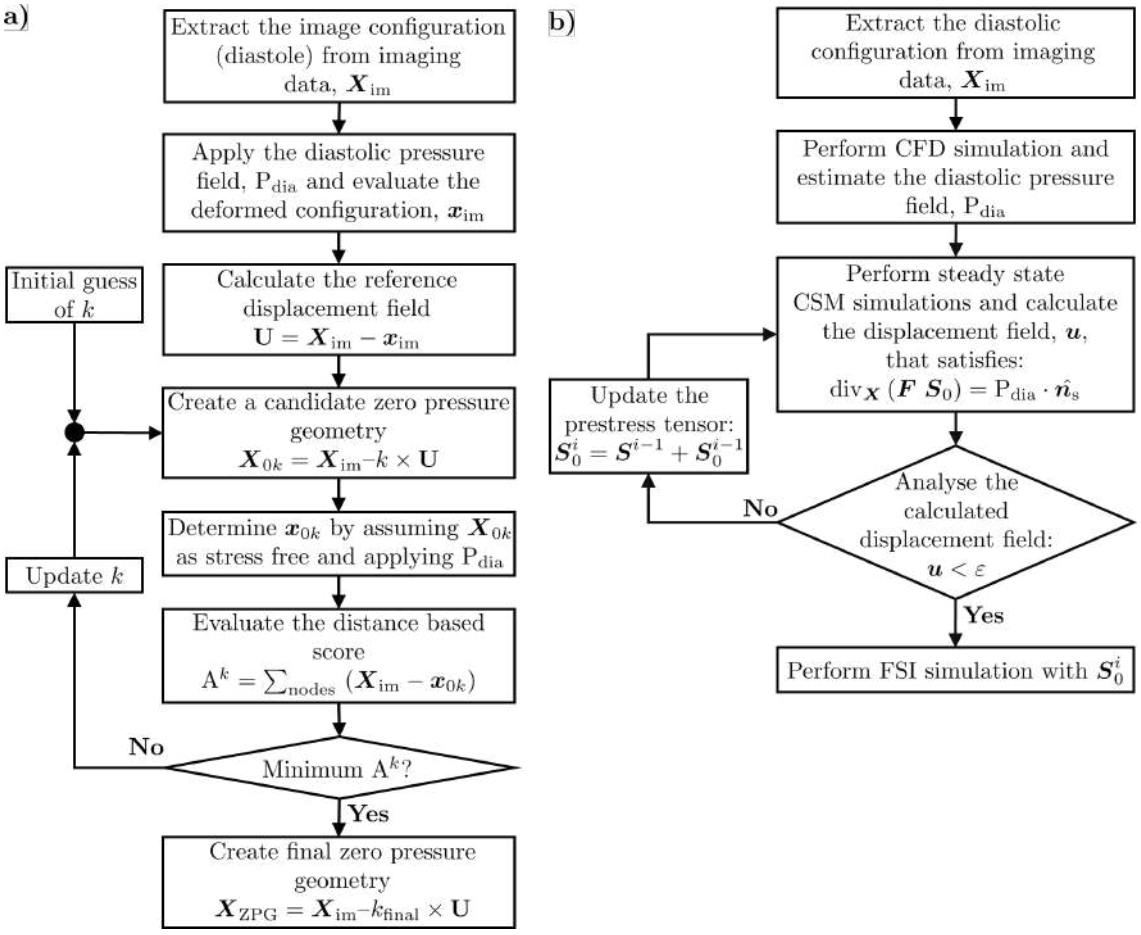

Figure 4.4: Schematic of the numerical implementation of a) the reverse displacement algorithm and b) the PT approach.

(c) Estimate A^k and update k until convergence is achieved.

4. Perform FSI analysis using the optimum candidate reference configuration, $\boldsymbol{X}_{\text{ZPG}}$.

4.3.2 Prestress tensor

The PT methodology (Fig. 4.4b) was proposed by Hsu and Bazilevs [129] and accounts for the diastolic stress state by suggesting a slight modification to the solid domain formulation, proposing to incorporate the PT, $\boldsymbol{S}_0$, in the image domain, Ω_{im} using the additive decomposition of the second Piola-Kirchhoff stress tensor:

$$\rho_{\text{s}} \frac{\partial^2 \boldsymbol{u}}{\partial t^2} + \nabla \cdot [\boldsymbol{F}\,(\boldsymbol{S} + \boldsymbol{S}_0)] = 0, \text{ in } \Omega_{\text{im}} \tag{4.7}$$

This tensor is calibrated in order to balance the diastolic hemodynamic loads applied at the fluid-solid interface, in other words, $\boldsymbol{S}_0$ is calculated as the stress state in the image configuration that yields a null displacement field when P_{dia} is applied:

$$\nabla \cdot [\boldsymbol{F}\ \boldsymbol{S}_0] = \text{P}_{\text{dia}} \cdot \hat{\boldsymbol{n}}_{\text{s}} \tag{4.8}$$

Numerically, the implementation of the methodology proposed by Hsu and Bazilevs [129] is a fairly straightforward process consisting of the following steps:

1. Estimate P_{dia} at the image configuration time instance through the performance of a rigid wall analysis on the fluid domain considering the boundary conditions presented above (Subsection 4.2.4).

2. Perform the prestress analysis using P_{dia}. As Eq. 4.8 may hold an infinite number of solutions, the following algorithm is executed to estimate one particular solution:

   (a) Define $\boldsymbol{S}_0 = \boldsymbol{S}_0^i$ and $\boldsymbol{u} = 0$ which consequently holds $\boldsymbol{F} = \boldsymbol{I}$ and $\boldsymbol{S} = 0$;

   (b) Run a steady CSM simulation with P_{dia} and estimate $\boldsymbol{u}$ which is a solution of Eq. 4.7;

   (c) Update $\boldsymbol{S}_0^i$ as the sum of the previously used PT, $\boldsymbol{S}_0^{i-1}$, and the estimated second Piola-Kirchhoff stress tensor, $\boldsymbol{S}^{i-1}$, on the previous iteration. This step, as well as all the above, are performed until convergence is achieved, i.e., $\boldsymbol{u} \approx 0$.

3. Perform FSI analysis with augmented second Piola-Kirchhoff tensor and considering $\boldsymbol{S}_0 = \boldsymbol{S}_0^i$.

4.3.3 Prestress tensor with calibrated material properties

In our preliminary analysis, we found that models employing the PT method exhibit a significantly stiffer structural response compared to those using ZPG algorithms. This phenomenon is illustrated in Fig. 4.5. It occurs because ZPG algorithms account for the pre-deformation between the reference and image configurations, whereas the PT approach does not. Considering a representative stress-strain curve for a Neo-Hookean material, which exhibits logarithmic behaviour, the tangential Young's modulus decreases with increasing stretch. Consequently, the pre-deformation of the ATAA wall leads to a reduced tangential Young's modulus at the beginning of the cardiac cycle. Conversely, using the PT approach, the diastolic intramural stress state can be interpreted as residual stresses, with no deformation associated with it. Hence, the tangential Young's modulus at the beginning of the cardiac cycle is at its maximum possible value, which is higher than that obtained using ZPG algorithms, resulting in a stiffer structural response.

The PTCAL method was designed to improve this agreement by suggesting that, after employing the PT algorithm, a regional mapping of calibrated material properties should also be utilized when performing structural analysis of the ATAA wall. The hypothesis underlying this methodology is that a specific set of material properties should be attributed to each element of the solid domain mesh, reflecting the specific stress-strain state of the element at the beginning of the cardiac cycle. However, SimVascular limits the maximum number of sets of material properties to 32. Given this constraint, it was decided to define a number, j, of subdomains where material properties did not vary

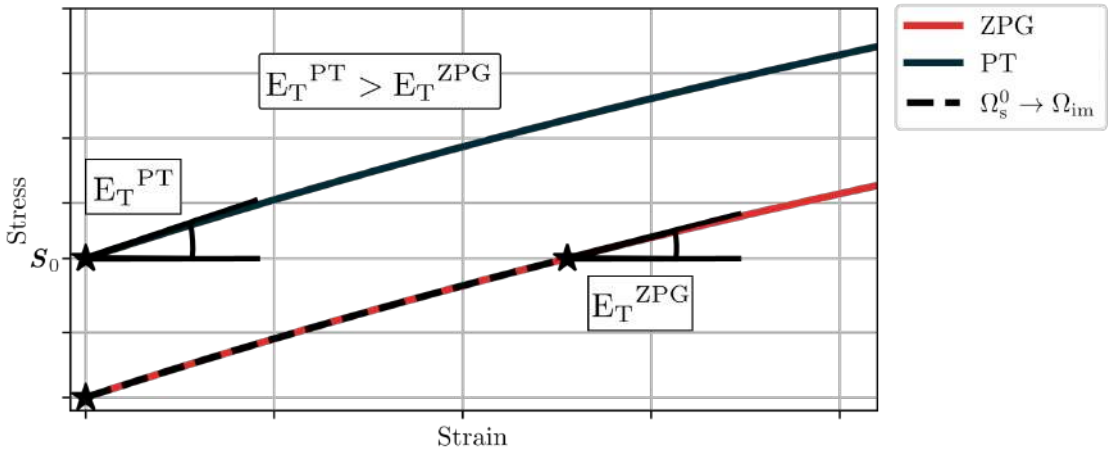

Figure 4.5: Representative stress-strain curves of a Neo-Hookean material using the ZPG and the PT approaches.

significantly. For this study, 10 subdomains were considered. Additionally, since the ATAA wall is modelled as a Neo-Hookean material, the Young's modulus was the only material property requiring calibration.

The implementation of the PTCAL methodology involves two main tasks: (i) dividing the ATAA wall mesh into subdomains (Fig. 4.6a) and (ii) assigning each subdomain a Young's modulus representative of the stress-strain state at the beginning of the cardiac cycle (Fig. 4.6b). The following steps were performed to complete these tasks:

1. Define the 10 subdomains, Ω_s^j.

   (a) Use the previously estimated $\boldsymbol{S}_0$ to calculate the Principal Stresses average, $\overline{\sigma_P}$, of each element of the solid domain;

   (b) Divide the range of $\overline{\sigma_P}$ into 10 equally spaced intervals. Each of the intervals defines a subdomain, Ω_s^j. These subdomains follow that $\bigcup_{j=1}^{10} \Omega_s^j = \Omega_s^0$ and $\bigcap_{j=1}^{10} \Omega_s^j = \varnothing$. Additionally, they are characterized by the medium value of Principal Stresses average, $\overline{\sigma_P}^j$.

2. Estimate the new Young's modulus [216, 217], $E_{CAL}{}^j$, for each subdomain.

   (a) Virtualize an uniaxial tensile test on a sample of ATAA tissue (considering the Young's modulus used for the PT methodology) to estimate the relation between the force, $\vec{F}$, and the stretch, λ, relative to the deformation between the image and reference configurations;

   (b) Calculate the Kirchhoff stress, σ', and Green-St. Venant strain, ε', as follows:

$$\sigma' = \frac{F}{A_0 \cdot \lambda} \quad \varepsilon' = \frac{\lambda^2 - 1}{2} \tag{4.9}$$

   where A_0 is the initial cross-sectional area of the sample;

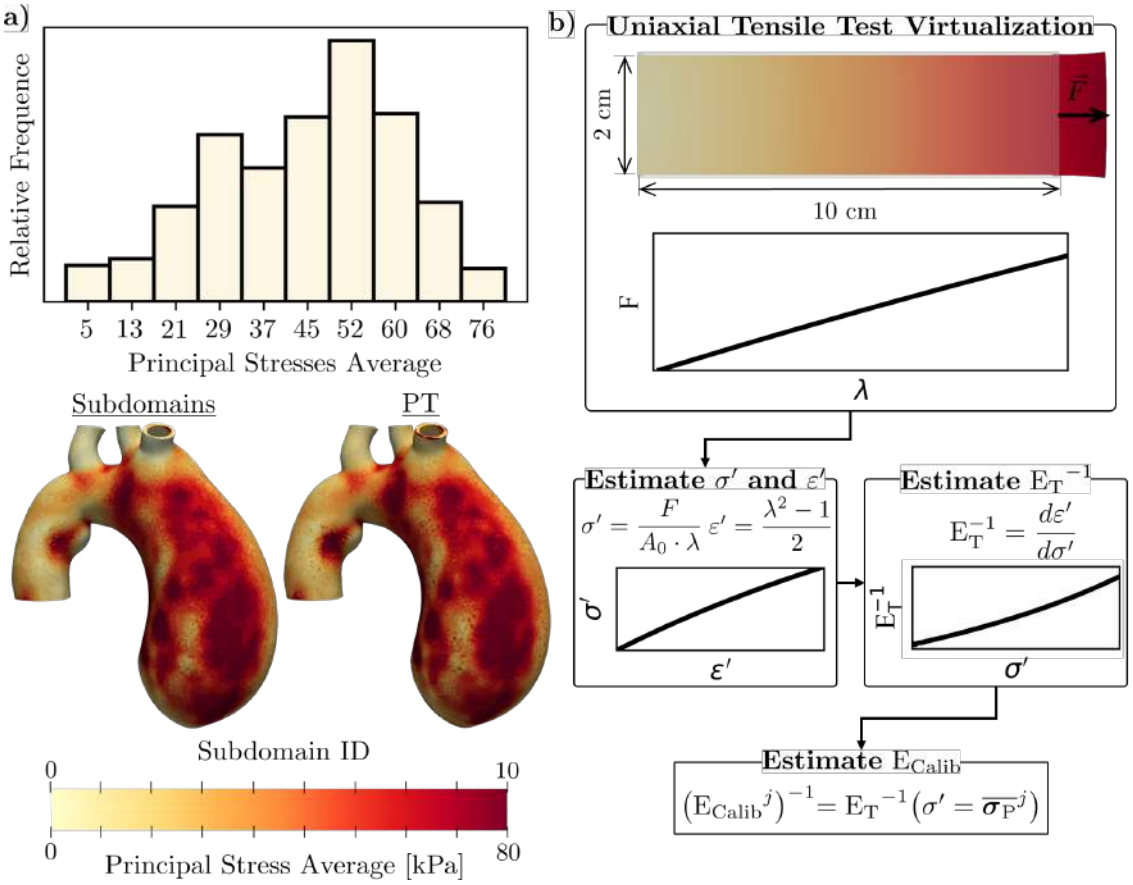

Figure 4.6: Schematic representation of PTCAL methodology numerical implementation: a) creation of the subdomains and b) estimation of the calibrated Young's modulus.

(c) Estimate the inverse of the tangential Young's modulus, $E_T{}^{-1}$, as the derivative of ε' with respect to σ';

(d) Attribute the new E_{CAL} to each subdomain as the estimated tangent Young's modulus correspondent to $\left(E_{CAL}{}^{j}\right)^{-1} = E_T{}^{-1}\left(\sigma' = \overline{\sigma_P}^{j}\right)$.

4.4 Impact of different tissue prestressing methods

The impact of different tissue prestressing methods on the biomechanical characterization of ATAA using FSI models was measured in this study. Regarding the hemodynamics, the pressure field and WSS based metrics were analysed due to their positive correlation with the risk of acute complications [96, 218], such as rupture and dissection. The nodal pressure time series of PT and PTCAL models were compared with ZPG using the pairwise Pearson's correlation coefficient, R, which ranges from -1 to 1 for negative and positive correlations, respectively. Regarding the estimated WSS, the impact was quantified in terms of the Time-Averaged Wall Shear Stress (TAWSS) (measures the local average magnitude of WSS):

$$\text{TAWSS} = \frac{1}{T}\int_0^T |\text{WSS}|\ \text{dt} \tag{4.10}$$

together with Oscillatory Shear Index (OSI) (quantifies the directional changes of WSS during the cardiac cycle):

$$\text{OSI} = \frac{1}{2}\left(1 - \frac{\left|\int_0^T \text{WSS}\ \text{dt}\right|}{\int_0^T |\ \text{WSS}|\text{dt}}\right) \tag{4.11}$$

and Relative Residence Time (RRT) (aims to quantify the time blood is near the wall):

$$\text{RRT} = \left[\text{TAWSS}\left(1 - 2 \cdot \text{OSI}\right)\right]^{-1} \tag{4.12}$$

To investigate the impact of the prestressing methods on the estimated structural response, both the maximum principal strain and maximum principal stress were analysed as these are also relevant metrics for the risk stratification of acute complications.

Another relevant aspect regarding the application of these methodologies is the cycle-to-cycle convergence which was evaluated by analysing the number of required iterations until a periodic steady-state is achieved (Eq. 4.13). The periodic steady-state was considered to be obtained when the relative instantaneous difference of estimated pressure in consequent cycles was below an user-defined tolerance, $\varepsilon = 2.5$ %.

$$\frac{|p(t) - p(t-T)|}{p(t-T)} < \varepsilon \tag{4.13}$$

Where t is a time instant and T is the period of the cardiac cycle.

4.4.1 Pressure field

The violin plots of the Pearson's correlation coefficient regarding the comparison of nodal pressure time series between the ZPG approach, considered as the reference values, the PT and PTCAL models are presented in Fig. 4.7. Across all patients, the PT based approaches exhibited a strong correspondence with the estimated pressure field by the ZPG algorithm. This is evidenced by the fact that the average values of R were greater than 0.99 for all patients and models. It is also noticeable that the PTCAL methodology slightly outperformed its counterpart regarding the estimation of the pressure field.

4.4.2 Wall shear stress

The violin plots of WSS based metrics of each patient, presented in Fig. 4.8, revealed that all models produced similar distributions and average behaviours which is indicative of a good agreement between the ZPG, PT and PTCAL models. However, by analysing the scatter plots presented in Fig. 4.9, only the TAWSS produced a good agreement between

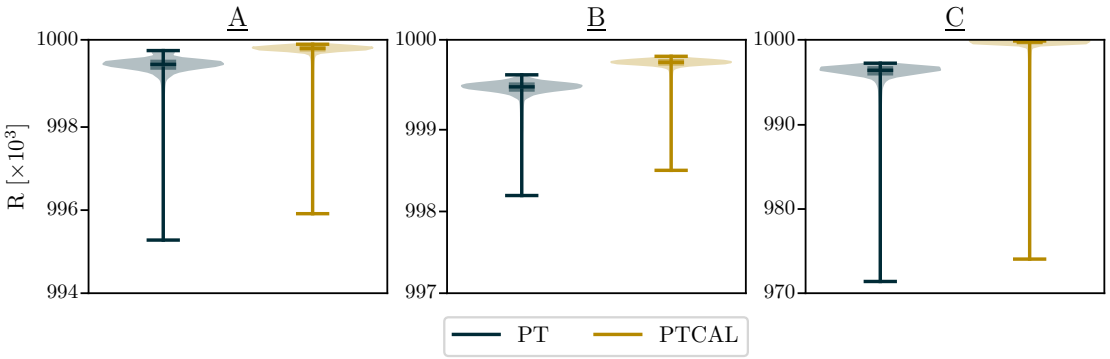

Figure 4.7: Impact of different tissue prestressing methods on the nodal pressure time series in the ATAA: violin plots of the Pearson's correlation coefficient, R, between the ZPG model (reference) and the PT and PTCAL models.

the different tissue prestressing approaches (correlation coefficient, R^2,ranging from 0.82–0.98), in particular for patients B and C. Regarding the OSI (correlation coefficient R^2 ranging from 0.59–0.84) and RRT (correlation coefficient R^2 ranging from 0.31–0.47) the scatter plots evidence a greater variation between the approaches.

4.4.3 Maximum principal stress and strain

The impact of different tissue prestressing methods on the estimated probability density function of the maximum principal strain and stress in the ATAA wall is presented in Fig. 4.10. Contrary to the hemodynamic indices, only patient B presented similar distributions of maximum principal strain and stress across all methodologies. For the remaining patients, significant differences were found when comparing the ZPG approach results with the PT and PTCAL models. Additionally, although the variation is slight in the maximum principal stress distribution of patient A, significantly distinct distributions were observed in the maximum principal strain and stress of the PT and PTCAL models. The scatter plots of Fig. 4.11 confirm this analysis. Patient B presented the higher correlation coefficient R^2, with values ranging from 0.92–0.97. Patient A also presented a good R^2 (ranging from 0.88–0.96). Patient C, however, presented the lowest R^2 (ranging from 0.74–0.88) and the biggest difference between the PT and PTCAL approaches.

4.4.4 Cycle-to-cycle convergence

The evolution of the average pressure and the periodic state criterium in three distinct orthogonal slices located along the computational domain is presented in Fig. 4.12. These results show that both PT and PTCAL required an equivalent amount of iterations to achieve a periodic state. Additionally, it was also evidenced that these two approaches outperformed the ZPG methodology in terms of cycle-to-cycle convergence taking around 60 % less iterations to achieve cycle-to-cycle convergence.

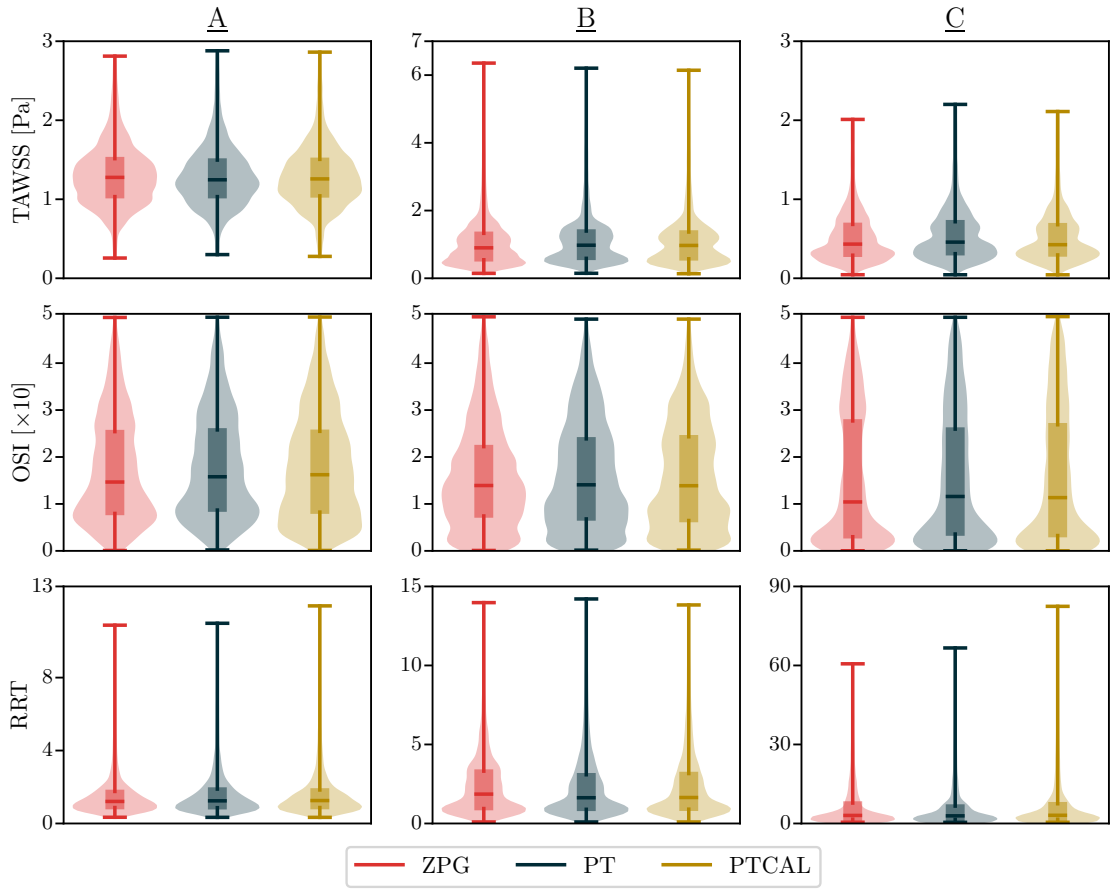

Figure 4.8: Impact of different tissue prestressing methods on the estimated WSS in the ATAA: violin plots of TAWSS, OSI and RRT.

4.5 Discussion regarding the use of tissue prestressing methods

The characterization of the reference configuration is a fundamental step to effectively perform numerical analysis of structures. This poses a concrete problem in modelling the mechanical behaviour of the ATAA wall, as this configuration is not available from *in vivo* imaging data. Although several approaches have been proposed in the literature to surpass this issue, the analysis of the impact of different tissue prestressing algorithms on the numerical results of FSI simulations has not been explored. In this work, three distinct methodologies were employed and compared to assess their impact on the estimated blood pressure, WSS and wall mechanics in ATAA.

The ZPG approach is the most commonly used methodology to estimate the reference configuration and is considered the gold-standard as it provides a complete description of the stress-strain state of the aortic wall at diastole. Nonetheless, this approach is computationally expensive and complex to implement. In this context, the PT emerges as a more straightforward and numerically efficient method. The results of this study revealed that the PT models produced similar results to the ZPG models in terms of blood pressure and the magnitude of WSS. However, the results regarding the direction of the WSS

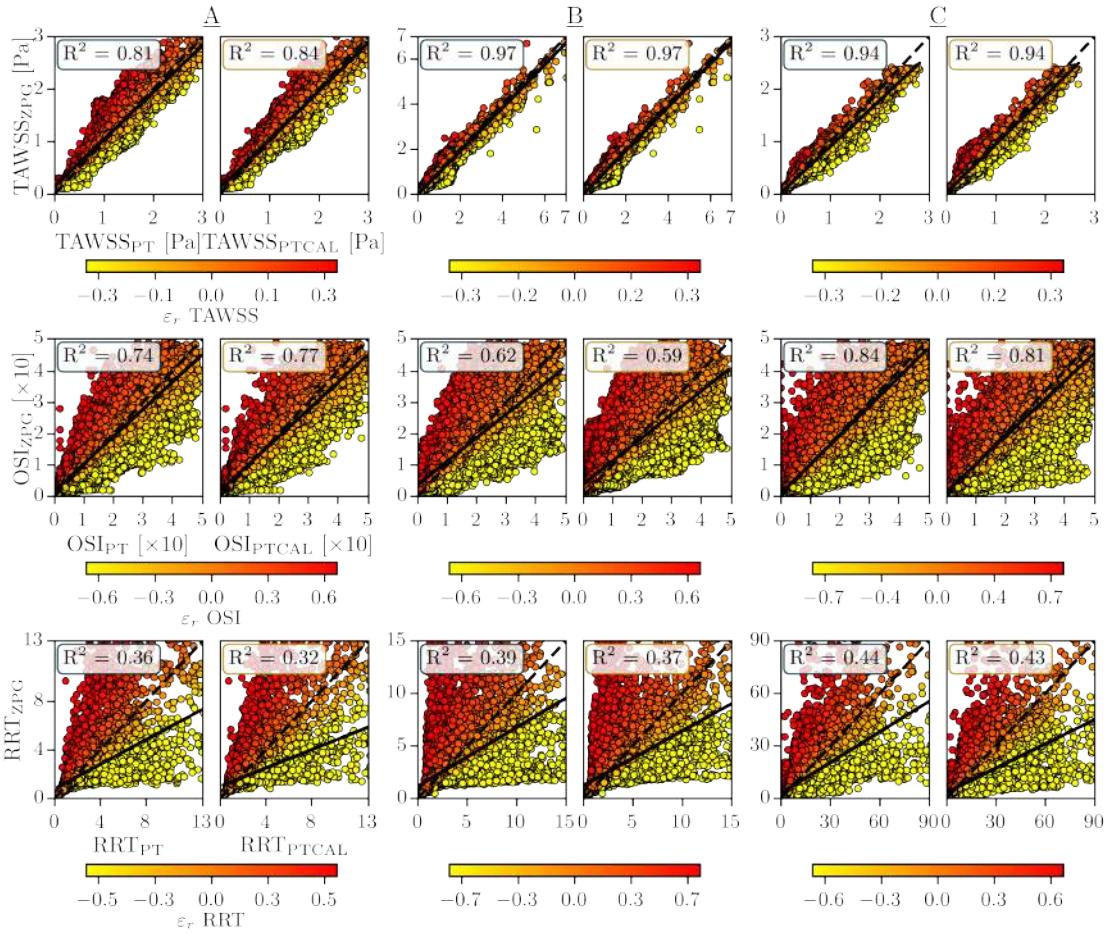

Figure 4.9: Quantification of the nodal variation between the ZPG model and the PT and PTCAL models of the estimated TAWSS, OSI and RRT, quantified by the nodal relative error, ε_r.

were significantly different, evidenced by the smaller correlation coefficients calculated for the OSI and RRT parameters. The estimated structural indices were also significant different as the PT models presented a stiffer mechanical response. Furthermore, the results evidenced that the difference in the estimated wall mechanics by the PT and ZPG grows with increased ATAA compliance.

The PTCAL methodology was developed to surpass this limitation regarding the simulation of ATAA wall mechanics. The regional mapping of calibrated material properties aimed to improve the characterization of the stress-strain state at the diastole in order to provide an improved agreement with the ZPG models. The PTCAL models produced results with equivalent degree of accuracy when compared to PT regarding blood pressure and WSS. However, it outperformed the PT models in the estimation of structural indices, presenting a closer agreement with the ZPG models. This aspects is particularly evident for patient C which presented the lowest stiffness among the studied patients, indicating that the use of the PTCAL methodology increases in relevance when the ATAA compliance is higher.

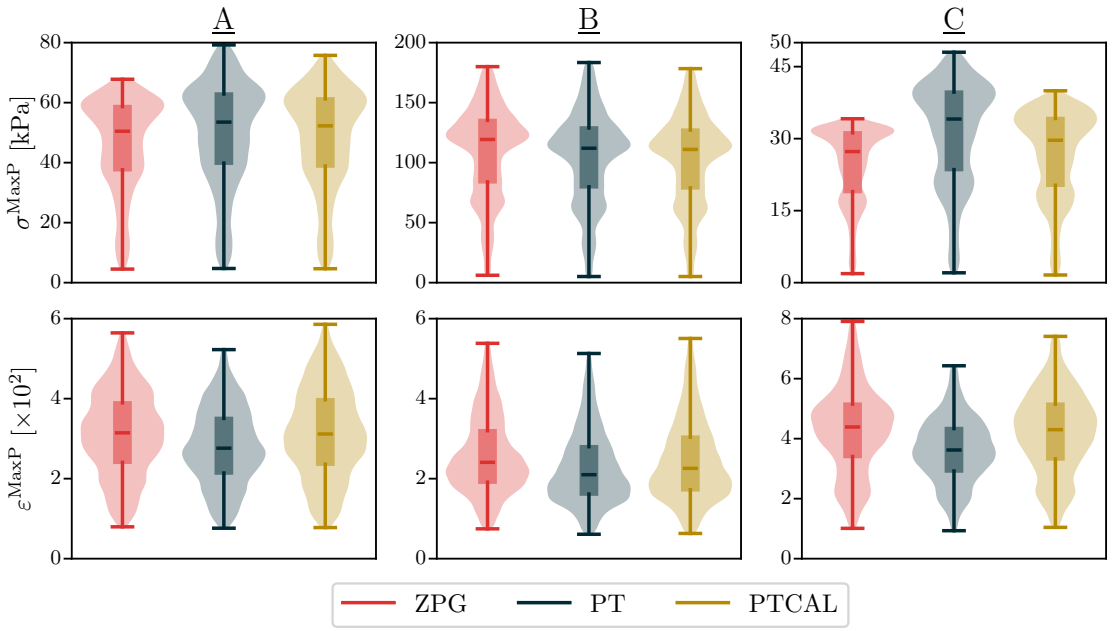

Figure 4.10: Impact of different tissue prestressing methodologies on the ATAA wall mechanics: violin plots of the maximum principal strain, ε^{MaxP}, and stress, σ^{MaxP}.

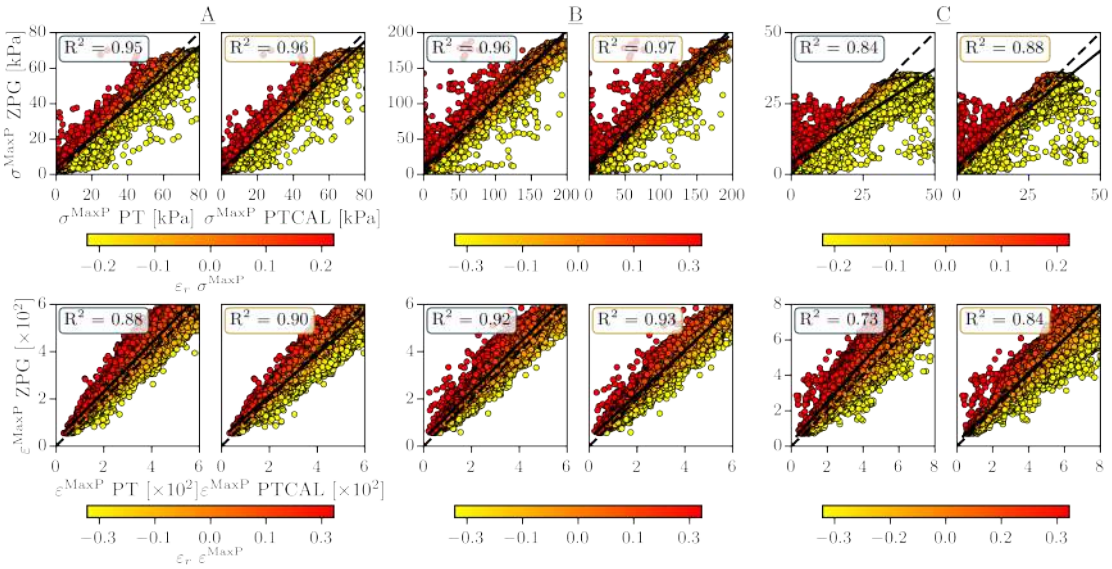

Figure 4.11: Nodal variation between the ZPG model and the PT and PTCAL models of the estimated maximum principal strain, ε^{MaxP}, and stress, σ^{MaxP}, quantified by the nodal relative error, ε_r.

One more relevant aspect when aiming towards the introduction of numerical models into clinical practices is the reporting time which can be directly influenced by the amount of iterations required to achieve a periodic steady-state, i.e, cycle-to-cycle convergence. In this matter both the PT and PTCAL models outperformed the ZPG approach as they required around 60 % less iterations to achieve the periodic state.

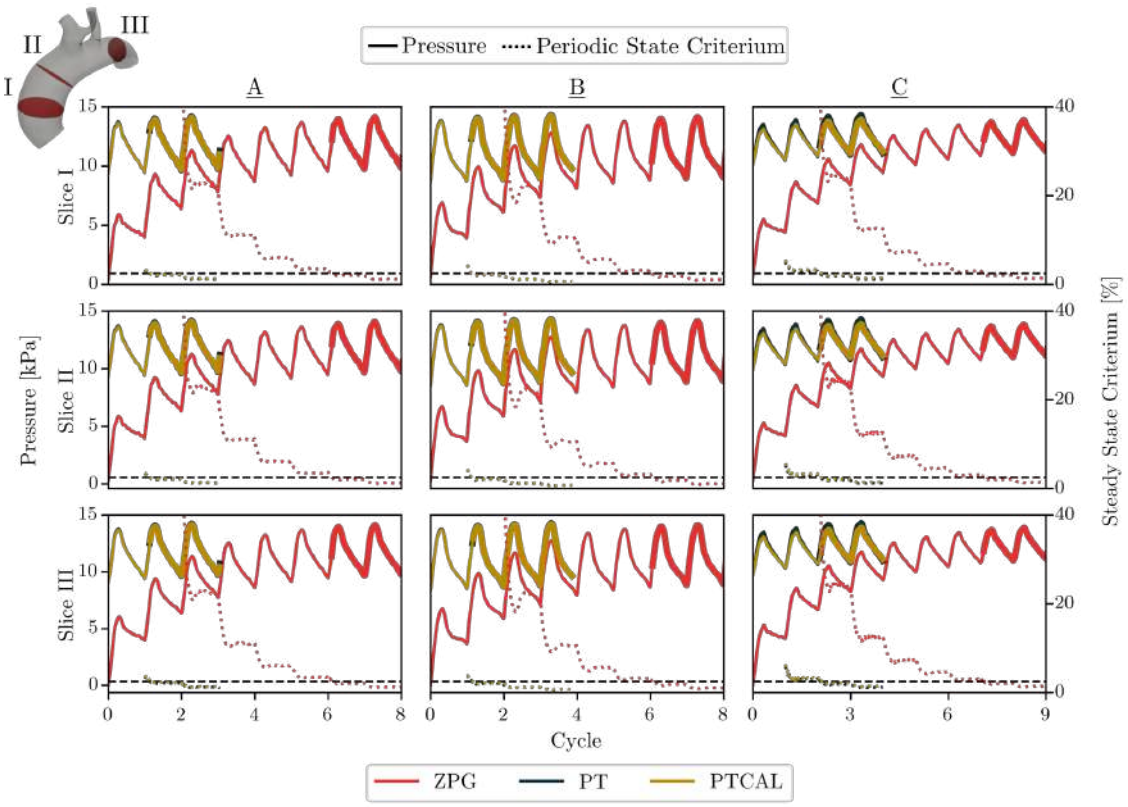

Figure 4.12: Impact of different tissue prestressing methods on the cycle-to-cycle convergence: time series of the average pressure and periodic state criterium in three orthogonal slices.

A relevant limitation of the PT and PTCAL methodologies is the range of application. Although these methods have advantages in terms of computational cost and numerical implementation, they become inadequate for recreating the biomechanical behaviour of ATAA at supraphysiological or infraphysiological pressure conditions that may occur during intense exercise, for instance. The non uniqueness of the solution found by the PT approach also represents a limitation of this work and will be addressed in future work.

4.6 Main remarks

In this chapter the impact of using different tissue prestressing algorithms on the results of FSI simulations of ATAA biomechanics was investigated. The ZPG and PT methods, were implemented. Furthermore, a novel methodology was proposed, the PTCAL, which couples the PT algorithm with a regional mapping of calibrated material properties. The results revealed that the PT and PTCAL models presented a good agreement with the ZPG models in terms of blood pressure and magnitude of WSS, and required around 60 % less iterations to achieve cycle-to-cycle convergence. However, neither approach presented a close agreement with ZPG regarding the direction of WSS. Regarding the simulation of the ATAA wall mechanics, the PT methodology revealed to produce a stiffer mechanical

response than the models using the ZPG approach. The PTCAL methodology, developed to address this issue, outperformed the PT models as it presented a significantly closer agreement with ZPG. These results highlight the need to consider a regional mapping of material properties when using the PT approach.

Chapter 5

Comparison of Numerical Models to Compute Biomechanical Markers in Ascending Thoracic Aortic Aneurysms

Abstract: Numerical modelling of Ascending Thoracic Aortic Aneurysms (ATAAs) biomechanics has the potential to improve current clinical guidelines. Fluid-Structure Interaction (FSI) is considered the gold-standard approach to perform this type of analysis, as it enables the simultaneous simulation of hemodynamics, structural mechanics and interaction between the blood and the aortic wall. Nonetheless, this significantly increases the reporting time of the simulations, which may hinder its application in routine clinical practices. The hypothesis tested in this work is that the increased stiffness of aneurysms allows the use of more straightforward numerical approaches without a significant impact in accuracy. Therefore, FSI, rigid wall and moving wall Computational Fluid Dynamics (CFD), Reduced Order Model (ROM) andComputational Solid Mechanics (CSM) models of ATAAs were developed using Computed Tomography Angiography (CTA) and Magnetic Resonance Imaging (MRI) data of patients that presented different degrees of stiffness. The numerical results for blood pressure, Wall Shear Stress (WSS) based metrics, maximum principal strain and maximum principal stress estimated by the FSI model were compared with the remaining models. The results showed that all numerical approaches estimated the pressure field with a close agreement with FSI. However, WSS were not accurately estimated by neither of the more straightforward approaches. The maximum principal strain and stress were overestimated by the CSM models using CFD driven pressure boundary conditions. Moreover, coupling CSM and ROM produced the closer agreement with FSI regarding the structural mechanics of ATAA.

Keywords: Ascending Thoracic Aortic Aneurysm (ATAA), Computational Fluid Dynamics (CFD), Computational Solid Mechanics (CSM), Computational cost, Fluid-Structure Interaction (FSI), Numerical accuracy, Reduced Order Model (ROM).

Contents

5.1 Relevance of modelling the fluid-structure interaction

To improve diagnosis and personalised treatment, numerical models have been proposed to estimate indicators of the risk of acute complications. These models solve the governing equations of fluid dynamics and structural mechanics. Accurate representation of Ascending Thoracic Aortic Aneurysms (ATAAs) biomechanics is crucial to estimate patient-specific intravascular flow patterns, Wall Shear Stress (WSS) based metrics and intramural stress distribution, for instance [219]. The most complete numerical model is the Fluid-Structure Interaction (FSI) which accounts for the multiphysics phenomenon and the interaction between the intra-aortic flow and the aortic wall [53, 114, 177, 186]. However, FSI simulations are usually computationally expensive. Computational Fluid Dynamics (CFD) and Reduced Order Model (ROM) analyses can recreate patient-specific hemodynamics. The first, may provide complete tridimensional time-resolved descriptions of hemodynamical quantities [56, 57, 156, 175]. Usually these simulations consider a rigid aortic wall. Nonetheless, moving boundary methods have also been applied to account for the effects of *in vivo* displacements [17, 18, 40, 63, 220]. The latter, is a more straightforward approach providing an average characterization of the hemodynamics across the ATAA centerline [110, 162, 221, 222]. Computational Solid Mechanics (CSM) is the solid mechanics counterpart to CFD, used to simulate the mechanical response of the aortic wall [115, 158, 172, 223–225]. It enables a complete tridimensional description of the intramural stress-strain state.

Despite the potential of numerical models to enhance current clinical guidelines, their introduction in real-life practices remains limited. In Chapter 3 [219], we identified three main issues: (i) developing fully patient-specific models remains challenging, which impacts the accuracy of numerical results; (ii) the excessive computational requirements turn these models unsuitable for routine clinical practice; and (iii) the lack of numerical validation against large patient cohorts.

In this chapter, the main objective is comparing the estimation of key biomechanical markers in ATAAs for a range of numerical models. We compared modelling approaches that vary in complexity and computational requirements, namely: FSI, rigid-wall and moving-wall CFD, ROM, and CSM. The biomechanical indicators considered in this work are blood pressure, WSS based metrics, maximum principal strain and maximum principal stress. This comparison was performed considering eight ATAA patients with distinct degrees of aortic wall stiffening.

This chapter is organized as follows: Section 5.2 presents the development of each the considered numerical models; the numerical results are presented in Section 5.3 and discussed in Section 5.4; and in Section 5.5 the main conclusions are summarized.

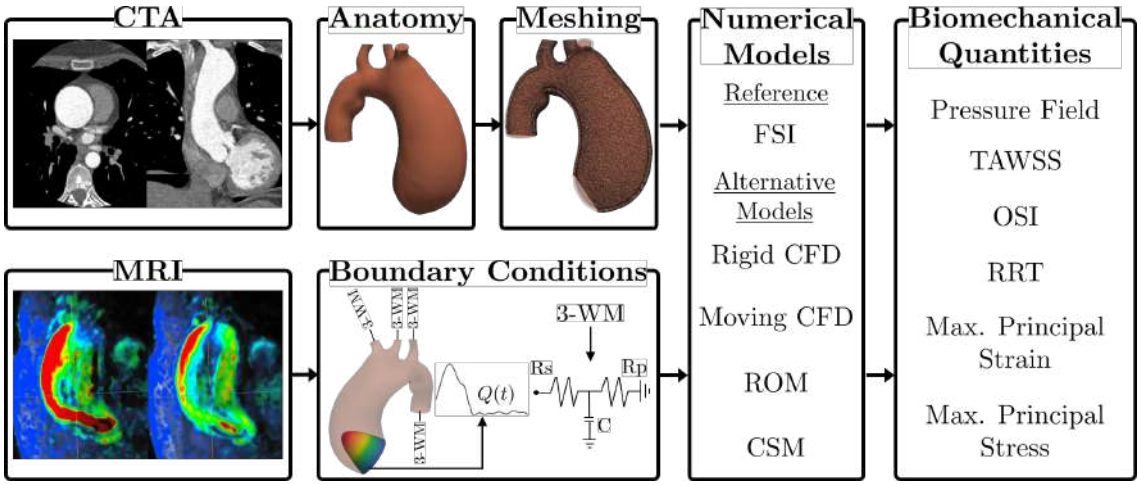

Figure 5.1: Schematic representation of the methodology employed to evaluate the relevance of alternatives to FSI modelling of ATAA hemodynamics and structural mechanics. Anatomic models and boundary conditions were derived from CTA and MRI data. These supported the development of CFD, ROM, CSM and FSI models. The results of the FSI model were considered the reference and compared with the alternative models in terms of pressure field, WSS based metrics, and maximum principal strain and stress.

5.2 Numerical modelling of ascending thoracic aortic aneurysm

An overview of the workflow adopted to assess how different numerical models estimate key biomechanical markers of ATAA is presented in Fig. 5.1. Medical imaging data of eight subjects was used to develop the numerical models. The patients were three females and five males, with ages in the range of 43–72. The patient-specific data (demographics, aortic diameters, valve type and heart function) is summarized in Table 5.1.

Table 5.1: Summary of patient-specific data (demographics, valve morphology, heart function).

Patient	**Age**	**Sex**	**Valve**	**MaxD** [mm]	**CardOut** [L min^{-1}]	**EjecFra** [%]	**Hrate** [bpm]
A	60	M	MAV	50.9	7.8	68.8	58.0
B	72	M	TAV	44.1	3.5	55.2	55.0
C	72	F	TAV	61.5	4.7	60.8	65.0
D	50	F	TAV	49.3	4.0	64.8	72.0
E	44	M	BAV	46.7	5.2	58.6	61.0
F	66	M	TAV	46.5	4.3	59.0	70.0
G	56	M	TAV	49.7	4.5	52.6	54.0
H	43	F	BAV	43.4	4.6	61.2	76.0

BAV = Bicuspid aortic valve, CardOut = Cardiac output, EjecFra = Ejection fraction, F = Biological female, Hrate = Heart rate, M = Biological male, MAV = Mechanical Aortic Valve, MaxD = Maximum diameter, TAV = Tricuspid aortic valve.

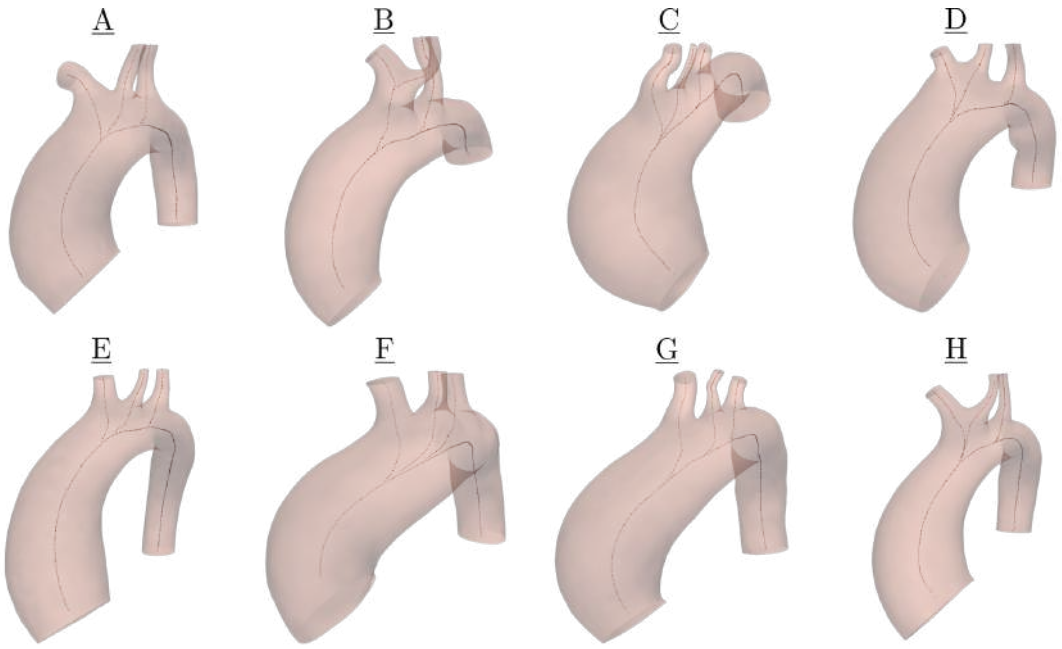

Figure 5.2: Final virtualization of the ATAA geometry for all patients.

5.2.1 Medical imaging data

We developed the numerical models using Computed Tomography Angiography (CTA) and 4D flow Magnetic Resonance Imaging (MRI) data acquired from the thorax. The *in vivo* data collection followed the research protocol of the AneurysmTool project (DOI: 10.54499/PTDC/EMD-EMD/1230/2021) approved by the ethics committee of the *Unidade Local de Saúde São José*. All participating patients provided written informed consent.

The CTA data was acquired using a revolution CT scanner (GE Healthcare, Milwaukee, WI, USA) after administering an iodinated contrast agent (Ultravist 370, Bayer, Leverkusen, Germany). Each patient underwent 21 ECG-gated acquisitions with a temporal resolution of 5 % of the cardiac cycle. Each scan produced a 512 ×512×292 voxel volume with an isotropic spatial resolution of 0.63 mm. This data enabled the segmentation of patient-specific anatomic models at the 0 % and 30 % of the cardiac cycle. The 0 % phase was used to generate the computational domains for biomechanical simulations. The 30 % phase was employed to estimate aortic wall properties. The segmentation process was performed using the open-source software 3D Slicer [212], requiring a combination of threshold and region-growing techniques. In the final virtualizations of each patient (Fig. 5.2), the inlet cut plane was placed just distal to the Sinus of Valsalva due to segmentation challenges in this region. Additionally, outlet boundaries were clipped to facilitate mesh generation.

The 4D flow MRI data was obtained using a 3T scanner (Signa, GE Healthcare, Milwaukee, WI, USA), without contrast medium. The acquisition consisted of 20 time instances throughout the cardiac cycle and the image resolution (RL-AP-SI) was 2.0

mm × 2.0 mm × 2.4 mm. Arterys software (San Francisco, CA, USA) was used to perform eddy current correction and data analysis during the post-processing of 4D flow data. The post-processed data defined the patient-specific inlet boundary conditions and calibrate three-element Windkessel models applied at the outlets. The assigned boundary conditions ensured the preservation of the mass conservation law.

5.2.2 Numerical models

Modelling the biomechanics of ATAA represents a multiphysics problem. In this regard, FSI is recognized as the most accurate numerical strategy. It solves both the blood dynamics and aortic wall mechanics, as well as, the interaction between the fluid, Ω_f, and solid, Ω_s, domains. The governing equations of the fluid, written in the ALE formulation, and solid domains are as follows:

$$\rho_f \left[\hat{\partial}_t \boldsymbol{v} + (\boldsymbol{v} - \boldsymbol{w}) \cdot \nabla \boldsymbol{v} \right] - \nabla \cdot \boldsymbol{\sigma}_f = 0 \qquad \wedge \qquad \nabla \cdot \boldsymbol{v} = 0, \qquad \text{in } \Omega_f \tag{5.1}$$

$$\rho_s \frac{\partial^2 \boldsymbol{u}}{\partial t^2} + \nabla \cdot (\boldsymbol{F}\boldsymbol{S}) = 0, \quad \text{in } \Omega_s \tag{5.2}$$

where ρ_f and ρ_s are the densities of the fluid and solid domains, respectively, ∇ denotes the gradient operator, $\boldsymbol{u}$ is the displacement field of the aortic wall, $\boldsymbol{F}$ is the deformation gradient tensor and $\boldsymbol{S}$ is the second Piola-Kirchhoff stress tensor.

We implemented the FSI model using SimVascular [211], which employs a monolithic approach. SimVascular uses the ALE formulation to manage mesh motion in the fluid domain through grid velocity, $\boldsymbol{w}$. The ALE time derivative, $\hat{\partial}_t$, resorts to the generalized-α scheme [213] to solve time integration of the velocity field, $\boldsymbol{v}$.

Table 5.2: Summary of the values selected for the three-element Windkessel model parameters, Young's modulus and aortic wall thickness.

Patient	Outlet	Hemodynamics			Structural Mechanics	
		R_s [MPa s m^{-3}]	C [m^3 Pa^{-1}]	R_p [MPa s m^{-3}]	E [MPa]	Th [mm]
A	DescA	10.0	6800.0	120.0	6.9	1.2
	BraT	30.0	2500.0	550.0		
	LCC	100.0	800.0	1660.0		
	LSC	150.0	1100.0	1900.0		
B	DescA	6.0	7500.0	160.0	1.9	1.4
	BraT	50.0	1100.0	1120.0		
	LCC	110.0	800.0	2840.0		
	LSC	120.0	1800.0	2575.0		
C	DescA	12.0	6500.0	180.0	5.2	1.0

	BraT	48.0	1100.0	1300.0		
	LCC	110.0	900.0	2220.0		
	LSC	120.0	1500.0	2400.0		
D	DescA	15.0	4000.0	300.0	1.0	1.8
	BraT	51.0	700.0	850.0		
	LCC	90.0	600.0	2000.0		
	LSC	70.0	1000.0	1700.0		
E	DescA	15.0	7500.0	160.0	0.7	1.6
	BraT	40.0	2500.0	780.0		
	LCC	100.0	1100.0	1750.0		
	LSC	200.0	1900.0	2800.0		
F	DescA	10.0	4200.0	200.0	21.8	1.5
	BraT	80.0	1900.0	1150.0		
	LCC	150.0	300.0	1650.0		
	LSC	230.0	800.0	2400.0		
G	DescA	10.0	3000.0	220.0	5.0	1.3
	BraT	55.0	900.0	720.0		
	LCC	120.0	300.0	1350.0		
	LSC	150.0	600.0	1950.0		
H	DescA	10.0	2500.0	300.0	1.3	1.4
	BraT	55.0	1100.0	750.0		
	LCC	120.0	300.0	1350.0		
	LSC	150.0	800.0	1850.0		

BraT = Brachiocephalic trunk, C = Artery compliance in $m^3\,Pa^{-1}$, DescA = Descending aorta, E = Young's modulus, LCC = Left common carotid, LSC = Left subclavian, R_p = Resistance of smaller arteries and arterioles in $MPa\,s\,m^{-3}$, R_s = Resistance of larger calibre arteries in $MPa\,s\,m^{-3}$, Th = Thickness of the aortic wall.

In this work, blood was modelled as a Newtonian and incompressible fluid, which are common assumptions for large-calibre arteries [56, 79, 127, 194]. The fluid density and dynamic viscosity were set to $\rho_f = 1060\,kg\,m^{-3}$ [53, 173, 180] and $\mu = 4 \cdot 10^{-3}\,Pa\,s$ [179, 180, 182], respectively. Additionally, we assumed laminar flow within the aorta [18, 54, 155, 181]. Regarding the boundary conditions, we prescribed patient-specific flow rates at the inlet considering a parabolic velocity profile and coupled the outlets with three-element Windkessel models. Table 5.2 presents the Windkessel models parameters used for each outlet and patient.

The aortic wall was modelled as a monolayer, isotropic and Neo-Hookean material. The strain energy density function in this case is written as:

$$\boldsymbol{W} = \mu^{\mathrm{s}} \left[\frac{I_1 - 3}{2} - \ln \boldsymbol{J} \right] + \kappa_{\mathrm{s}} \frac{(\ln J)^2}{2} \tag{5.3}$$

where $\boldsymbol{W}$ is the strain energy density function, I_1 is the first invariant of the right Cauchy–Green deformation tensor, $\boldsymbol{J}$ is the Jacobian of the deformation gradient, μ^{s} is the second Lamé parameter, and κ_{s} is the bulk modulus. The material properties required to define this constitutive model are Young's modulus, E, and Poisson's ratio, ν. We estimated the Young's modulus considering the volume of the segmentation at 30 % of the cardiac cycle as reference. The estimated Young's modulus for every patient, as well as, the considered aortic wall thickness, are presented in Table 5.2. The Poisson's ratio was set to 0.49 based on the available literature [79, 189], and the aortic wall density was set to 1120 kg m^{-3} [153, 201]. At the solid domain extremities, the out-of-plane displacements were fixed.

The reference configuration of the solid domain, Ω_{s}^0, was considered to be the image configuration (0 % of the cardiac cycle). To account for the initial stress state, induced by the continuous loading of the aorta during the cardiac cycle, the novel method proposed in Chapter 4 was used here.

At the interface between the domains, $\Gamma(t)$, kinematic and dynamic boundary conditions were enforced:

$$\boldsymbol{w} = \frac{\partial \boldsymbol{u}}{\partial t} \quad \wedge \quad \boldsymbol{\sigma}_{\mathrm{f}} \hat{\boldsymbol{n}}_{\mathrm{f}} + \boldsymbol{\sigma}_{\mathrm{s}} \hat{\boldsymbol{n}}_{\mathrm{s}} = 0 \,, \quad \text{in } \Gamma(t) \tag{5.4}$$

where $\boldsymbol{\sigma}_{\mathrm{s}}$ and $\boldsymbol{\sigma}_{\mathrm{f}}$ are the Cauchy stress tensor, and $\hat{\boldsymbol{n}}_{\mathrm{s}}$ and $\hat{\boldsymbol{n}}_{\mathrm{f}}$ are the unit normal to the surface, for the solid and fluid domains, respectively. These ensure that, at each time step, the displacement field estimated at the interface updates the fluid domain mesh, and the hemodynamics loads at the interface are transferred to the solid domain. The fluid and solid domain meshes were generated ensuring a nodal correspondence at the interface, which automatically satisfies these conditions. The meshing workflow is described in Valente et al. [52].

In addition to FSI, we implemented three additional numerical strategies using SimVascular to simulate ATAA hemodynamics, namely: (i) moving wall CFD; (ii) rigid wall CFD; and (iii) ROM. The moving wall approach estimates aortic hemodynamics considering the wall motion. In these simulations, the prescribed wall motion were the displacement fields estimated by FSI to ensure a better comparison between the approaches. The rigid wall simulations consider $\boldsymbol{w} = 0$ and non-slip boundary condition at the interface. The ROM solves the hemodynamics of ATAAs along the centreline. In this approach, each node on the centreline corresponds to a cross-section in the patient-specific geometry. SimVascular employs the continuity and momentum balance equations for 1D blood flow in an elastic domain, as derived by Hughes and Lubliner [226]:

$$\frac{\partial Q}{\partial t} + \frac{\partial}{\partial z}\left(\frac{4Q^2}{3A}\right) + \frac{A}{\rho_{\mathrm{f}}}\frac{\partial p}{\partial z} = \frac{\mu}{\rho_{\mathrm{f}}}\left(\frac{\partial^2 Q}{\partial z^2} - 8\pi\frac{Q}{A}\right) \quad \wedge \quad \frac{\partial A}{\partial t} + \frac{\partial (A\boldsymbol{v})}{\partial z} = 0, \quad \text{in } \Omega\_\mathrm{f} \tag{5.5}$$

where Q is the volumetric flow rate and z is the axial direction (along the centreline). To complete the system of equations, it is necessary to define a constitutive relation between the pressure and the cross-sectional area, A. In this case, a linear elastic material model was considered. The considered boundary conditions and modelling assumptions described for the FSI model were also applied to these models.

Regarding the structural mechanics, CSM models were also implemented. These models used the pressure fields estimated by the alternatives numerical strategies as boundary conditions applied at the inner surface fo the ATAA wall.

5.2.3 Biomechanical markers and statistical analysis

The primary objective of this work is to assess the relevance of using alternative numerical models, other than FSI, to simulate ATAA hemodynamics and structural mechanics. Hence, the numerical results of the FSI simulations were considered the ground-truth and compared with the results of the remaining models.

We used Bland-Altman plots to evaluate the agreement between the numerical strategies. For these plots, measurements of relevant biomechanical marker were considered at three slices locations across the volume of interest as shown in Fig. 5.3. Regarding ATAA hemodynamics, the pressure and WSS fields were analysed. Pressure was evaluated in terms of its minimum, p_{min}, and maximum, p_{max}, values. For the WSS field, three metrics were considered:

i) TAWSS, the time-averaged magnitude of WSS:

$$\text{TAWSS} = \frac{1}{T}\int_0^T |\text{WSS}(t)|\,\mathrm{d}t \tag{5.6}$$

ii) OSI, which quantifies directional changes in WSS over the cardiac cycle:

$$\text{OSI} = \frac{1}{2}\left(1 - \frac{\left|\int_0^T \text{WSS}(t)\,\mathrm{d}t\right|}{\int_0^T |\text{WSS}(t)|\,\mathrm{d}t}\right) \tag{5.7}$$

iii) RRT, an estimate of the residence time of blood near the wall:

$$\text{RRT} = [\text{TAWSS}\cdot(1 - 2\cdot\text{OSI})]^{-1} \tag{5.8}$$

The mechanical response of theATAA wall was analysed using the maximum principal stress, σ^{MaxP}, and strain, $\varepsilon^{\text{MaxP}}$, in a manner analogous to the WSS-based metrics.

In addition, this work investigates whether the agreement between the alternative numerical models and FSI correlates with the elasticity of the aortic wall. The agreement was quantified using the 75^{th} percentile of the nodal relative error, $\varepsilon_{\text{r}}^{75\text{th}}$, while wall elasticity was assessed through the distensibility coefficient, DC_{V}:

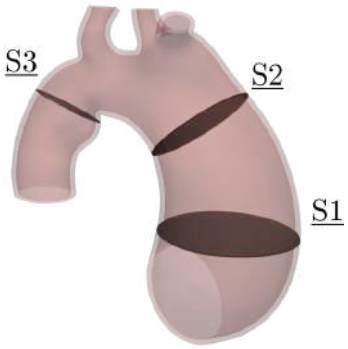

Figure 5.3: Location of the three slices (S1, S2 and S3) used for measuring the biomechanical markers of interest.

$$DC_V = \frac{V_{max} - V_{min}}{V_{min}(p_{max} - p_{min})} \tag{5.9}$$

where V_{max} and V_{min} represent the maximum and minimum volumes of the ATAA lumen, and P_{max} and P_{min} are the corresponding pressures. All values used to compute DC_V were obtained from the FSI simulations.

5.3 Numerical estimation of biomechanical biomarkers

In this work, we performed 7 simulations per patient, namely: rigid wall CFD (RW), moving wall CFD (MW), ROM, 3 CSM analysis (coupled with distinct pressure fields obtained by the hemodynamics simulations), and FSI. The simulations were performed using SimVascular in a workstation with an Intel Xeon Gold 6242R 3.10GHz CPU and 40 cores. The global results of the 75th percentile of the nodal relative error for each patient and numerical strategy are reported in Table 5.3. These results suggest that: (i) alternative approaches, in particular moving wall CFD and ROM, presents close agreement with FSI regarding the estimation of maximum and minimum pressures; (ii) although for most patients the alternative approaches are not reliable in estimating WSS, in some situations the moving wall simulations presents a close agreement with FSI; and (iii) coupling CSM with alternative approaches to simulate aortic hemodynamics estimates the maximum principal stress and strain with close agreement with FSI for the majority of the patients.

Table 5.3: Global results of the 75th percentile of the nodal relative error for each patient and numerical strategy.

Patient	Approach	p^{max}	p^{min}	TAWSS	OSI	RRT	σ^{MaxP}	ε^{MaxP}
A	RW	0.01	0.03	0.01	0.08	0.09	0.02	0.04
	MW	0.00	0.02	0.06	0.08	0.05	0.04	0.06
	ROM	0.01	0.01	0.98	—	—	0.05	0.07

B	RW	0.01	0.07	0.01	0.06	0.16	0.01	0.12
	MW	0.11	0.08	0.06	0.17	0.15	0.01	0.12
	ROM	0.01	0.01	0.94	—	—	0.07	0.03
C	RW	0.01	0.07	0.00	0.18	0.23	0.05	0.05
	MW	0.03	0.04	0.04	0.20	0.20	0.10	0.13
	ROM	0.02	0.02	0.98	—	—	0.10	0.06
D	RW	0.10	0.12	0.07	0.02	0.34	0.48	0.05
	MW	0.01	0.03	0.01	0.06	0.17	0.22	0.47
	ROM	0.00	0.00	0.98	—	—	0.22	0.47
E	RW	0.13	0.16	0.21	0.04	0.35	0.20	0.06
	MW	0.06	0.07	0.03	0.16	0.14	0.39	0.49
	ROM	0.01	0.01	0.89	—	—	0.31	0.38
F	RW	0.01	0.02	0.00	0.09	0.13	0.04	0.06
	MW	0.02	0.02	0.01	0.07	0.09	0.06	0.07
	ROM	0.01	0.01	0.92	—	—	0.00	0.00
G	RW	0.10	0.10	0.01	0.06	0.17	0.14	0.10
	MW	0.02	0.02	0.06	0.11	0.08	0.04	0.04
	ROM	0.06	0.03	0.99	—	—	0.08	0.06
H	RW	0.10	0.08	0.14	0.09	0.25	0.24	0.07
	MW	0.01	0.01	0.03	0.00	0.10	0.17	0.16
	ROM	0.00	0.00	0.79	—	—	0.18	0.17

5.3.1 Hemodynamics

Regarding the estimation of the maximum and minimum pressures, the agreement between FSI and alternative approaches is presented in Fig. 5.4. The rigid wall CFD simulations consistently overestimate maximum pressure, being the mean difference -6.47 ± 6.39 mmHg across all measurements, with differences reaching up to 20 mmHg. These differences are smaller for the minimum pressure. Nonetheless, for most measurements rigid wall CFD significantly underestimates this metric (mean difference of 5.9 ± 3.32 mmHg). The remaining approaches present a closer agreement with FSI, presenting most deviations in the range of ±3 mmHg. Moving wall CFD produces estimations with mean differences of -0.7 ± 5.0 mmHg and 0.9 ± 3.1 mmHg for the maximum and minimum pressures, respectively. Resorting to ROM, produced the results with the closer agreement against FSI which presented mean differences of -0.5 ± 0.7 mmHg and -0.5 ± 0.9 mmHg for the maximum and minimum pressures, respectively.

The relevance of using alternative approaches to estimate WSS based metrics is analysed in Fig. 5.5 and Fig. 5.6. Regarding the Time-Averaged Wall Shear Stress (TAWSS),

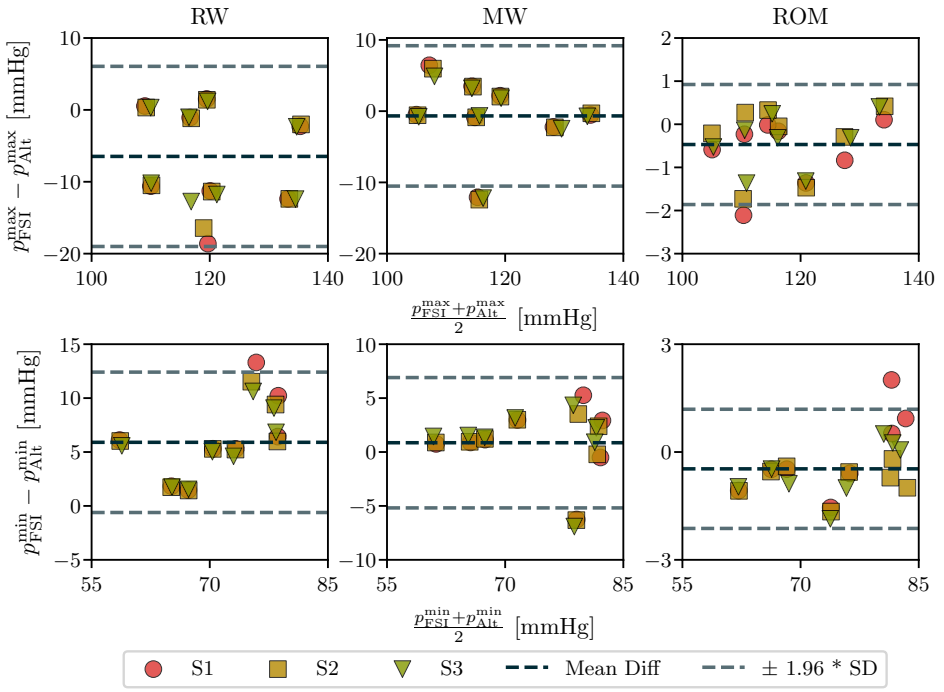

Figure 5.4: Agreement between FSI and alternative approaches regarding hemodynamics: Bland-Altman plots of the minimum and maximum pressures estimated by all approaches at slices S1, S2 and S3.

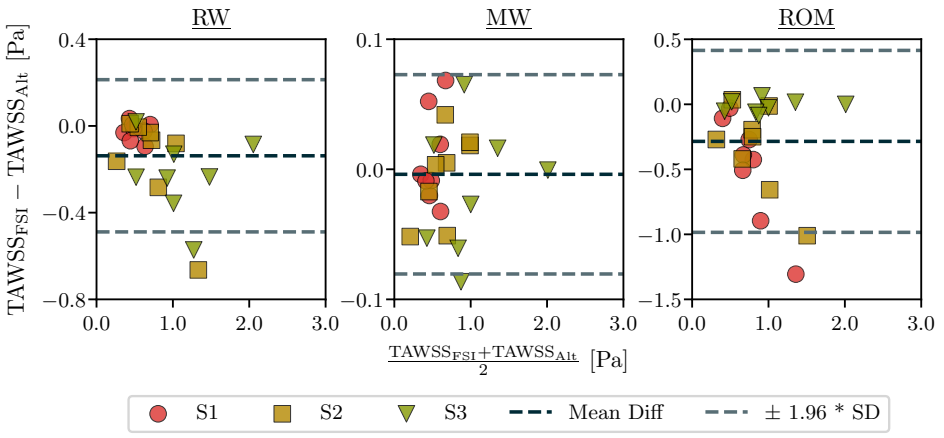

Figure 5.5: Agreement between FSI and alternative approaches regarding hemodynamics: Bland-Altman plots of the TAWSS estimated by all approaches at slices S1, S2 and S3.

both the rigid wall CFD and ROM simulations consistently overestimate this metric, presenting mean differences of -0.2 ± 0.2 Pa and -0.3 ± 0.4 Pa, respectively. It is worth noting, however, that ROM predictions in the region of the descending aorta (S3) show close agreement with FSI. Among all numerical strategies, the moving wall CFD presented the closer agreement with FSI, with mean differences of 0.0 ± 0.1 Pa.

A significant limitation of the ROM simulations is that only estimates the WSS magnitude, which prevents the computation of Oscillatory Shear Index (OSI) and Relative

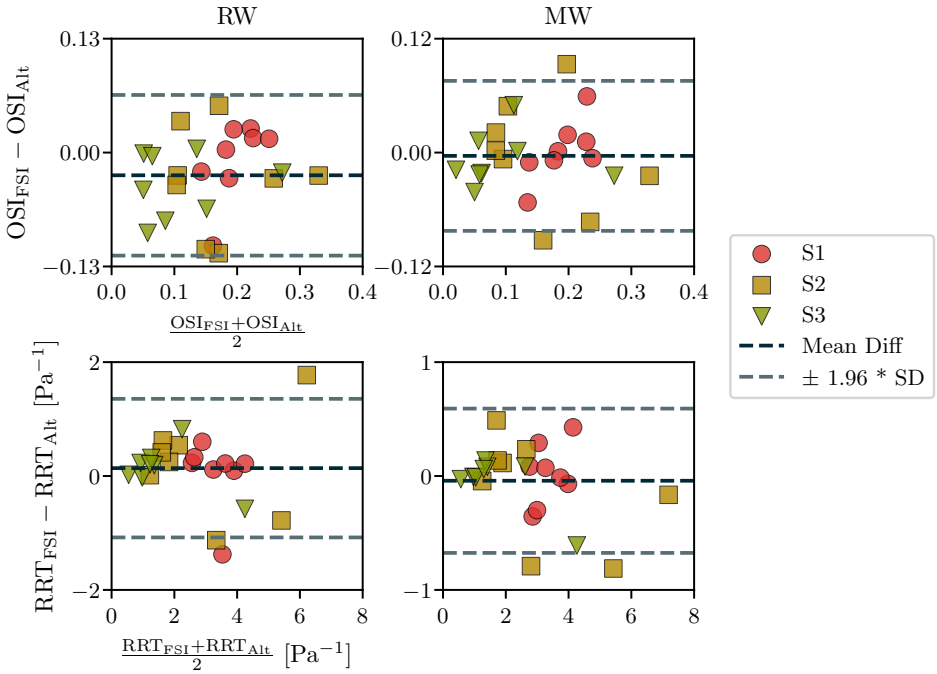

Figure 5.6: Agreement between FSI and alternative approaches regarding hemodynamics: Bland-Altman plots of the OSI and RRT estimated by all approaches at slices S1, S2 and S3.

Residence Time (RRT). For the remaining approaches, while the mean differences in OSI and RRT are small, the variance is high. Specifically, the rigid wall simulations yield mean differences of -0.03 ± 0.05 and 0.14 ± 0.62 Pa^{-1} for OSI and RRT, respectively. The moving wall simulations perform slightly better, with mean differences of -0.01 ± 0.04 and -0.04 ± 0.32 Pa^{-1} for OSI and RRT, respectively.

5.3.2 Structural mechanics

The results of the agreement between the numerical strategies regarding the estimated maximum principal stress and maximum principal strain is presented in Fig. 5.7. Coupling CSM with the pressure field estimated by rigid wall, moving wall and ROM simulations shows a close agreement with FSI for most measurements in both of these metrics. In the estimated maximum principal stress, the mean differences are -5.0 ± 5.0 kPa, 3.8 ± 4.8 kPa and 4.5 ± 4.5 kPa, respectively. Regarding the maximum principal strain, the mean differences are -0.1 ± 0.5, 0.4 ± 0.8 and 0.3 ± 0.8, respectively.

5.3.3 Impact of aortic wall stiffness on the differences between numerical approaches

In Fig. 5.8 shows the correlation between the 75^{th} percentile of the nodal relative error and the stiffness of the aortic wall for the different alternative numerical strategies. Overall, these results suggest that increasing the compliance of the wall also increases the error

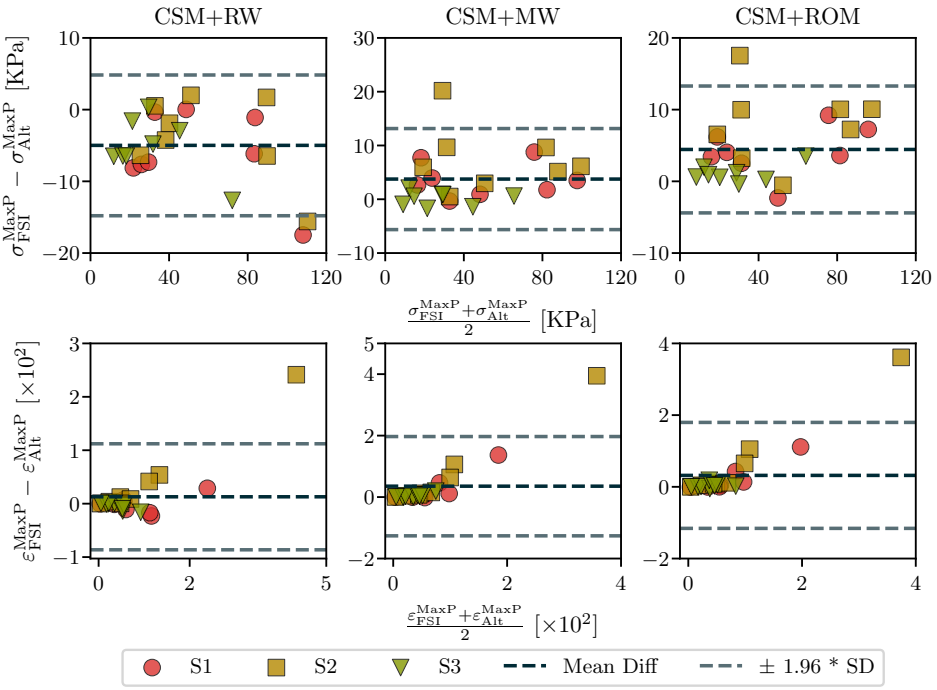

Figure 5.7: Agreement between FSI and alternative approaches regarding structural mechanics: Bland-Altman plots of the maximum principal stress and strain estimated by all approaches at slices S1, S2 and S3.

between FSI and the remaining approaches. Regarding the maximum and minimum pressures, this is more evident for the rigid wall and moving wall simulations. ROM presented the smaller error in these metrics across all degrees of stiffness (close to 0% for most patients). In respect to the TAWSS, ROM produced estimations with an error close to 95%. The remaining approaches produced good approximations of this metric. OSI seems to be the only variable where the correlation between the error of using alternative numerical strategies and the stiffness of the aortic wall is negative, in particular for the rigid wall simulations. Regarding the RRT, as the elasticity of the wall increased the moving wall simulations outperformed the rigid counterparts. Regarding the structural mechanics variables, the same positive trend is found. One exception to this trend is the maximum principal strain estimated by coupling CSM and rigid wall simulations.

5.4 Impact of different modelling approaches in estimating biomechanical markers

Modelling the interaction between blood and the aortic wall is the gold-standard approach to recreate patient-specific biomechanics of ATAAs. This approach yields numerical results with higher accuracy at the cost of elevated computational requirements and reporting time. The use of FSI frameworks is as more relevant as more compliant the analysed system is. As aneurysms are a direct consequence of increased stiffness of

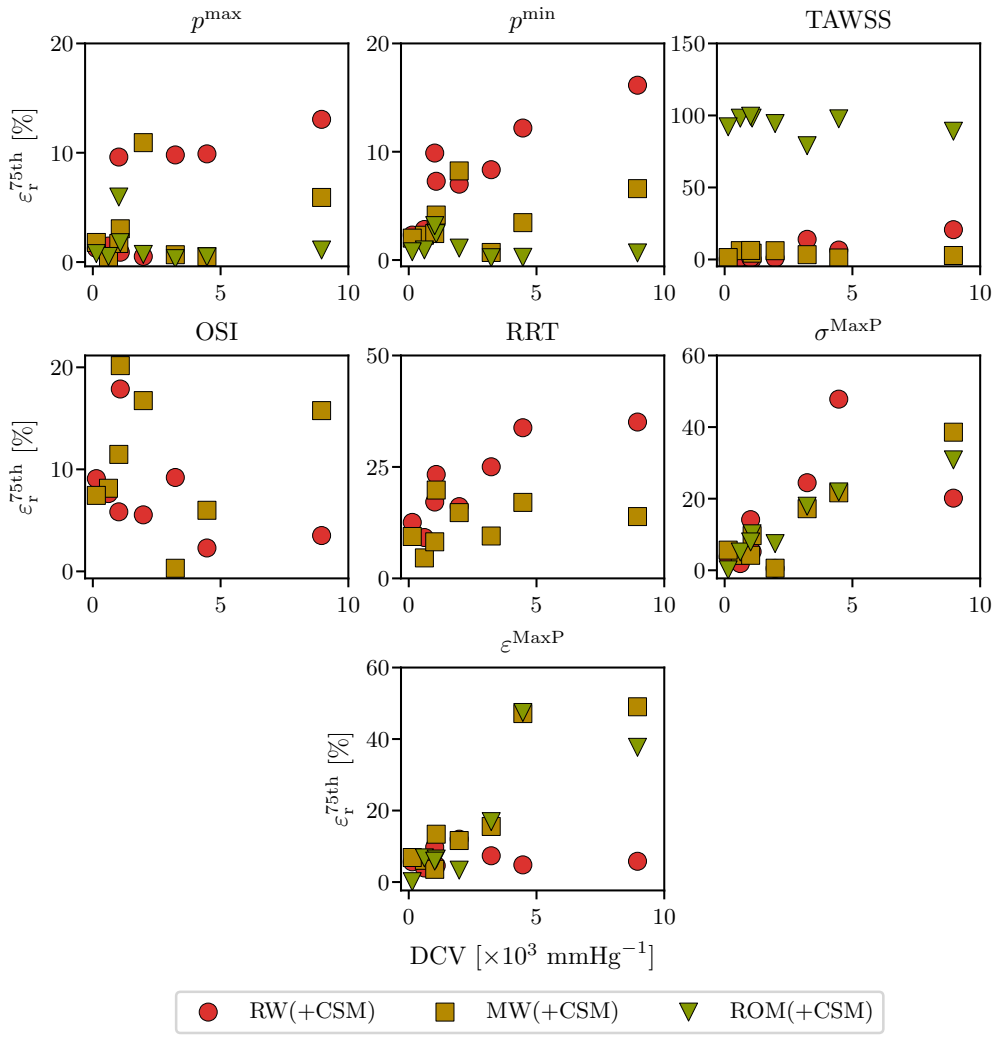

Figure 5.8: Correlation between the 75th percentile of the nodal relative error and aortic wall stiffness.

the aortic wall, other more straightforward modelling approaches, such as CFD, ROM and CSM, may be as accurate as FSI.

Regarding the modelling of ATAA hemodynamics, the intraluminal pressure is a key variable to estimate the aortic wall mechanics. All implemented numerical strategies were able to estimate pressure fields with a close agreement with FSI. Nonetheless, the ROM and moving wall simulations presented the closest agreement for the more compliant ATAA wall due to considering the deformation of the lumen during the cardiac cycle.

The analysis of WSS fields is also highly relevant due to its known correlation with the risk of acute complications [96, 218] and progression of aneurysms [227, 228]. The rigid wall analysis significantly overestimated the average WSS magnitude when compared to FSI. The moving wall CFD simulations presented a close agreement with FSI when estimating the average WSS magnitude. Despite this, neither of the numerical strategies accurately reproduced the variation in the direction of this vector. Additionally, ROM is

not a suitable approach to estimate the WSS field due to the fact that assumes a parabolic flow along the centreline. These findings are in accordance with previous reports in the literature. Reymond et al. [229] compared the hemodynamics of one patient-specific healthy aorta, estimated by 2-way FSI, CFD and ROM frameworks and was reported that the pressure field estimated by CFD and ROM models presented a close agreement with FSI. The WSS were significantly impacted by the motion of the aortic wall, revealing significantly different results between the CFD and FSI models, in particular in the ascending aorta where diameter changes throughout the cardiac cycle are higher. Mendez, Di Giuseppe, and Pasta [123] employed a similar methodology to compare the hemodynamics of 11 patient-specific ATAA geometries estimated by rigid wall CFD and FSI simulations. The results revealed a slightly better correspondence of WSS than reported by Reymond et al. [229] which was attributed to the stiffer aneurysms. Soudah et al. [230] and Jin and Alastruey [231] explored the use of ROM to estimate the hemodynamics of aortic aneurysm. In both works a close agreement with FSI modelling was reported regarding the estimated pressure field. Bonfanti et al. [232] introduced the moving-boundary method to CFD models as a simplified approach to account for wall motion in patient-specific aortic dissection models and compared the results with FSI simulations. The estimated pressure by this approach presented a below 2 % error and similar WSS distributions when compared to FSI simulations. Also, Calò et al. [40] studied the impact of wall movement on ascending aortic blood flow by applying the moving-boundary method to CFD simulations and comparing the results with traditional rigid wall simulations. It was reported that the wall movement had a significant impact on secondary flow patterns and WSS directional changes.

With respect to calculating the maximum principal stress and strain, resorting to CSM instead of FSI tends to underestimate both quantities, considering the same pressure differential during the cardiac cycle. This aspect becomes increasingly more evident as the stiffness of the aortic wall decreases. Nonetheless, coupling CSM with moving wall CFD or ROM driven boundary conditions presented a close agreement with FSI in estimating the maximum principal stress and strain for distensibility coefficient below 5×10^{-3} mmHg^{-1}.

Choosing the adequate numerical approach to estimate any system is always dependent on the specific objectives of each model. Regarding modelling the biomechanics of ATAAs, the objective is to contribute to the improvement of current clinical practices. This aspect imposes a practical limitation related to the reporting time of simulations. Coupling CSM and moving-wall or ROM, which effectively recreates a 1-way FSI model, represent potential time-effective approach in regards to the estimation of ATAA pressure field, maximum principal stress and maximum principal strain. This type of model could be used as a complementary clinical exam and contribute to improving the stratification of the ATAA risk of rupture at the time of the medical imaging acquisitions.

A complementary medical exam could also be the estimation of aneurysm progression throughout long time scales. In this case, FSI seem to still be the gold-standard approach

due to the relevance of WSS to the growth and remodelling of the aortic wall. In recent decades, Artificial Intelligence (AI) based tools have emerged as a potential solution to reduce the reporting time of numerical modelling and contribute to the implementation of numerical models into real-life clinical practices. One way to achieve this is by developing surrogate models, using the data produced by the numerical models to train AI based tools, such as tree-based algorithms, support vector regression and neural networks. Several reports in the literature already present the development of surrogate models of aortic biomechanics [122, 233–235]. In future works, we aim to develop a surrogate model of the ATAA wall mechanics using the numerical results of the coupling of CSM and ROM models.

5.5 Main remarks

In this paper, we compared biomechanical markers predicted by different numerical strategies in 8 patient-specific ATAA. We found that neglecting FSI can be justified depending on the stiffness of the aortic wall. All numerical approaches presented a close agreement with FSI regarding the estimation of the pressure field for the higher stiffness patients. Using FSI modelling is the gold-standard approach to estimate patient-specific WSS as the remaining approaches were unable to replicate the changes in direction during the cardiac cycle. Coupling CSM and moving wall or ROM driven pressure boundary conditions produced estimations of maximum principal stress and strain similar to the FSI model, except for the most compliant case. This work highlights that more straightforward numerical approaches such as coupling CSM and ROM may represent time-efficient tools capable of being introduced into clinical practices and used to improve the stratification of the ATAA risk of rupture at the time of the medical imaging data acquisitions.

Chapter 6

Coupling Computational Solid Mechanics and Deep Learning for Surrogate Modelling of Aortic Wall Mechanics

Abstract: ATAAs require accurate biomechanical assessment. However, current numerical approaches are too computationally demanding for routine clinical use. This work proposes a deep learning-based surrogate model to overcome this limitation. A Statistical Shape Model (SSM) was developed from a dataset of patient-specific ascending aortas. The global anatomical features derived from the Principal Component Analysis (PCA), coupled with material and loading parameters, were used as inputs for a Deep Neural Network (DNN). The network was trained to predict stress and strain fields, using Computational Solid Mechanics (CSM) simulations as reference. Model performance was assessed both on synthetic PCA-driven geometries and on the original patient-specific anatomies. The surrogate model reproduced the spatial distributions of the second Piola-Kirchhoff and right Cauchy-Green fields with high reliability. For PCA-driven geometries, around 99% of the test cases achieved at least moderate agreement with reference simulations. For patient-specific anatomies, more than 95% of the predictions showed at least moderate agreement. Errors were mainly associated with low-pressure loading conditions, while no clear dependency was found on shape or material inputs. The results highlight the potential of data-driven approaches to accelerate patient-specific biomechanical assessments, paving the way for integration into future clinical decision-support systems.

Keywords: Ascending Thoracic Aortic Aneurysm (ATAA), Computational Solid Mechanics (CSM), Deep learning, Deep Neural Networks (DNN), Patient-specific, Surrogate

modelling.

Contents

6.1 Surrogate modelling of biomechanical systems

Simplified models that closely replicate the outputs of high-fidelity simulations, allow drastic reductions in the calculation time. Thus, surrogate modelling is particularly valuable in scenarios where the extensive reporting time of numerical models imposes a strong practical constraint [123, 236]. In the realm of cardiovascular biomechanics analysis, surrogate models may be used to increase the efficiency of numerical simulations of Ascending Thoracic Aortic Aneurysms (ATAAs) biomechanics and, therefore, improve current clinical guidelines. On one hand, numerical modelling has proved its ability to accurately recreate the conditions of biological systems, including cardiovascular systems [53, 114, 177, 186]. On the other hand, surrogate models are able to reduce the computational cost of numerical models, while maintaining a acceptable level of accuracy [236, 237].

Over the past few decades, a variety of techniques have been used to develop surrogate models of biomechanical systems. These techniques vary in complexity and formulation, ranging from classical regression methods to more advanced approaches such as Gaussian process regression [238, 239] and Artificial Intelligence (AI) [240, 241]. Gaussian processes were, for instance, used by Di Achille et al. [242] to assist on the estimations of mechanical parameters of the left ventricular myocardium. Regarding AI-based approaches, Liang et al. [243] trained Deep Neural Network (DNN) with Computational Solid Mechanics (CSM) data of the aortic wall to estimate the deformation field under a fixed pressure load; Moura et al. [244] developed surrogate models of the pelvic floor dynamics during vaginal delivery using tree-based algorithms (random forests and extreme gradient boosting), support vector regression, and Artificial Neural Networks (ANN). These aimed to estimated the maximum principal stress distribution along the pelvic floor muscle at different stages of fetal head descent; and Sajjadinia, Carpentieri, and Holzapfel [245] used graph neural networks to develop multiscale surrogate models of knee cartilage.

In this chapter, we present a surrogate modelling framework that couples CSM simulations and neural networks to reproduce aortic wall mechanics in patient-specific geometries. This model aims to estimate the second Piola-Kirchhoff stress and deformation gradient tensors distribution along the aortic wall. The surrogate model is based on a neural network architecture trained with numerical data. We used mesh/morphing techniques and Principal Component Analysis (PCA) to encode the information regarding the aortic geometry. Material and hemodynamic variability was also included through parameters such as wall thickness, Young's modulus, and blood pressure.

The remainder of this chapter is organised as follows: Section 6.2 details the methodology employed to generate the database of numerical data and train the neural network; Section 6.3 present the results of the surrogate model performance; Section 6.4 discusses the main findings; and Section 6.5 concludes the chapter with a summary of the contributions.

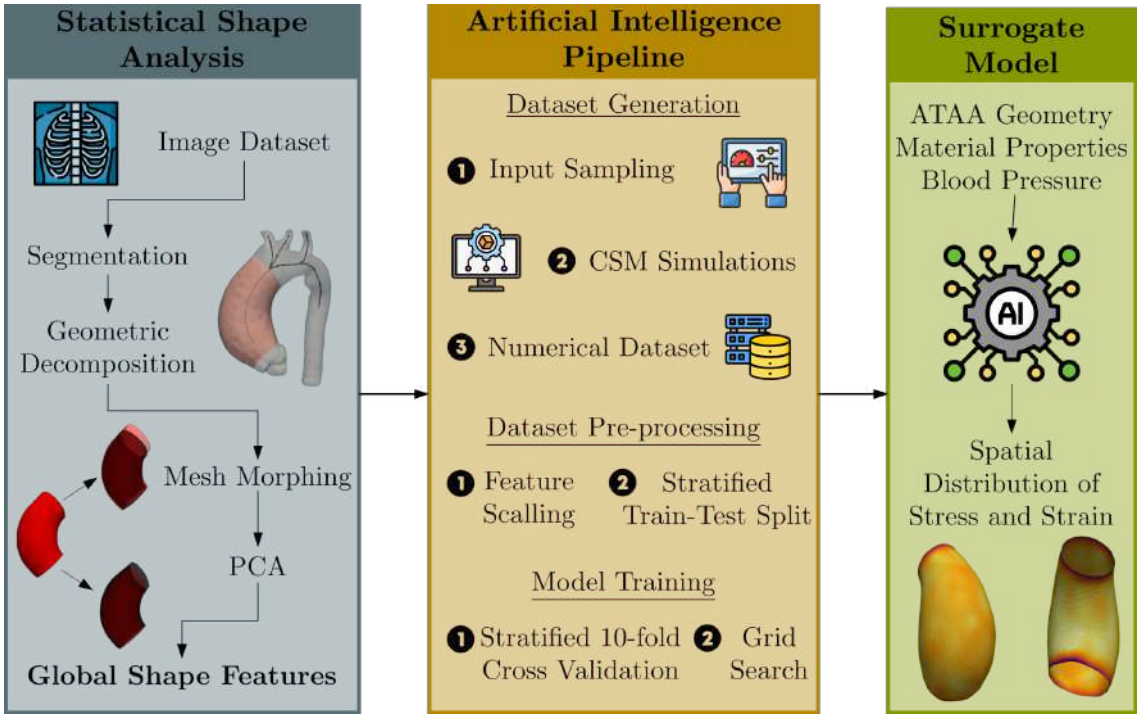

Figure 6.1: Overview of the methodology employed to develop an AI-based surrogate model of ATAA wall mechanics. Statistical shape analysis was applied to an image dataset to extract global shape features via PCA. These features, combined with material properties and blood pressure, were used to generate a dataset of CSM simulations. The dataset was pre-processed and employed to train the surrogate model using stratified 10-fold cross-validation and grid search. The trained model predicts the spatial distribution of wall stress and strain.

6.2 Surrogate modelling of aortic wall mechanics

The main purpose of this chapter is to develop an AI-based surrogate model of ATAA structural mechanics. In Fig. 6.1 we present the workflow of the proposed surrogate model which consists in three main steps: (i) statistical shape analysis; (ii) numerical simulations of ATAA wall mechanics; and (iii) AI pipeline.

6.2.1 Patient-specific anatomy dataset

This work utilized patient-specific Computed Tomography Angiography (CTA) data from 70 individuals diagnosed with ATAAs, comprising cases with both BAV and Tricuspid Aortic Valve (TAV). All patients were recruited under the scope of the AneurysmTool project (DOI: 10.54499/PTDC/EMD-EMD/1230/2021) and provided written informed consent. The study protocol was approved by the Ethics Committee of the *Unidade Local de Saúde São José*.

Aortic lumen segmentations were obtained at two phases of the cardiac cycle using a in-house build multi-view 2D U-Net. This method employs three independently trained U-Net encoder-decoder architectures, corresponding to the axial, coronal, and sagittal

planes, in order to balance segmentation accuracy and computational efficiency. A total of $K = 94$ segmentations were generated with at least one of each patient. Issues were found in some segmentations and excluded from the study.

Following segmentation, the ascending aorta was geometrically isolated to focus the analysis on this region of interest. This was achieved by slicing the aortic lumen at the sinotubular junction and at the first ostium of the brachiocephalic artery. The extraction process relied on computing the aortic centreline using the inscribed sphere method and Voronoi diagram-based techniques.

6.2.2 Mesh morphing

Developing a Statistical Shape Model (SSM) of the ATAA requires generating a set of isotopological meshes that represent patient-specific anatomies. This was accomplished through a two-step procedure. First, all segmented ATAA surfaces were spatially aligned with a reference mesh using an Iterative Closest Point (ICP) algorithm to ensure consistent anatomical orientation. Second, the aligned reference mesh was deformed to fit each target surface using radial basis function mesh morphing. A thin plate spline kernel was selected to interpolate displacements across the 3D domain.

A key challenge in morphing anatomical structures lies in the absence of distinct anatomical landmarks. To address this, we developed an automated approach for extracting pseudo-landmarks, referred to as Source Points (SP), to guide the morphing process. These SP were defined by uniformly sampling previously extracted centreline-based splines along the aortic wall. For each geometry, 16 SP were selected per spline across 10 cross-sectional planes.

The initial reference mesh was chosen as the surface corresponding to the average ATAA diameter and centreline length across the dataset [246, 247]. A triangular surface mesh was then generated using the TetGen libraries within the SimVascular framework [211], comprising $n = 1354$ elements.

To reduce mesh distortion and improve consistency across the dataset, a refined template was generated by averaging the initially morphed meshes. The entire morphing procedure was then repeated using this mean template as the new reference. This iterative refinement yielded a robust and consistent set of isotopological meshes for all patient-specific geometries.

6.2.3 Statistical shape analysis

A statistical shape analysis was conducted on the isotopological surface meshes to identify global shape features of the ATAA. PCA was employed for this purpose, implemented in Python using the *scikit-learn* library. The resulting low-dimensional representation enabled compact characterization of each patient-specific geometry and was later used as input for the surrogate model.

The spatial coordinates of each mesh were vectorized by concatenating the x, y, and z components of all n mesh nodes, resulting in a data matrix of size $K \times 3n$. Prior to PCA, the matrix was standardized using the *StandardScaler* function to ensure zero mean and unit variance for each coordinate dimension across the dataset.

PCA was then applied to extract the principal modes of geometric variation. The first six principal components, ranked by decreasing explained variance, were retained for further analysis. Together, these components accounted for around 90% of the cumulative morphological variance in the geometries dataset. The corresponding modes describe major patterns of morphological variation in the ATAA, such as elongation, dilation, and asymmetry.

6.2.4 Computational solid mechanics model of the aortic wall

The mechanical response of the ATAA wall throughout the cardiac cycle was simulated using CSM simulations. The primary objective was to estimate the spatial distributions of the second Piola-Kirchhoff stress tensor, $\boldsymbol{S}$, and the right Cauchy-Green deformation tensor, $\boldsymbol{C}$, under physiological pressure loading. These quantities were later used as output targets for the surrogate model.

The solid domain was generated by extruding the isotopological surface meshes along the outward normal direction, assuming a uniform wall thickness. The resultant surface mesh of the ATAA wall was then meshed using the Gmsh library. A Python-based pipeline was developed to automate this step, ensuring consistent mesh generation across all patient-specific geometries.

The aortic wall was modelled as a homogeneous, isotropic, incompressible, and Neo-Hookean material. A monolayer structure with constant wall thickness was assumed for all geometries. To better reflect physiological conditions, prestressing was included, following the method described by Hsu and Bazilevs [129]. This approach estimates the Prestress Tensor (PT) required to balance the hemodynamic loads at the diastolic phase, thus estimating the intramural stress state of the aortic wall. As for boundary conditions, a homogeneous pressure load was applied to the luminal surface of the aortic wall. The pressure values followed an idealized curve. At the proximal and distal extremities of the domain, the displacements were fixed.

All simulations were carried out using SimVascular on a workstation equipped with an Intel Xeon Gold 6242R 3.10 GHz CPU and 40 cores. A total of 4000 simulations were attempted, of which 3911 were successfully completed. The aortic wall density and Poisson's ratio were fixed at 1120 $\mathrm{kg\,m^{-3}}$ [153, 201] and 0.49 [79, 189], respectively. Computational settings, including the time step size and number of time steps, were kept constant across all simulations. The varying variables included the wall thickness and Young's modulus, sampled from uniform distributions $U(1, 2.5)$ mm [248] and $U(1, 4)$ MPa [249], respectively. The diastolic and systolic pressures also varied and followed normal distributions $N(80, 16)$ mmHg and $N(120, 16)$ mmHg, respectively.

In addition to varying mechanical and loading parameters, 500 ATAA geometries were synthetically generated by sampling the first six PCA modes. Each mode was sampled from a normal distribution with zero mean and variance equal to the corresponding eigenvalue of the PCA covariance matrix, enabling the creation of anatomically plausible yet diverse shapes.

6.2.5 Artificial intelligence pipeline

6.2.5.1 Dataset generation

The dataset used to train the surrogate model was constructed from the results of the CSM simulations described previously. From each simulation, 20 samples were extracted, corresponding to 20 different loading states throughout the cardiac cycle. Each sample was defined by a unique combination of geometry, material properties, and loading conditions, resulting in a total of $m = 78220$ samples.

Each data sample consisted of an input-output pair. The input vector contained 10 features. The first six corresponded to the first six PCA modes, representing the patient-specific geometry. The remaining four included wall thickness, Young's modulus, diastolic pressure, and the instantaneous pressure applied.

The output vector captured the nodal distribution of two tensor fields: the second Piola-Kirchhoff stress tensor and the right Cauchy-Green deformation tensor. For each node in the isotopological mesh, the six unique components of each tensor (due to symmetry) were recorded. As a result, each row of the output dataset had a length of $n \times 12$, with the first half corresponding to the components of $\boldsymbol{S}$ and the second half to those of $\boldsymbol{C}$.

6.2.5.2 Data pre-processing

To improve the robustness of the training process and ensure balanced data distribution across training, validation and testing splits, a stratified sampling strategy was employed. Specifically, the dataset was clustered using the *KMeans* algorithm, based on the input features. These clusters were then used to perform a stratified shuffle split via the *StratifiedShuffleSplit* function from the *scikit-learn* library. The data was divided into training (80%) and testing (20%) sets. Within the training set, an additional 10% was reserved for validation, resulting in final proportions of 72% for training, 8% for validation, and 20% for testing.

All input features were standardized using the *StandardScaler* from *scikit-learn*, applied only to the training data to avoid data leakage. The scaling parameters computed from the training set were then used to transform both the validation and testing sets, maintaining consistency across the datasets. Additionally, this transformation was performed independently for groups of variables with the same order of magnitude. For instance, the PCAs modes were scaled together, while the wall thickness, Young's modulus, and pressure values were scaled separately.

Table 6.1: Final hyperparameters used in the training of the surrogate model.

Hyperparameter	Value
Hidden layers	64, 128, 256, 512, 1024
Activation function	ReLU
Batch size	400
Optimizer	Adam
Dropout rate	0.2
Epochs	152

6.2.5.3 Model training

To perform regression operations, in particular when coupling CSM data and AI, neural networks are the most commonly used approach [250]. There are also known for being capable of handling nonlinear relationships between high-dimensional input and output data [251]. This is particularly relevant, as the developed model aims to estimate the nodal distribution of the second Piola-Kirchhoff stress and right Cauchy-Green deformation tensors. Also, this model was implemented using the *PyTorch* framework.

To identify the optimal set of hyperparameters, a grid search (*GridSearchCV*) strategy was employed in combination with stratified 10-fold cross-validation (*StratifiedKFold*). The grid search exhaustively evaluated combinations over a predefined parameter space, including learning rate, number of hidden layers, number of neurons per layer, dropout rate, and batch size. The final hyperparameters used for training are summarized in Table 6.1.

The loss function used during training was suggested by Ghazi et al. [252], which aims to penalize more for elements with higher variation across the training samples. The loss function is as follows:

$$\text{loss} = \frac{1}{n \times m} \sum_{i=1}^{n} \left(\sum_{j=1}^{m} s_i \left(y_i - \hat{y}_i \right)^2 \right) \tag{6.1}$$

where n is the number of nodes, m is the number of samples, s_i is the standard deviation of the i-th node across all samples, y_i is the true value at the i-th node, and $\hat{y}_i$ is the predicted value at the same node.

6.2.5.4 Performance metrics

To evaluate the performance of the trained DNN, two metrics were computed across all testing samples: the normalized mean absolute error, NMAE, and the Pearson correlation coefficient, R. The NMAE was computed as:

$$\text{NMAE} = \frac{1}{m} \sum_{i=1}^{m} \frac{|y_i - \hat{y}_i|}{\max(y_i) - \min(y_i)} \tag{6.2}$$

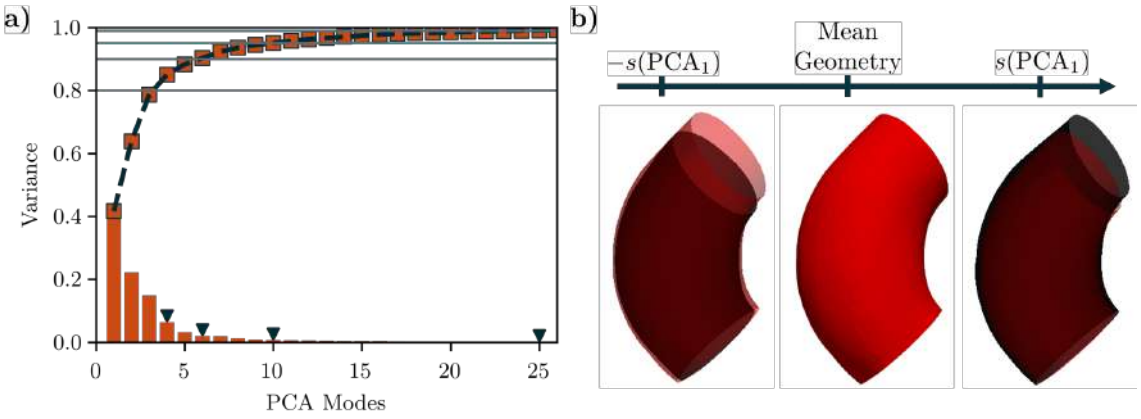

Figure 6.2: Results of the SSM: a) compactness curve of the PCA (the symbols mark the number of modes required to capture 80%, 90%, 95%, and 99% of the cumulative variance), and b) geometric variations imposed by the first PCA mode on the mean shape (bright red).

These metrics were estimated independently for the predicted distributions $\boldsymbol{S}$ and $\boldsymbol{C}$. Additionally, the same analysis was repeated for the subset of patient-specific ATAA geometries. To better access the performance of the surrogate model, two thresholds for success were defined:

- Moderate agreement: R > 0.8 and NMAE < 0.2
- High agreement: R > 0.95 and NMAE < 0.05

6.3 Surrogate model results

6.3.1 PCA results

Concerning the results of the SSM, Fig. 6.2-a shows the compactness curve. The first mode alone captures approximately 42% of the anatomical variation in the sample of patient-specific geometries characterized with isotopological meshes. The Second and third modes represent 22% and 15%, respectively. Together, these three modes account for nearly 80% of the variability. The 90%, 95%, and 99% thresholds of the compactness curve were reached using 6, 10, and 25 PCA modes, respectively. Fig. 6.2-b illustrates the changes in geometry obtained by varying the first PCA mode around the mean shape.

6.3.2 Neural network performance

6.3.2.1 Case 1 – PCA driven geometries

Figure 6.3 summarizes the NMAE and R of all test samples. For the predictions of the second Piola-Kirchhoff stress tensor components, 99% and 96% of the samples showed a moderate and high agreement, respectively. For the predictions of the right Cauchy-Green deformation tensor, 99% and 95% of the samples fell into these categories, respectively.

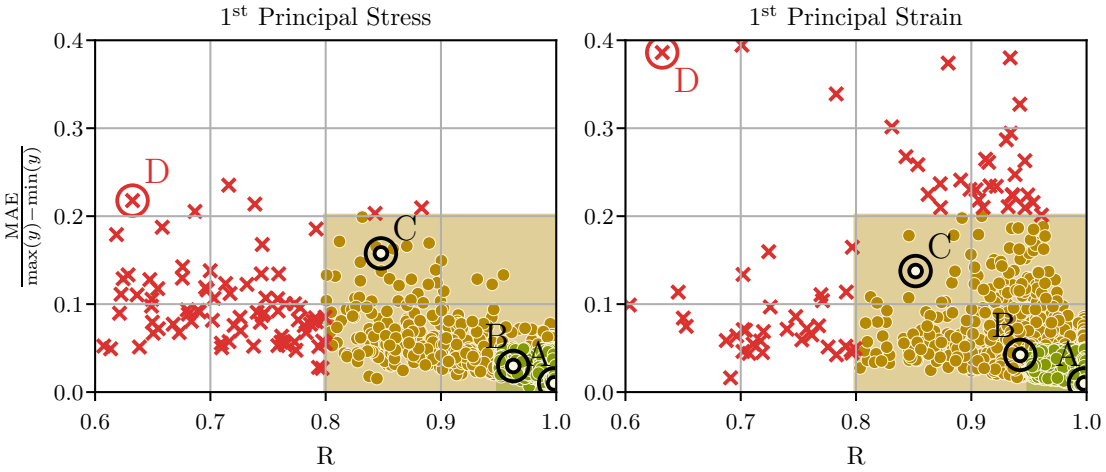

Figure 6.3: DNN performance overview: summary of the NMAE and R for all test samples.

Fig. 6.4 and Fig. 6.5 present the surface representations of the first principal stress and strain for four representative test cases. These examples cover different levels of agreement between the surrogate model predictions and the CSM simulations: A) very high, B) high, C) moderate, and D) low agreement. The heatmaps illustrate the spatial distribution in the ascending aorta mapped into a topologically equivalent rectangle. The y-axis corresponds to the circumferential direction, with BC and SC denoting the big and small curvatures, respectively, while the x-axis corresponds to the axial direction.

For stress predictions, across all agreement levels the estimated and reference results exhibit similar spatial distributions. In particular, cases A and B also present a close match in magnitude. Cases C and D show an overestimation of stress magnitudes compared with the reference values. The predictions of the first principal strain follow the same trend, with the overestimation in cases C and D appearing even more pronounced.

6.3.2.2 Case 2 – Patient-specific geometries

The performance of the surrogate model was also evaluated using the set of patient-specific anatomies employed in the PCA analysis. Figs. 6.6 and 6.7 illustrate the comparison between surrogate model predictions and reference CSM results for the first principal stress and strain, respectively. These figures follow the same rationale as in Case 1, including both the performance overview and the surface representation analysis.

For the patient-specific geometry dataset, the success rates for high agreement changed notably: 51% and 64% for the predictions of the second Piola-Kirchhoff stress and right Cauchy-Green deformation tensors, respectively. Nonetheless, the success rates for moderate agreement remained similar (95% and 97%, respectively). As with the PCA-driven cases, the DNN predicted spatial distributions follow the same qualitative patterns as the CSM simulations. However, more pronounced differences in the magnitude of the variables are observed in regions of reduced mechanical loading.

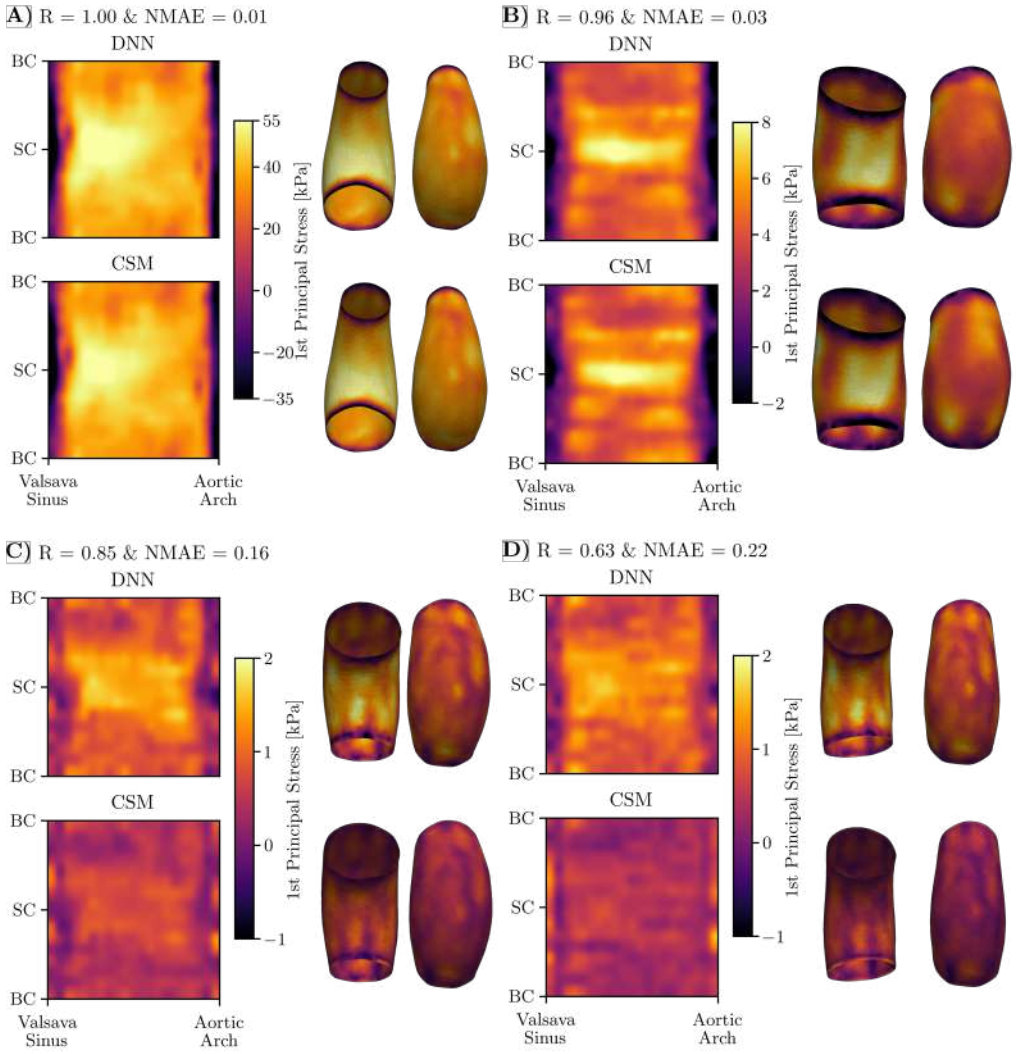

Figure 6.4: Surface representation of the surrogate and CSM model predictions of the first principal stress.

6.3.3 Correlation between error and inputs

Figure 6.8 examines how the prediction error of the surrogate model varies with different input parameters. The most noticeable trend is observed for the instantaneous pressure: as the pressure increases, the prediction error decreases significantly. For the remaining variables, including the PCA shape modes, wall thickness, and Young's modulus, no clear or consistent relationship with the error can be identified.

6.4 Discussion regarding the applicability of surrogate models

The work presented in this chapter introduced a surrogate modelling framework for predicting the mechanical response of ATAA. By combining SSM, CSM simulations, and DNNs, we developed a tool capable of reproducing the spatial distribution of the second Piola-Kirchhoff and right Cauchy-Green tensors with good agreement to reference

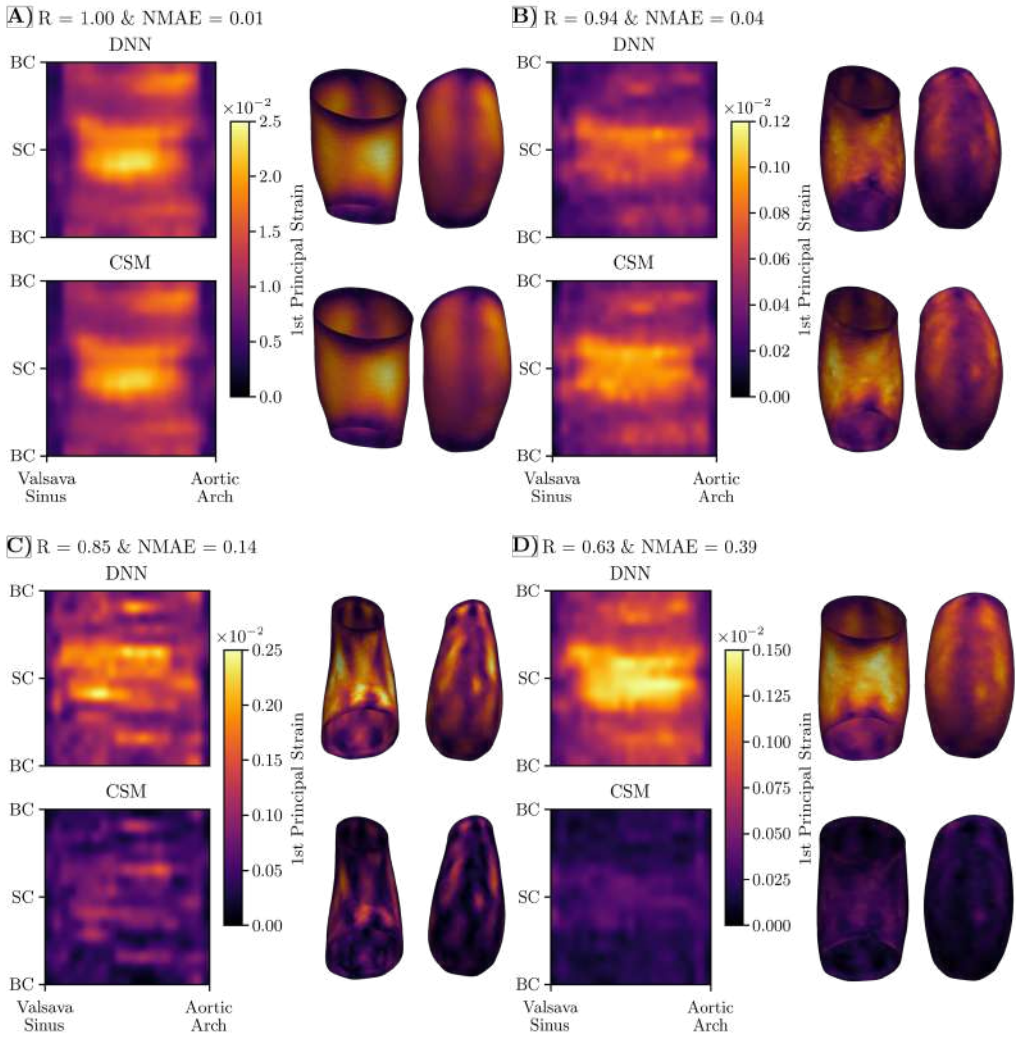

Figure 6.5: Surface representation of the surrogate and CSM model predictions of the first principal strain.

simulations. The model showed robust generalization across the input space, with its main sensitivity being associated with the loading conditions. In particular, prediction accuracy improved at higher instantaneous pressures, indicating that the surrogate performs more reliably under high loading conditions, such as peak systolic pressure.

One of the most relevant outcomes of this study is the gain in reporting time. While the reference CSM simulations required between 20–60 minutes to complete on a high-performance workstation, the surrogate model generated results in less than one second on a low-end computer. This substantial reduction in computational demand highlights the clinical potential of such approaches, where time-efficient tools are essential. The computational burden is transferred almost entirely to the training stage, enabling fast simulations once the model is trained. Nonetheless, a limitation of this strategy is the need for retraining whenever significant changes are introduced, such as new input features. Retraining the surrogate model may also require performing new simulations, for instance

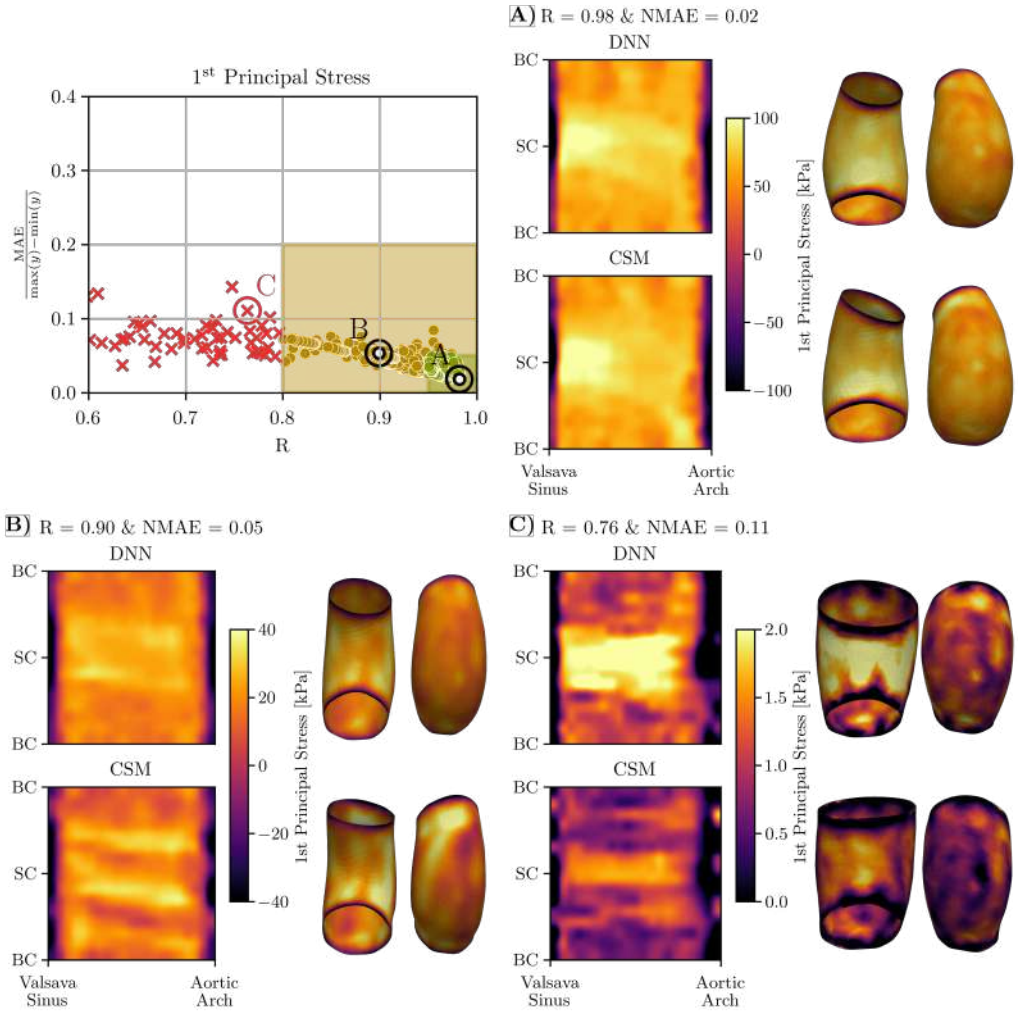

Figure 6.6: Surface representation of the surrogate and CSM model predictions of the first principal stress for the patient-specific anatomy dataset.

if boundary conditions are altered.

The performance analysis also revealed a decrease in success rate when the surrogate was applied to patient-specific anatomies, when compared to PCA-driven geometries. This reduction underscores the importance of expanding the input space to better capture anatomical variability. As future work, training the model with a higher number of PCA modes (for instance, the first 25 modes, which describe 99% of the shape variability) may improve predictive performance for patient-specific cases. Although this study focused on the ascending aorta, the proposed methodology could be extended to the full aortic geometry. Achieving this goal will require the development of more efficient mesh morphing strategies, capable of handling the increased anatomical complexity.

One major limitation observed in the high-fidelity CSM simulations is the presence of boundary effects, manifested as localized stress concentrations at the inlet and outlet regions. These effects are likely induced by the imposed boundary conditions. While such artifacts are confined to the boundaries and do not affect the main region of interest

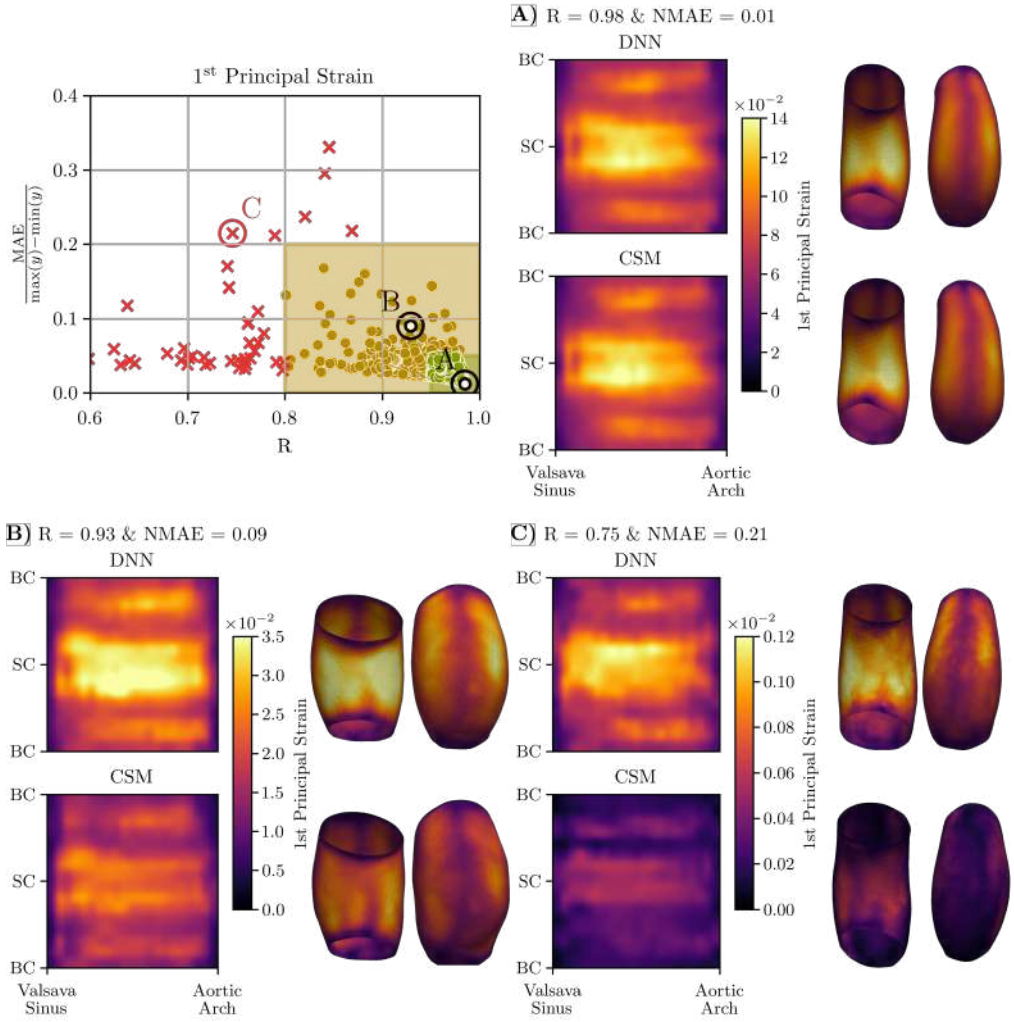

Figure 6.7: Surface representation of the surrogate and CSM model predictions of the first principal strain for the patient-specific anatomy dataset.

in the ascending aorta, they highlight the importance of carefully designing boundary conditions to avoid unrealistic stress distributions. Extending the computational domain or testing alternative boundary conditions could help mitigate these artifacts.

Additional improvements can also be made in the constitutive description of the aortic wall. The present framework assumes a homogeneous wall with constant thickness and material properties. More physiologically realistic descriptions, such as spatially varying thickness, heterogeneous material properties, and histo-mechanical constitutive models, would better capture the underlying biomechanics. Incorporating these features, together with numerical validation, will be key steps towards building clinically reliable digital twins of aortic aneurysms. Future work may also include in training the effects of hypertension and hypotension.

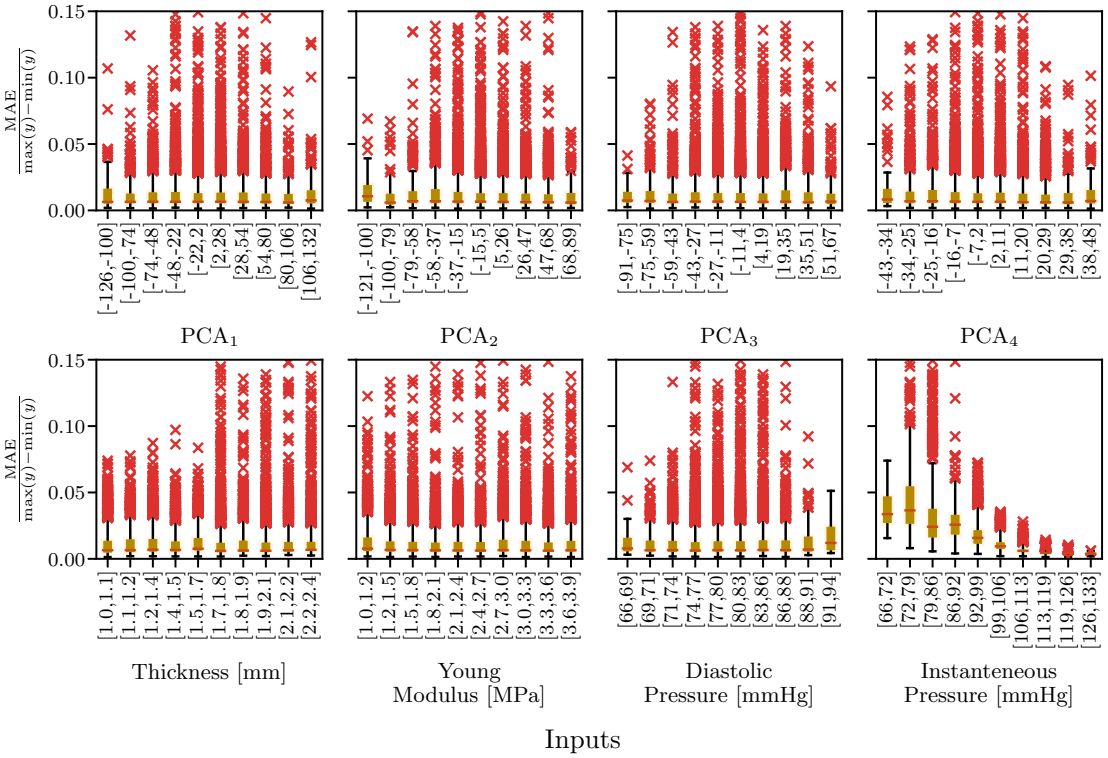

Figure 6.8: Correlation between the NMAE of the model predictions and the input parameters.

6.5 Main remarks

One of the main bottlenecks limiting the introduction of numerical models of ATAA biomechanics is the long computational time required for patient-specific analyses. Deep learning architectures trained on numerical simulation data offer a promising approach to overcome this limitation, as demonstrated in the present work. In this chapter, a surrogate model of ATAA wall mechanics was proposed, combining a SSM, DNN, and CSM simulations. The surrogate model was able to reproduce the spatial distributions of the second Piola-Kirchhoff and right Cauchy-Green tensors across almost the entire test dataset. For the patient-specific geometries, more than 95% of the predictions reached at least moderate agreement, confirming the robustness of the approach. Overall, this chapter demonstrates the feasibility and impact of using data-driven surrogate modelling to accelerate patient-specific biomechanical analyses, representing a significant step toward clinical translation.

Chapter 7

Conclusions

The work presented in this PhD thesis focused on studying the application of different numerical approaches to model the biomechanics of Ascending Thoracic Aortic Aneurysms (ATAAs), aiming to find the techniques that yield the optimal trade-off between numerical accuracy and reporting time. This rationale comes under the context of reducing the reporting time in order to facilitate the introduction into clinical practices of computational frameworks.

The extensive bibliographic review regarding the numerical modelling of healthy and diseased aortas highlighted that: (i) numerical modelling represent a reliable tool to recreate patient-specific biomechanics of cardiovascular systems; (ii) Finite Element Method (FEM) and Finite Volume Method (FVM) are the most commonly used numerical approaches; and (iii) Fluid-Structure Interaction (FSI) is the gold standard technique to model the biomechanics of ATAA. Additionally, a critical analysis of the articles evidenced that the lack of implementation of patient-specific computational frameworks in current clinical guidelines is mainly due to the challenges regarding the adaption of these frameworks to *in vivo* conditions, modelling all the relevant physiological phenomenons, the high reporting time which is not suited for time-sensitive situations, and the lack of extensive validation against large patient cohorts.

Using different tissue prestressing methodologies to perform patient-specific FSI simulations of ATAA significantly impacted the numerical results of WSS and wall mechanics. Using the Prestress Tensor (PT) algorithm originated a stiffer mechanical response of the aortic wall than when using the Zero Pressure Geometry (ZPG) approach. This occurred due to the fact that the PT algorithm does not consider the deformation between the reference and image configurations. The proposed methodology to define a regional mapping of calibrated material properties in combination with the PT improved the agreement with ZPG regarding the predictions of maximum principal stress and maximum principal

strain.

Resorting to FSI frameworks to simulate the biomechanics of ATAA requires extensive reporting time which may render them impractical for current clinical practices. Coupling Computational Solid Mechanics (CSM) and Reduced Order Model (ROM) recreates a 1-way FSI framework and represents a time-efficient alternative to estimate the biomechanics of ATAA. This computational framework may assist the development of robust tools to accurately stratify the risk of rupture of ATAA at the time of the medical imaging acquisitions. However, in situations where the Wall Shear Stress (WSS) are relevant, such as for modelling the growth and remodelling of the aortic wall, FSI is the most suitable approach. Resorting to Artificial Intelligence (AI) based tools may represent a promising solution to reduce the computational cost of FSI analysis. Although generating a suitable database of FSI simulation data to train the AI model is computationally expensive, this cost is "pulled back" entirely to the training stage.

Tools based on AI architectures stands out as a highly promising to be applied the entire workflow of numerical modelling of ATAAs, from geometry characterization to numerical results post-processing. Within the simulation stage AI demonstrates capability to reduce reporting times while maintaining a high level of accuracy. In this work,a Deep Neural Network (DNN)-based surrogate model of aortic structural mechanics was developed. The model relied on statistical shape analysis to extract global shape features and used CSM simulations to generate the training dataset. The performance showed strong agreement with the reference simulations, with more than 93 % of the test samples achieving a Pearson correlation coefficient greater than 0.8 and a normalized mean absolute error below 0.2. These results suggest that the proposed framework provides a time-efficient alternative to conventional simulations and holds potential for translation into clinical practice.

This thesis has some limitations that open opportunities for further developments. From the structural mechanics perspective, the aortic wall was modelled with homogeneous material properties and uniform thickness, whereas in reality it exhibits local variations in microstructure that lead to heterogeneous and anisotropic behaviour. In addition, the Neo-Hookean constitutive model, while numerically efficient and able to capture the hyperelastic response of the wall, in particular within the physiological pressure range, cannot fully reproduce the complexity of vascular tissue mechanics. Future extensions of this work could incorporate patient-specific material properties and wall thickness, as well as more advanced constitutive models, such as the Holzapfel-Gasser-Ogden formulation. Regarding the hemodynamic simulations, an idealized parabolic velocity profile was prescribed at the inlet. Although this is a reasonable assumption, it does not fully capture patient-specific inflow conditions. In future works, more realistic inlet boundary conditions should be implemented and automatic calibration methods should be developed for the outlet conditions.

The numerical analysis was also limited to a relatively small patient cohort, which may affect the generalizability of the findings, in particular for the Chapters 4 and 5. Most

importantly, the numerical results were not validated against experimental or in vivo data, which represents a key step for strengthening the reliability of the developed models. Future work should therefore focus on validation efforts.

References

[1] J. M. Lourenço. *The NOVAthesis LaTeX Template User's Manual*. NOVA University Lisbon. 2021. URL: https://github.com/joaomlourenco/novathesis/raw/main/template.pdf (cit. on p. i).

[2] W. H. Organization. *Cardiovascular diseases*. https://www.who.int/news-room/fact-sheets/detail/cardiovascular-diseases-(cvds) [Accessed: 08/03/2024]. 2021 (cit. on p. 2).

[3] K. H. Chau and J. A. Elefteriades. "Natural history of thoracic aortic aneurysms: size matters, plus moving beyond size". In: *Progress in cardiovascular diseases* 56.1 (2013), pp. 74–80. DOI: 10.1016/j.pcad.2013.05.007 (cit. on p. 2).

[4] G. A. Kuzmik, A. X. Sang, and J. A. Elefteriades. "Natural history of thoracic aortic aneurysms". In: *Journal of vascular surgery* 56.2 (2012), pp. 565–571. DOI: 10.1016/j.jvs.2012.04.053 (cit. on p. 2).

[5] J. A. Beckman and W. C. Members. "2022 ACC/AHA Guideline for the Diagnosis and Management of Aortic Disease: A Report of the American Heart Association/American College of Cardiology Joint Committee on Clinical Practice Guidelines". In: *Circulation* 146.24 (2022), e334–e482. DOI: 10.1161/CIR.0000000000001106 (cit. on p. 2).

[6] A. Mathur et al. "Aortic aneurysm". In: *Journal of translational internal medicine* 4.1 (2016), pp. 35–41. DOI: 10.1515/jtim-2016-0008 (cit. on p. 2).

[7] R. Erbel et al. "2014 ESC Guidelines on the diagnosis and treatment of aortic diseases: document covering acute and chronic aortic diseases of the thoracic and abdominal aorta of the adult The Task Force for the Diagnosis and Treatment of Aortic Diseases of the European Society of Cardiology (ESC)". In: *Eur. Heart J.* 35.41 (2014), pp. 2873–2926. DOI: 10.1093/eurheartj/ehu281 (cit. on pp. 2, 22, 32).

[8] L. F. Hiratzka et al. "2010 ACCF / AHA / AATS / ACR / ASA / SCA / SCAI / SIR / STS / SVM guidelines for the diagnosis and management of patients with thoracic aortic disease". In: *J. Am. Coll. Cardiol.* 55.14 (2010), e27–e129. DOI: 10.1161/CIR.0b013e3181d4739e (cit. on pp. 2, 22).

[9] J. Rozado et al. "Comparing American, European and Asian practice guidelines for aortic diseases". In: *Journal of thoracic disease* 9.Suppl 6 (2017), S551. DOI: 10.21037/jtd.2017.03.97 (cit. on p. 2).

[10] S. Shelmerdine, J. Barber, and C. George. "Applications of Laplace's law in clinical medicine: A radiological pictorial review". In: *British Journal of Hospital Medicine (2005)* 74.8 (2013), pp. 451–456. DOI: 10.12968/hmed.2013.74.8.451 (cit. on p. 2).

[11] B. P. Adriaans et al. "Predictive imaging for thoracic aortic dissection and rupture: moving beyond diameters". In: *European radiology* 29.12 (2019), pp. 6396–6404. DOI: 10.1007/s00330-019-06320-7 (cit. on p. 2).

[12] S. Trimarchi et al. "Descending aortic diameter of 5.5 cm or greater is not an accurate predictor of acute type B aortic dissection". In: *The Journal of thoracic and cardiovascular surgery* 142.3 (2011), e101–e107. DOI: 10.1016/j.jtcvs.2010.12.032 (cit. on p. 2).

[13] H. I. Michelena et al. "Incidence of aortic complications in patients with bicuspid aortic valves". In: *Jama* 306.10 (2011), pp. 1104–1112. DOI: 10.1001/jama.2011.1286 (cit. on p. 2).

[14] M. Lucio et al. "On the importance of tunica intima in the aging aorta: a three-layered in silico model for computing wall stresses in abdominal aortic aneurysms". In: *Comput. Methods Biomech. Biomed. Eng.* 24.5 (2021), pp. 467–484. DOI: 10.1080/10255842.2020.1836167 (cit. on pp. 2, 11, 17, 21, 44, 153).

[15] R. Jayendiran et al. "Computational prediction of hemodynamical and biomechanical alterations induced by aneurysm dilatation in patient-specific ascending thoracic aortas". In: *Int. J. Numer. Method. Biomed. Eng.* 36.6 (2020), e3326. DOI: 10.1002/cnm.3326 (cit. on pp. 2, 17).

[16] J Rueckel et al. "Artificial intelligence assistance improves reporting efficiency of thoracic aortic aneurysm CT follow-up". In: *European Journal of Radiology* 134 (2021), p. 109424. DOI: 10.1016/j.ejrad.2020.109424 (cit. on pp. 2, 32, 41).

[17] K. Capellini et al. "Computational fluid dynamic study for aTAA hemodynamics: an integrated image-based and radial basis functions mesh morphing approach". In: *J. Biomech. Eng.* 140.11 (2018), pp. 1–10. DOI: 10.1115/1.4040940 (cit. on pp. 3, 30, 31, 45, 47, 75, 153).

[18] F Condemi et al. "Fluid-and biomechanical analysis of ascending thoracic aorta aneurysm with concomitant aortic insufficiency". In: *Ann. Biomed. Eng.* 45.12 (2017), pp. 2921–2932. DOI: 10.1007/s10439-017-1913-6 (cit. on pp. 3, 14, 16, 42, 47, 57, 75, 79, 150).

[19] S. Pasta et al. "Shear stress and aortic strain associations with biomarkers of ascending thoracic aortic aneurysm". In: *Ann. Thorac. Surg.* 110.5 (2020), pp. 1595–1604. DOI: 10.1016/j.athoracsur.2020.03.017 (cit. on pp. 3, 14, 17, 40–42, 47, 149).

[20] J. Corral-Acero et al. "The 'Digital Twin'to enable the vision of precision cardiology". In: *Eur. Heart J.* 41.48 (2020), pp. 4556–4564. DOI: 10.1093/eurheartj/ehaa159 (cit. on pp. 3, 27).

[21] Y. Zhang et al. "A pilot study exploring the mechanisms involved in the longitudinal propagation of acute aortic dissection through computational fluid dynamic analysis". In: *Cardiology* 128.2 (2014), pp. 220–225. DOI: 10.1159/000358041 (cit. on pp. 3, 31, 33, 36, 47, 144).

[22] H. H. Yeh, S. W. Rabkin, and D. Grecov. "Hemodynamic assessments of the ascending thoracic aortic aneurysm using fluid-structure interaction approach". In: *Med. Biol. Eng. Comput.* 56.3 (2018), pp. 435–451. DOI: 10.1007/s11517-017-1693-z (cit. on pp. 3, 35, 47, 141).

[23] T. C. Gasser. *Vascular Biomechanics: Concepts, Models, and Applications*. Springer Cham, 2021. DOI: 10.1007/978-3-030-70966-2 (cit. on pp. 9, 18, 20).

[24] J. E. Hall and M. E. Hall. *Guyton and Hall textbook of medical physiology*. Elsevier Health Sciences, 2020. ISBN: 978-0-323-59712-8 (cit. on pp. 9, 16).

[25] O. K. Baskurt, M. R. Hardeman, and M. W. Rampling. *Handbook of hemorheology and hemodynamics*. Vol. 69. IOS press, 2007. ISBN: 978-1-58603-771-0 (cit. on pp. 9, 13).

[26] M. Thiriet. *Biology and mechanics of blood flows: Part II: Mechanics and medical aspects*. Springer Science & Business Media, 2007. DOI: 10.1007/978-0-387-74847-4 (cit. on p. 9).

[27] L. Prahl Wittberg et al. "Effects of aortic irregularities on blood flow". In: *Biomech. Model. Mechanobiol.* 15.2 (2016), pp. 345–360. DOI: 10.1007/s10237-015-0692-y (cit. on pp. 11, 15, 35, 142).

[28] M. Bopp et al. "A computational and experimental study of physiological pulsatile flow in an aortic aneurysm". In: *11th International Symposium on Turbulence and Shear Flow Phenomena, Southampton, United Kingdom*. 30 July 2019 (cit. on pp. 11, 40, 41, 149).

[29] A. J. Peacock, R. Naeije, and L. J. Rubin. *Pulmonary circulation*. Hodder Arnold, 2016. ISBN: 978-1-4987-1994-0 (cit. on p. 11).

[30] S. Standring et al. "Gray's anatomy: the anatomical basis of clinical practice". In: *American journal of neuroradiology* 26.10 (2005), p. 2703 (cit. on p. 11).

[31] J. S. Wilson, W. R. Taylor, and J. Oshinski. "Assessment of the regional distribution of normalized circumferential strain in the thoracic and abdominal aorta using DENSE cardiovascular magnetic resonance". In: *Journal of Cardiovascular Magnetic Resonance* 21.1 (2019), pp. 1–14. DOI: 10.1186/s12968-019-0565-0 (cit. on p. 11).

[32] O. Gültekin et al. "Computational modeling of progressive damage and rupture in fibrous biological tissues: application to aortic dissection". In: *Biomech. Model. Mechanobiol.* 18.6 (2019), pp. 1607–1628. DOI: 10.1007/s10237-019-01164-y (cit. on pp. 11, 17, 27, 38, 47, 147).

[33] M. Ben-Or Frank et al. "Micromechanically-motivated analysis of fibrous tissue". In: *J. Mech. Behav. Biomed. Mater.* 96 (2019), pp. 69–78. DOI: 10.1016/j.jmbbm.2019.04.007 (cit. on pp. 11, 31, 45, 147).

[34] G. A. Holzapfel, T. C. Gasser, and R. W. Ogden. "A new constitutive framework for arterial wall mechanics and a comparative study of material models". In: *Journal of elasticity and the physical science of solids* 61 (2000), pp. 1–48. DOI: 10.1023/A:1010835316564 (cit. on p. 11).

[35] J. E. Wagenseil et al. "Reduced vessel elasticity alters cardiovascular structure and function in newborn mice". In: *Circulation research* 104.10 (2009), pp. 1217–1224. DOI: 10.1161/CIRCRESAHA.108.192054 (cit. on p. 11).

[36] G. G. Belz. "Elastic properties and Windkessel function of the human aorta". In: *Cardiovascular Drugs and Therapy* 9.1 (1995), pp. 73–83. DOI: 10.1007/BF00877747 (cit. on p. 12).

[37] H. Bader. "Importance of the gerontology of elastic arteries in the development of essential hypertension". In: *Clinical physiology and biochemistry* 1.1 (1983), pp. 36–56 (cit. on p. 12).

[38] G. S. Kassab. "Biomechanics of the cardiovascular system: the aorta as an illustratory example". In: *J. R. Soc. Interface* 3.11 (2006), pp. 719–740. DOI: 10.1098/rsif.2006.0138 (cit. on p. 12).

[39] R. Valente et al. "CFD Model of the Ascending Thoracic Aortic Aneurysms with Patient Wall Deformation". In: *Congress of the Portuguese Society of Biomechanics*. Springer. 2023, pp. 69–77. DOI: 10.1007/978-3-031-47790-4_7 (cit. on pp. 12, 14).

[40] K. Calò et al. "Impact of wall displacements on the large-scale flow coherence in ascending aorta". In: *J. Biomech.* 154 (2023), p. 111620. DOI: 10.1016/j.jbiomech.2023.111620 (cit. on pp. 12, 75, 88).

[41] O. K. Baskurt and H. J. Meiselman. "Blood rheology and hemodynamics". In: *Seminars in thrombosis and hemostasis*. Vol. 29. 05. 2003. DOI: 10.1055/s-2003-44551 (cit. on pp. 12, 13).

[42] A. N. Beris et al. "Recent advances in blood rheology: A review". In: *Soft Matter* 17.47 (2021), pp. 10591–10613. DOI: 10.1039/D1SM01212F (cit. on pp. 12, 13, 15).

[43] A. S. Popel and P. C. Johnson. "Microcirculation and hemorheology". In: *Annu. Rev. Fluid Mech.* 37 (2005), pp. 43–69. DOI: 10.1146/annurev.fluid.37.042604.133933 (cit. on pp. 12, 13).

[44] L. H. Pugholm et al. "Phenotyping of leukocytes and leukocyte-derived extracellular vesicles". In: *Journal of immunology research* 2016 (2016). DOI: 10.1155/2016/6391264 (cit. on p. 12).

[45] A Marossy et al. "Hemorheology and circulation". In: *Clinical hemorheology and microcirculation* 42.4 (2009), pp. 239–258. DOI: 10.3233/CH-2009-1192 (cit. on p. 13).

[46] M. Eppihimer and H. Lipowsky. "Effects of leukocyte-capillary plugging on the resistance to flow in the microvasculature of cremaster muscle for normal and activated leukocytes". In: *Microvascular research* 51.2 (1996), pp. 187–201. DOI: 10.1006/mvre.1996.002 (cit. on p. 13).

[47] R. F. Tuma, W. N. Durán, and K. Ley. *Microcirculation*. Vol. 4. Academic Press, 2011. ISBN: 978-0-12-374530-9 (cit. on p. 13).

[48] C. G. Ellis, J. Jagger, and M. Sharpe. "The microcirculation as a functional system". In: *Critical care* 9 (2005), pp. 1–6. DOI: 10.1186/cc3751 (cit. on p. 13).

[49] S. Chien. "Biophysical behavior of red cells in suspensions". In: *The red blood cell*. Vol. 2. New York: Academic Press, Inc, 1975. Chap. 26, pp. 1031–1133. ISBN: 0-12-677202-9 (cit. on p. 13).

[50] C. Bachmann et al. "Fluid dynamics of a pediatric ventricular assist device". In: *Artificial Organs* 24.5 (2000), pp. 362–372. DOI: 10.1046/j.1525-1594.2000.06536.x (cit. on p. 13).

[51] M. G. Al-Azawy, A Turan, and A. Revell. "Investigating the impact of non-Newtonian blood models within a heart pump". In: *Int. J. Numer. Method. Biomed. Eng.* 33.1 (2017), e02780. DOI: 10.1002/cnm.2780 (cit. on p. 13).

[52] R. Valente et al. "Fluid-Structure Interaction Modeling of Ascending Thoracic Aortic Aneurysms in SimVascular". In: *Biomechanics* 2.2 (2022), pp. 189–204. DOI: 10.3390/biomechanics2020016 (cit. on pp. 14, 16, 21, 30, 45, 53, 57, 80, 152).

[53] A. Mariotti et al. "Hemodynamics and stresses in numerical simulations of the thoracic aorta: Stochastic sensitivity analysis to inlet flow-rate waveform". In: *Comput. Fluids* 230 (2021), pp. 173–182. DOI: 10.1016/j.compfluid.2021.105123 (cit. on pp. 14, 30, 47, 58, 75, 79, 93, 152).

[54] U. Hackstein, S. Krickl, and S. Bernhard. "Estimation of ARMA-model parameters to describe pathological conditions in cardiovascular system models". In: *Inf. Med. Unlocked* 18 (2020), pp. 1–8. DOI: 10.1016/j.imu.2020.100310 (cit. on pp. 14, 46, 57, 79, 152).

[55] C. Arico et al. "Numerical Simulations of the Hydrodynamics of the Abdominal Aorta Aneurysm (AAA) Using a Smoothed Particle Hydrodynamics Code with Deformable Wall Preliminary Results". In: *4th IEEE International Forum on Research and Technologies for Society and Industry, Palermo, Italy*. 10 September 2018. DOI: 10.1109/RTSI.2018.8548389 (cit. on pp. 14, 32, 46, 49, 153).

[56] A. Totorean et al. "Medical IMAGE-Based Numerical Simulation of the Abdominal Aorta Flow". In: *10th International Conference on Energy and Environment, Bucharest, Romania*. 14 October 2021. DOI: 10.1109/CIEM52821.2021.9614874 (cit. on pp. 14, 34, 57, 75, 79, 140).

[57] J. K. Long Ko et al. "Pulsatile hemodynamics in patient-specific thoracic aortic dissection models constructed from computed tomography angiography". In: *J. X-Ray Sci. Technol.* 25.2 (2017), pp. 233–245. DOI: 10.3233/XST-17256 (cit. on pp. 14, 33, 36, 47, 75, 141).

[58] S. Numata et al. "Blood flow analysis of the aortic arch using computational fluid dynamics". In: *Eur. J. Cardiothorac. Surg.* 49.6 (2016), pp. 1578–1585. DOI: 10.1093/ejcts/ezv459 (cit. on pp. 14, 35, 42, 47, 142).

[59] H. Wei, A. L. Cheng, and N. M. Pahlevan. "On the significance of blood flow shear-rate-dependency in modeling of Fontan hemodynamics". In: *European Journal of Mechanics-B/Fluids* 84 (2020), pp. 1–14. DOI: 10.1016/j.euromechflu.2020.05.011 (cit. on pp. 14, 15).

[60] A Mourato et al. "On the RANS modelling of the patient-specific thoracic aortic aneurysm". In: *9th Portuguese Congress on Biomechanics, Biomechanics, Porto, Portugal*. CRC Press, 19-20 February 2021, pp. 98–102. ISBN: 978-1-032-10806-3 (cit. on pp. 14–16, 44, 48, 152).

[61] B. Šeta, M. Torlak, and A. Vila. "Numerical simulation of blood flow through the aortic arch". In: vol. 62. 16 March 2017, pp. 259–268. DOI: 10.1007/978-981-10-4166-2_39 (cit. on pp. 14, 33, 141).

[62] T. Gasser, M. Auer, and J. Biasetti. "Structural and hemodynamical analysis of aortic aneurysms from computerized tomography angiography data". In: 7 September 2009, pp. 1584–1587. DOI: 10.1007/978-3-642-03882-2_420 (cit. on pp. 14, 33, 34, 145).

[63] M. E. Biancolini et al. "Fast interactive CFD evaluation of hemodynamics assisted by RBF mesh morphing and reduced order models: the case of aTAA modelling". In: *Int. J. Interact. Des. Manuf.* 14.4 (2020), pp. 1227–1238. DOI: 10.1007/s12008-020-00694-5 (cit. on pp. 14, 32, 46–48, 75, 152).

[64] M. Alimohammadi et al. "Aortic dissection simulation models for clinical support: fluid-structure interaction vs. rigid wall models". In: *Biomed. Eng. Online* 14.1 (2015), pp. 1–16. DOI: 10.1186/s12938-015-0032-6 (cit. on pp. 14, 43, 44, 48, 154).

[65] M. Silva et al. "Comparative Study of Rheological Models for Pulsatile Blood Flow in Realistic Aortic Arch Aneurysm Geometry by Numerical Computer Simulation". In: *Brazilian Congress on Biomedical Engineering*. Springer. 2020, pp. 37–42. DOI: 10.1007/978-3-030-70601-2_6 (cit. on pp. 14, 15).

[66] R. Campobasso et al. "Evaluation of peak wall stress in an ascending thoracic aortic aneurysm using FSI simulations: effects of aortic stiffness and peripheral resistance". In: *Cardiovasc. Eng. Technol.* 9.4 (2018), pp. 707–722. DOI: 10.1007/s13239-018-00385-z (cit. on pp. 14, 33, 35, 140).

[67] M. Nowak et al. "The protocol for using elastic wall model in modeling blood flow within human artery". In: *Eur. J. Mech. B. Fluids* 77 (2019), pp. 273–280. DOI: 10.1016/j.euromechflu.2019.03.009 (cit. on pp. 14, 31, 43, 48, 153).

[68] C. Del Gaudio, U. Morbiducci, and M. Grigioni. "Time dependent non-Newtonian numerical study of the flow field in a realistic model aortic arch". In: *Int. J. Artif. Organs* 29.7 (2006), pp. 709–718. DOI: 10.1177/039139880602900711 (cit. on pp. 15, 33, 145).

[69] M. Alishahi, M. Alishahi, and H. Emdad. "Numerical simulation of blood flow in a flexible stenosed abdominal real aorta". In: *Sci. Iran.* 18.6 (2011), pp. 1297–1305. DOI: 10.1016/j.scient.2011.11.021 (cit. on pp. 15, 33, 144).

[70] S. N. Sedeh et al. "Investigation of non-Newtonian blood flow with power-law model: Effects of coronary congenital heart defect on a specific age type". In: *ZAMM-Journal of Applied Mathematics and Mechanics/Zeitschrift für Angewandte Mathematik und Mechanik* (2021), e202000298. DOI: 10.1002/zamm.202000298 (cit. on p. 15).

[71] A. Caballero and S Laín. "Numerical simulation of non-Newtonian blood flow dynamics in human thoracic aorta". In: *Comput. Method. Biomec.* 18.11 (2015), pp. 1200–1216. DOI: 10.1080/10255842.2014.887698 (cit. on p. 15).

[72] J. V. Soulis et al. "Non-Newtonian models for molecular viscosity and wall shear stress in a 3D reconstructed human left coronary artery". In: *Med. Eng. Phys.* 30.1 (2008), pp. 9–19. DOI: 10.1016/j.medengphy.2007.02.001 (cit. on p. 15).

[73] A. A. Soares et al. "Computational fluid dynamics in abdominal aorta bifurcation: non-Newtonian versus Newtonian blood flow in a real case study". In: *Comput. Method. Biomec.* 20.8 (2017), pp. 822–831. DOI: 10.1080/10255842.2017.1302433 (cit. on p. 15).

[74] M. Jahangiri, M. Saghafian, and M. R. Sadeghi. "Effect of six non-Newtonian viscosity models on hemodynamic parameters of pulsatile blood flow in stenosed artery". In: *Journal of Computational & Applied Research in Mechanical Engineering (JCARME)* 7.2 (2018), pp. 199–207. DOI: 10.22061/jcarme.2017.1433.1114 (cit. on p. 15).

[75] L Goubergrits, E Wellnhofer, and U Kertzscher. "Choice and impact of a non-Newtonian blood model for wall shear stress profiling of coronary arteries". In: *14th Nordic-Baltic Conference on Biomedical Engineering and Medical Physics, Riga, Latvia*. 16 June 2008. DOI: 10.1080/10255842.2017.1302433 (cit. on p. 15).

[76] Z Cheng et al. "Analysis of flow patterns in a patient-specific aortic dissection model". In: *J. Biomech. Eng.* 132 (2010). DOI: 10.1115/1.4000964 (cit. on pp. 15, 35, 144).

[77] M. H. Mansour, N. W. Bressloff, and C. P. Shearman. "Red blood cell migration in microvessels". In: *Biorheology* 47.1 (2010), pp. 73–93. DOI: 10.3233/BIR-2010-0560 (cit. on p. 15).

[78] M. M. Molla and M. Paul. "LES of non-Newtonian physiological blood flow in a model of arterial stenosis". In: *Med. Eng. Phys.* 34.8 (2012), pp. 1079–1087. DOI: 10.1016/j.medengphy.2011.11.013 (cit. on p. 15).

[79] K. Bäumler et al. "Fluid–structure interaction simulations of patient-specific aortic dissection". In: *Biomech. Model. Mechanobiol.* 19.5 (2020), pp. 1607–1628. DOI: 10.1007/s10237-020-01294-8 (cit. on pp. 15, 29, 43, 53, 57, 58, 79, 80, 96, 152).

[80] J Febina, M. Y. Sikkandar, and N. Sudharsan. "Wall shear stress estimation of thoracic aortic aneurysm using computational fluid dynamics". In: *Comput. Math. Methods Med.* 2018 (2018). DOI: 10.1155/2018/7126532 (cit. on pp. 15, 27, 44, 47, 154).

[81] K. Khanafer et al. "Turbulence Significantly Increases Pressure and Fluid Shear Stress in an Aortic Aneurysm Model under Resting and Exercise Flow Conditions". In: *Ann. Vasc. Surg.* 21.1 (2007), pp. 67–74. DOI: 10.1016/j.avsg.2006.10.009 (cit. on pp. 15, 44, 156).

[82] K. J. Davies. "Adaptive homeostasis". In: *Molecular aspects of medicine* 49 (2016), pp. 1–7. DOI: 10.1016/j.mam.2016.04.007 (cit. on p. 15).

[83] T. C. Gasser. "Modeling the structural and mechanical properties of the normal and aneurysmatic aortic wall". In: *Multi-scale Extracellular Matrix Mechanics and Mechanobiology*. Cham: Springer International Publishing, 2020, pp. 55–82. ISBN: 978-3-030-20182-1. DOI: 10.1007/978-3-030-20182-1_3 (cit. on p. 16).

[84] J. G. Betts et al. "Anatomy and physiology. OpenStax". In: *Rice University: Houston, TX, USA* (2013) (cit. on p. 16).

[85] P. Youssefi et al. "Patient-specific computational fluid dynamics—assessment of aortic hemodynamics in a spectrum of aortic valve pathologies". In: *The Journal of thoracic and cardiovascular surgery* 153.1 (2017), pp. 8–20. DOI: 10.1016/j.jtcvs.2016.09.040 (cit. on p. 16).

[86] T. A. Hope et al. "Comparison of flow patterns in ascending aortic aneurysms and volunteers using four-dimensional magnetic resonance velocity mapping". In: *Journal of Magnetic Resonance Imaging: An Official Journal of the International Society for Magnetic Resonance in Medicine* 26.6 (2007), pp. 1471–1479. DOI: 10.1002/jmri.21082 (cit. on pp. 16, 23).

[87] X. Liu et al. "Physiological significance of helical flow in the arterial system and its potential clinical applications". In: *Ann. Biomed. Eng.* 43 (2015), pp. 3–15. DOI: 10.1007/s10439-014-1097-2 (cit. on p. 16).

[88] G. De Nisco et al. "The atheroprotective nature of helical flow in coronary arteries". In: *Ann. Biomed. Eng.* 47 (2019), pp. 425–438. DOI: 10.1007/s10439-018-02169-x (cit. on p. 16).

[89] O. A. Jarral et al. "Phase-contrast magnetic resonance imaging and computational fluid dynamics assessment of thoracic aorta blood flow: a literature review". In: *European Journal of Cardio-Thoracic Surgery* 57.3 (2020), pp. 438–446. DOI: 10.1093/ejcts/ezz280 (cit. on p. 16).

[90] H. Ha et al. "Age-related vascular changes affect turbulence in aortic blood flow". In: *Front. Physiol.* 9 (2018), p. 310199. DOI: 10.3389/fphys.2018.00036 (cit. on p. 16).

[91] C. W. Ong et al. "Computational fluid dynamics modeling of hemodynamic parameters in the human diseased aorta: A systematic review". In: *Annals of Vascular Surgery* 63 (2020), pp. 336–381. DOI: 10.1016/j.avsg.2019.04.032 (cit. on p. 16).

[92] C. Vergara et al. "Large eddy simulations of blood dynamics in abdominal aortic aneurysms". In: *Med. Eng. Phys.* 47 (2017), pp. 38–46. DOI: 10.1016/j.medengphy.2017.06.030 (cit. on p. 16).

[93] A. Postnov et al. "Thoracic aortic aneurysm: blood pressure and inflammation as key factors in the development of aneurysm dissection". In: *Current Pharmaceutical Design* 27.28 (2021), pp. 3122–3127. DOI: 10.2174/1381612827666210210142200 (cit. on p. 17).

[94] T. Hatakeyama, H. Shigematsu, and T. Muto. "Risk factors for rupture of abdominal aortic aneurysm based on three-dimensional study". In: *Journal of Vascular Surgery* 33.3 (2001), pp. 453–461. DOI: 10.1067/mva.2001.111731 (cit. on p. 17).

[95] E. Kobeissi et al. "Blood pressure, hypertension and the risk of abdominal aortic aneurysms: a systematic review and meta-analysis of cohort studies". In: *European journal of epidemiology* 34 (2019), pp. 547–555. DOI: 10.1007/s10654-019-00510-9 (cit. on p. 17).

[96] S. J. Mousavi et al. "Coupling hemodynamics with mechanobiology in patient-specific computational models of ascending thoracic aortic aneurysms". In: *Comput. Methods Programs Biomed.* 205 (2021), p. 106107. DOI: 10.1016/j.cmpb.2021.106107 (cit. on pp. 17, 65, 87).

[97] J. M. Ruddy et al. "Regional heterogeneity within the aorta: Relevance to aneurysm disease". In: *The Journal of Thoracic and Cardiovascular Surgery* 136.5 (2008-11), 1123–1130. ISSN: 0022-5223. DOI: 10.1016/j.jtcvs.2008.06.027. URL: http://dx.doi.org/10.1016/j.jtcvs.2008.06.027 (cit. on p. 17).

[98] J. Concannon et al. "Quantification of the regional bioarchitecture in the human aorta". In: *Journal of Anatomy* 236.1 (2019-09), 142–155. ISSN: 1469-7580. DOI: 10.1111/joa.13076. URL: http://dx.doi.org/10.1111/joa.13076 (cit. on p. 18).

[99] R Wang et al. "Effect of Glycation on Interlamellar Bonding of Arterial Elastin". In: *Exp. Mech.* 61.1 (2021), pp. 81–94. DOI: 10.1007/s11340-020-00644-y (cit. on pp. 18, 38, 47).

[100] H. Weisbecker et al. "The role of elastin and collagen in the softening behavior of the human thoracic aortic media". In: *Journal of Biomechanics* 46.11 (2013-07), 1859–1865. ISSN: 0021-9290. DOI: 10.1016/j.jbiomech.2013.04.025. URL: http://dx.doi.org/10.1016/j.jbiomech.2013.04.025 (cit. on pp. 19, 20).

[101] J. Shi et al. "Metabolism of vascular smooth muscle cells in vascular diseases". In: *American Journal of Physiology-Heart and Circulatory Physiology* 319.3 (2020-09), H613–H631. ISSN: 1522-1539. DOI: 10.1152/ajpheart.00220.2020. URL: http://dx.doi.org/10.1152/ajpheart.00220.2020 (cit. on p. 18).

[102] G. L. Basatemur et al. "Vascular smooth muscle cells in atherosclerosis". In: *Nature Reviews Cardiology* 16.12 (2019-06), 727–744. ISSN: 1759-5010. DOI: 10.1038/s41569-019-0227-9. URL: http://dx.doi.org/10.1038/s41569-019-0227-9 (cit. on p. 19).

[103] D. M. Milewicz et al. "Genetic variants promoting smooth muscle cell proliferation can result in diffuse and diverse vascular diseases: Evidence for a hyperplastic vasculomyopathy". In: *Genetics in Medicine* 12.4 (2010-04), 196–203. ISSN: 1098-3600. DOI: 10.1097/gim.0b013e3181cdd687. URL: http://dx.doi.org/10.1097/GIM.0b013e3181cdd687 (cit. on p. 19).

[104] N. Gundiah, A. R. Babu, and L. A. Pruitt. "Effects of elastase and collagenase on the nonlinearity and anisotropy of porcine aorta". In: *Physiological Measurement* 34.12 (2013), 1657–1673. ISSN: 1361-6579. DOI: 10.1088/0967-3334/34/12/1657. URL: http://dx.doi.org/10.1088/0967-3334/34/12/1657 (cit. on p. 19).

[105] A. J. Schriefl et al. "Selective enzymatic removal of elastin and collagen from human abdominal aortas: Uniaxial mechanical response and constitutive modeling". In: *Acta Biomaterialia* 17 (2015), pp. 125–136. ISSN: 1742-7061. DOI: https://doi.org/10.1016/j.actbio.2015.01.003. URL: https://www.sciencedirect.com/science/article/pii/S1742706115000045 (cit. on p. 19).

[106] A. V. Kamenskiy et al. "Biaxial mechanical properties of the human thoracic and abdominal aorta, common carotid, subclavian, renal and common iliac arteries". In: *Biomechanics and Modeling in Mechanobiology* 13.6 (2014-04), 1341–1359. ISSN: 1617-7940. DOI: 10.1007/s10237-014-0576-6. URL: http://dx.doi.org/10.1007/s10237-014-0576-6 (cit. on p. 20).

[107] G. Franchini et al. "Viscoelastic characterization of human descending thoracic aortas under cyclic load". In: *Acta Biomaterialia* 130 (2021), 291–307. ISSN: 1742-7061. DOI: 10.1016/j.actbio.2021.05.025. URL: http://dx.doi.org/10.1016/j.actbio.2021.05.025 (cit. on p. 19).

[108] A. Avanzini et al. "Biomechanical Evaluation of Ascending Aortic Aneurysms". In: *BioMed Research International* 2014 (2014), 1–9. ISSN: 2314-6141. DOI: 10.1155/2014/820385. URL: http://dx.doi.org/10.1155/2014/820385 (cit. on p. 20).

[109] A. Mourato et al. "On the Importance of Modelling the Interplay Between the Blood Flow and the Aortic Wall in Ascending Thoracic Aortic Aneurysms". In: *Congress of the Portuguese Society of Biomechanics*. Springer. 2023, pp. 233–243. DOI: 10.1007/978-3-031-47790-4_22 (cit. on p. 21).

[110] K. Matthys et al. "Pulse wave propagation in a model human arterial network: Assessment of 1-D numerical simulations against in vitro measurements". In: *J. Biomech.* 40.15 (2007), pp. 3476–3486. DOI: 10.1016/j.jbiomech.2007.05.027 (cit. on pp. 21, 46, 75, 156).

[111] A. Owen. "A numerical model of the aorta and aortic valve". In: *18th Annual Conference on Computers in Cardiology, Venice, Italy*. 23 September 1992, pp. 649–652 (cit. on pp. 21, 29, 46, 157).

[112] E. Bollache et al. "Numerical modeling of arterial pulse wave propagation to characterize aortic hemodynamic: Validation using magnetic resonance data". In: *Innovation Res. Biomed. Eng.* 34.1 (2013), pp. 86–89. DOI: 10.1016/j.irbm.2012.12.008 (cit. on pp. 21, 32, 46, 155).

[113] W. Wolański et al. "Numerical analysis of blood flow through artery with elastic wall of a vessel". In: *Innovations in Biomedical Engineering*. Ed. by M. Gzik et al. Vol. 526. Springer: Cham, Switzerland, 2017, pp. 193–200. DOI: 10.1007/978-3-319-47154-9_23 (cit. on pp. 21, 27, 43, 47, 154).

[114] J. Bols et al. "Unstructured hexahedral mesh generation of complex vascular trees using a multi-block grid-based approach". In: *Comput. Methods Biomech. Biomed. Eng.* 19.6 (2016), pp. 663–672. DOI: 10.1080/10255842.2015.1058925 (cit. on pp. 21, 30, 45, 48, 75, 93, 154).

[115] C. García–Herrera, D. Celentano, and E. Herrera. "Modelling and numerical simulation of the in vivo mechanical response of the ascending aortic aneurysm in Marfan syndrome". In: *Med. Biol. Eng. Comput.* 55.3 (2017), pp. 419–428. DOI: 10.1007/s11517-016-1524-7 (cit. on pp. 21, 35, 53, 75, 141).

[116] F. Riveros et al. "A Pull-Back Algorithm to Determine the Unloaded Vascular Geometry in Anisotropic Hyperelastic AAA Passive Mechanics". In: *Annals of Biomedical Engineering* 41.4 (2012-11), 694–708. ISSN: 1573-9686. DOI: 10.1007/s10439-012-0712-3. URL: http://dx.doi.org/10.1007/s10439-012-0712-3 (cit. on p. 21).

[117] S. Polzer et al. "Importance of material model in wall stress prediction in abdominal aortic aneurysms". In: *Medical Engineering Physics* 35.9 (2013-09), 1282–1289. ISSN: 1350-4533. DOI: 10.1016/j.medengphy.2013.01.008. URL: http://dx.doi.org/10.1016/j.medengphy.2013.01.008 (cit. on p. 21).

[118] G. A. Holzapfel, T. C. Gasser, and R. W. Ogden. "Comparison of a Multi-Layer Structural Model for Arterial Walls With a Fung-Type Model, and Issues of Material Stability". In: *Journal of Biomechanical Engineering* 126.2 (2004-04), 264–275. ISSN: 1528-8951. DOI: 10.1115/1.1695572. URL: http://dx.doi.org/10.1115/1.1695572 (cit. on p. 21).

[119] E. Ban, C. Cavinato, and J. D. Humphrey. "Differential propensity of dissection along the aorta". In: *Biomech. Model. Mechanobiol.* 20.3 (2021), pp. 895–907. DOI: 10.1007/s10237-021-01418-8 (cit. on pp. 21, 38, 146).

[120] A. N. Azadani et al. "Comparison of mechanical properties of human ascending aorta and aortic sinuses". In: *Ann. Thorac. Surg.* 93.1 (2012), pp. 87–94. DOI: 110.1016/j.athoracsur.2011.08.002 (cit. on pp. 21, 39, 42, 47, 148).

[121] C. Babbs. "Noninvasive measurement of cardiac stroke volume using pulse wave velocity and aortic dimensions: A simulation study". In: *Biomed. Eng. Online* 13 (2014), pp. 1–25. DOI: 10.1186/1475-925X-13-137 (cit. on pp. 21, 40, 151).

[122] L. Liang et al. "A machine learning approach as a surrogate of finite element analysis-based inverse method to estimate the zero-pressure geometry of human thoracic aorta". In: *Int. J. Numer. Method. Biomed. Eng.* 34.8 (2018), e3103. DOI: 10.1002/cnm.3103 (cit. on pp. 21, 30, 32, 45, 47, 49, 53, 89, 154).

[123] V. Mendez, M. Di Giuseppe, and S. Pasta. "Comparison of hemodynamic and structural indices of ascending thoracic aortic aneurysm as predicted by 2-way FSI, CFD rigid wall simulation and patient-specific displacement-based FEA". In: *Comput. Biol. Med.* 100 (2018), pp. 221–229. DOI: 10.1016/j.compbiomed.2018.07.013 (cit. on pp. 21, 27, 43, 48, 88, 93, 154).

[124] M. Liu et al. "Computation of a probabilistic and anisotropic failure metric on the aortic wall using a machine learning-based surrogate model". In: *Comput. Biol. Med.* 137 (2021), p. 104794. DOI: 10.1016/j.compbiomed.2021.104794 (cit. on pp. 21, 41, 42, 149).

[125] H. Taghizadeh, M. Tafazzoli-Shadpour, and M. B. Shadmehr. "Analysis of arterial wall remodeling in hypertension based on lamellar modeling". In: *J. Am. Soc. Hypertens.* 9.9 (2015), pp. 735–744. DOI: 10.1016/j.jash.2015.07.014 (cit. on pp. 21, 31, 38, 147).

[126] W. Wang et al. "Numerical Simulation of Instantaneous Wave-Free Ratio of Stenosed Coronary Artery". In: *Int. J. Comput. Methods* 16 (2019), pp. 1–9. DOI: 10.1142/S0219876218420094 (cit. on pp. 21, 146).

[127] G. Comunale et al. "Numerical models can assist choice of an aortic phantom for in vitro testing". In: *Bioengineering* 8.8 (2021), pp. 1–14. DOI: 10.3390/bioengineering8080101 (cit. on pp. 21, 30, 37, 47, 57, 79, 146).

[128] T. C. Gasser, R. W. Ogden, and G. A. Holzapfel. "Hyperelastic modelling of arterial layers with distributed collagen fibre orientations". In: *J. R. Soc. Interface* 3.6 (2006), pp. 15–35. DOI: 10.1098/rsif.2005.0073 (cit. on pp. 21, 58).

[129] M.-C. Hsu and Y. Bazilevs. "Blood vessel tissue prestress modeling for vascular fluid–structure interaction simulation". In: 47.6 (), pp. 593–599. DOI: 10.1016/j.finel.2010.12.015 (cit. on pp. 22, 53, 62, 63, 96).

[130] M. Raghavan, B. Ma, and M. F. Fillinger. "Non-invasive determination of zero-pressure geometry of arterial aneurysms". In: *Ann. Biomed. Eng.* 34 (2006), pp. 1414–1419. DOI: 10.1002/cnm.3663 (cit. on pp. 22, 53, 61).

[131] H. Weisbecker, D. M. Pierce, and G. A. Holzapfel. "A generalized prestressing algorithm for finite element simulations of preloaded geometries with application to the aorta". In: *Int. J. Numer. Method. Biomed. Eng.* 30.9 (2014), pp. 857–872. DOI: 10.1002/cnm.2632 (cit. on p. 22).

[132] R. Gouveia e Melo et al. "Incidence and Prevalence of Thoracic Aortic Aneurysms: A Systematic Review and Meta-analysis of Population-Based Studies". In: *Seminars in Thoracic and Cardiovascular Surgery* 34.1 (2022), pp. 1–16. ISSN: 1043-0679. DOI: 10.1053/j.semtcvs.2021.02.029 (cit. on p. 22).

[133] G. A. Kuzmik, A. X. Sang, and J. A. Elefteriades. "Natural history of thoracic aortic aneurysms". In: *Journal of Vascular Surgery* 56.2 (2012), pp. 565–571. ISSN: 0741-5214. DOI: 10.1016/j.jvs.2012.04.053 (cit. on p. 22).

[134] D. Laukka et al. "Prevalence of thoracic aortic aneurysms and dilatations in patients with intracranial aneurysms". In: *Journal of Vascular Surgery* 70.6 (2019), pp. 1801–1808. ISSN: 0741-5214. DOI: 10.1016/j.jvs.2019.01.066 (cit. on p. 22).

[135] G. Martufi et al. "Is There a Role for Biomechanical Engineering in Helping to Elucidate the Risk Profile of the Thoracic Aorta?" In: *The Annals of Thoracic Surgery* 101.1 (2016), pp. 390–398. ISSN: 0003-4975. DOI: 10.1016/j.athoracsur.2015.07.028 (cit. on p. 22).

[136] L. A. Pape et al. "Aortic diameter > or = 5.5 cm is not a good predictor of type A aortic dissection: Observations from the International Registry of Acute Aortic Dissection (IRAD)". In: *Circulation* 116.10 (2007), 1120 – 1127. DOI: 10.1161/CIRCULATIONAHA.107.702720 (cit. on p. 22).

[137] G. Coorey et al. "The health digital twin: advancing precision cardiovascular medicine". In: *Nat. Rev. Cardiol.* 18.12 (2021), pp. 803–804. DOI: 10.1038/s41569-021-00630-4 (cit. on p. 27).

[138] J. R. Thunes et al. "Structural modeling reveals microstructure-strength relationship for human ascending thoracic aorta". In: *J. Biomech.* 71 (2018), pp. 84–93. DOI: 10.1016/j.jbiomech.2018.01.037 (cit. on pp. 27, 30, 38, 43, 48, 147).

[139] W. Chen et al. "Direct numerical simulation of pulsatile flow in pipes". In: *19th Australasian Fluid Mechanics Conference, Melbourne, Australia*. 8 December 2014 (cit. on pp. 27, 30, 44, 48, 155).

[140] M. J. Page et al. "The PRISMA 2020 statement: an updated guideline for reporting systematic reviews". In: *Br. Med. J.* 372 (2021), pp. 1–11. DOI: 10.1186/s13643-021-01626-4 (cit. on p. 27).

[141] H. J. Schünemann et al. "Grading quality of evidence and strength of recommendations for diagnostic tests and strategies". In: *Br. Med. J.* 336.7653 (2008), pp. 1106–1110. DOI: 10.1136/bmj.39500.677199.AE (cit. on p. 28).

[142] G. H. Guyatt et al. "What is "quality of evidence" and why is it important to clinicians?" In: *Br. Med. J.* 336.7651 (2008), pp. 995–998. DOI: 10.1136/bmj.39490.551019.BE (cit. on p. 28).

[143] Z. Lou and W.-J. Yang. "A computer simulation of the non-Newtonian blood flow at the aortic bifurcation". In: *J. Biomech.* 26.1 (1993), pp. 37–49. DOI: 10.1016/0021-9290(93)90611-H (cit. on pp. 29, 31, 44).

[144] M. Žáček and E. Krause. "Numerical simulation of the blood flow in the human cardiovascular system". In: *J. Biomech.* 29.1 (1996), pp. 13–20. DOI: 10.1016/0021-9290(95)00027-5 (cit. on p. 29).

[145] D. Molony et al. "Fluid–Structure Interaction in Healthy, Diseased and Endovascularly Treated Abdominal Aortic Aneurysms". In: *Biomechanics and Mechanobiology of Aneurysms*. Ed. by T. McGloughlin. Vol. 7. Springer: Cham, Switzerland, 2011, pp. 163–179. DOI: 10.1007/8415_2011_85 (cit. on pp. 29, 31, 34, 144).

[146] B. Doyle et al. "On the influence of patient-specific material properties in computational simulations: A case study of a large ruptured abdominal aortic aneurysm". In: *Int. J. Numer. Method. Biomed. Eng.* 29.2 (2013), pp. 150–164. DOI: 10.1002/cnm.2515 (cit. on pp. 29, 44, 155).

[147] F. Carneiro et al. "Numerical study of blood fluid rheology in the abdominal aorta". In: *WIT Trans. Ecol. Environ.* 114 (2008), pp. 169–178. DOI: 10.2495/DN080181 (cit. on pp. 29, 44, 48, 156).

[148] F. Helderman et al. "A numerical model to predict abdominal aortic aneurysm expansion based on local wall stress and stiffness". In: *Med. Biol. Eng. Comput.* 46.11 (2008), pp. 1121–1127. DOI: 10.1007/s11517-008-0358-3 (cit. on pp. 29, 38, 148).

[149] Y. Shi et al. "The risk of stanford type-A aortic dissection with different tear size and location: A numerical study". In: *Biomed. Eng. Online* 15 (2016), pp. 531–544. DOI: 10.1186/s12938-016-0258-y (cit. on pp. 29, 33, 36, 141).

[150] L. Taelman et al. "Fluid-structure interaction simulation of pulse propagation in arteries: Numerical pitfalls and hemodynamic impact of a local stiffening". In: *Int. J. Eng. Sci.* 77 (2014), pp. 1–13. DOI: 10.1016/j.ijengsci.2013.12.002 (cit. on pp. 30, 46, 47, 154).

[151] E. K. Shang et al. "Peak wall stress predicts expansion rate in descending thoracic aortic aneurysms". In: *Ann. Thorac. Surg.* 95.2 (2013), pp. 593–598. DOI: 10.1016/j.athoracsur.2012.10.025 (cit. on pp. 31, 40, 41, 144, 151).

[152] G. D. Nisco et al. "What is needed to make low-density lipoprotein transport in human aorta computational models suitable to explore links to atherosclerosis? Impact of initial and inflow boundary conditions". In: *J. Biomech.* 68 (2018), pp. 33–42. DOI: 10.1016/j.jbiomech.2017.12.009 (cit. on pp. 31, 47, 153).

[153] S. Pasta et al. "Difference in hemodynamic and wall stress of ascending thoracic aortic aneurysms with bicuspid and tricuspid aortic valve". In: *J. Biomech.* 46.10 (2013), pp. 1729–1738. DOI: 10.1016/j.jbiomech.2013.03.029 (cit. on pp. 31, 34, 47, 58, 80, 96, 143).

[154] J. Sotelo et al. "3D axial and circumferential wall shear stress from 4D flow MRI data using a finite element method and a laplacian approach". In: *Magn. Reson. Med.* 79.5 (2018), pp. 2816–2823. DOI: 10.1002/mrm.26927 (cit. on pp. 31, 41, 47, 150).

[155] J. Sotelo et al. "Quantification of wall shear stress using a finite-element method in multidimensional phase-contrast MR data of the thoracic aorta". In: *J. Biomech.* 48.10 (2015), pp. 1817–1827. DOI: 10.1016/j.jbiomech.2015.04.038 (cit. on pp. 31, 41, 57, 79, 150).

[156] H. Suito, T. Ueda, and D. Sze. "Numerical simulation of blood flow in the thoracic aorta using a centerline-fitted finite difference approach". In: 30.3 (2013), pp. 701–710. DOI: 10.1007/s13160-013-0123-3 (cit. on pp. 31, 45, 48, 75, 143, 155).

[157] F. He and X.-Y. Li. "Selection of boundary conditions in numerical investigation of arterial flow". In: *3rd International Conference on Bioinformatics and Biomedical Engineering, Beijing, China*. 11 June 2009. DOI: 10.1109/ICBBE.2009.5163374 (cit. on pp. 31, 46, 47, 156).

[158] J. Brunet, B. Pierrat, and P. Badel. "A Parametric Study on Factors Influencing the Onset and Propagation of Aortic Dissection Using the Extended Finite Element Method". In: *IEEE Trans. Biomed. Eng* 68.10 (2021), pp. 2918–2929. DOI: 10.1109/TBME.2021.3056022 (cit. on pp. 31, 36, 38, 75, 140).

[159] T. Fukui and K. Morinishi. "Blood flow simulation in the aorta with aortic valves using the regularized lattice boltzmann method with LES model". In: vol. 129. 10 April 2013, pp. 97–107. DOI: 10.2495/FSI130091 (cit. on pp. 32, 33, 143).

[160] Y. Aboelkassem, D. Savic, and S. Campbell. "Mathematical modeling of aortic valve dynamics during systole". In: *J. Theor. Biol.* 365 (2015), pp. 280–288. DOI: 10.1016/j.jtbi.2014.10.027 (cit. on pp. 32, 45, 155).

[161] A. Geertsema et al. "Development of a numerical simulation model of the cardiovascular system". In: *Artif. Organs* 21.12 (1997), pp. 1297–1301. DOI: 10.1111/j.1525-1594.1997.tb00492.x (cit. on pp. 32, 46, 49, 156).

[162] I. Sazonov et al. "A novel method for non-invasively detecting the severity and location of aortic aneurysms". In: *Biomech. Model. Mechanobiol.* 16.4 (2017), pp. 1225–1242. DOI: 10.1007/s10237-017-0884-8 (cit. on pp. 32, 40, 75, 150).

[163] N. Kizilova and J. Mizerski. "Validation of numerical models for flow simulation and wave propagation a human aorta". In: vol. 1101. 9 September 2018. DOI: 10.1088/1742-6596/1101/1/012014 (cit. on pp. 32, 40, 149).

[164] Y. Chen and H. Luo. "Pressure distribution over the leaflets and effect of bending stiffness on fluid-structure interaction of the aortic valve". In: *J. Fluid Mech.* 883 (2019), pp. 1–29. DOI: 10.1017/jfm.2019.904 (cit. on pp. 32, 34, 46, 49, 140).

[165] M. Liu, L. Liang, and W. Sun. "A generic physics-informed neural network-based constitutive model for soft biological tissues". In: *Comput. Methods Appl. Mech. Eng.* 372 (2020), p. 113402. DOI: 10.1016/j.cma.2020.113402 (cit. on pp. 32, 45).

[166] X. He, S. Avril, and J. Lu. "Prediction of local strength of ascending thoracic aortic aneurysms". In: *J. Mech. Behav. Biomed. Mater.* 115 (2021), p. 104284. DOI: 10.1016/j.jmbbm.2020.104284 (cit. on pp. 32, 42).

[167] X. He, S. Avril, and J. Lu. "Estimating aortic thoracic aneurysm rupture risk using tension-strain data in physiological pressure range: an in vitro study". In: *Biomech. Model. Mechanobiol.* 20.2 (2021), pp. 683–699. DOI: 10.1007/s10237-020-01410-8 (cit. on pp. 32, 42).

[168] Y. Luo et al. "Machine learning-aided exploration of relationship between strength and elastic properties in ascending thoracic aneurysm". In: *Int. J. Numer. Method. Biomed. Eng.* 34.6 (2018), e2977. DOI: 10.1002/cnm.2977 (cit. on pp. 32, 42).

[169] C. Aricò et al. "Investigation of the hemodynamic flow conditions and blood-induced stresses inside an abdominal aortic aneurysm by means of a SPH numerical model". In: *Int. J. Numer. Method. Biomed. Eng.* 36 (2020), pp. 1–6. DOI: 10.1002/cnm.3263 (cit. on pp. 32, 46, 49, 153).

[170] J. Silva et al. "Numerical simulation of aneurysms with Finite Element and meshless methods". In: 23 February 2019. DOI: 10.1109/ENBENG.2019.8692459 (cit. on pp. 32, 45, 49, 153).

[171] Y. Cong, L. Wang, and X. Liu. "A numerical study of fluid-structure coupled effect of abdominal aortic aneurysm". In: *Bio-Med. Mater. Eng.* 26 (2015), S245–S255. DOI: 10.3233/BME-151311 (cit. on pp. 33, 34, 143).

[172] G. Jalalahmadi, C. Linte, and M. Helguera. "A numerical framework for studying the biomechanical behavior of abdominal aortic aneurysm". In: vol. 10137. 12 February 2017. DOI: 10.1117/12.2254528 (cit. on pp. 33, 35, 75, 141).

[173] F. Callaghan et al. "Thoracic aortic aneurysm: 4D flow MRI and computational fluid dynamics model". In: *Comput. Method. Biomech. Biomed. Engin.* 18.Suppl 1 (2015), pp. 1894–1895 (cit. on pp. 33, 34, 58, 79, 142).

[174] K. Chaudhari and H. Patel. "Hemodynamics numerical simulation of stenosis bifurcation". In: vol. 3-2015. 13 November 2015. DOI: 10.1115/IMECE2015-51072 (cit. on pp. 33, 142).

[175] Z. Keshavarz-Motamed and L. Kadem. "3D pulsatile flow in a curved tube with coexisting model of aortic stenosis and coarctation of the aorta". In: *Med. Eng. Phys.* 33.3 (2011), pp. 315–324. DOI: 10.1016/j.medengphy.2010.10.017 (cit. on pp. 33, 75, 145).

[176] B. Melka et al. "Numerical investigation of multiphase blood flow coupled with lumped parameter model of outflow". In: *Int. J. Numer. Methods Heat Fluid Flow* 30.1 (2020), pp. 228–244. DOI: 10.1108/HFF-04-2019-0279 (cit. on pp. 33, 140).

[177] J. Lantz, J. Renner, and M. Karlsson. "Wall shear stress in a subject specific human aorta - Influence of fluid-structure interaction". In: *Int. J. Appl. Mech.* 3.4 (2011), pp. 759–778. DOI: 10.1142/S1758825111001226 (cit. on pp. 33, 43, 48, 75, 93, 144).

[178] G. Marom et al. "Fully coupled fluid-structure interaction model of congenital bicuspid aortic valves: Effect of asymmetry on hemodynamics". In: *Med. Biol. Eng. Comput.* 51.8 (2013), pp. 839–848. DOI: 10.1007/s11517-013-1055-4 (cit. on pp. 33, 143, 155).

[179] M.-H. Moosavi et al. "Numerical simulation of blood flow in the left ventricle and aortic sinus using magnetic resonance imaging and computational fluid dynamics". In: *Comput. Methods Biomech. Biomed. Eng.* 17.7 (2014), pp. 740–749. DOI: 10.1080/10255842.2012.715638 (cit. on pp. 33, 58, 79, 143).

[180] S. B. Ahmed, D Dillon-Murphy, and C. Figueroa. "Computational study of anatomical risk factors in idealized models of type B aortic dissection". In: *Eur. J. Vasc. Endovasc. Surg.* 52.6 (2016), pp. 736–745. DOI: 10.1016/j.ejvs.2016.07.025 (cit. on pp. 36, 58, 79, 142).

[181] W. N. Wan Ab Naim et al. "A perspective review on numerical simulations of hemodynamics in aortic dissection". In: *Sci. World J.* 2014 (2014), pp. 1–13. DOI: 10.1155/2014/652520 (cit. on pp. 36, 57, 79).

[182] H. Chen et al. "Editor's Choice–Fluid–Structure Interaction Simulations of Aortic Dissection with Bench Validation". In: *Eur. J. Vasc. Endovasc. Surg.* 52.5 (2016), pp. 589–595 (cit. on pp. 36, 58, 79, 142).

[183] A. Cloonan et al. "3D-printed tissue-mimicking phantoms for medical imaging and computational validation applications". In: *3D Print. Addit. Manuf.* 1.1 (2014), pp. 14–23. DOI: 10.1089/3dp.2013.0010 (cit. on pp. 37, 40, 148).

[184] J. R. Thunes et al. "A structural finite element model for lamellar unit of aortic media indicates heterogeneous stress field after collagen recruitment". In: *J. Biomech.* 49.9 (2016), pp. 1562–1569. DOI: 10.1016/j.jbiomech.2016.03.034 (cit. on pp. 38, 40, 147).

[185] S. Maiti et al. "Computational modeling of the strength of the ascending thoracic aortic media tissue under physiologic biaxial loading conditions". In: *J. Biomech.* 108 (2020), p. 109884. DOI: 10.1016/j.jbiomech.2020.109884 (cit. on pp. 38, 146).

[186] A.-S. Yang et al. "An innovative numerical approach to resolve the pulse wave velocity in a healthy thoracic aorta model". In: *Comput. Methods Biomech. Biomed. Eng.* 17.5 (2014), pp. 461–473. DOI: 10.1080/10255842.2012.691476 (cit. on pp. 39, 40, 75, 93, 148).

[187] M. Liu, L. Liang, and W. Sun. "Estimation of in vivo mechanical properties of the aortic wall: A multi-resolution direct search approach". In: *J. Mech. Behav. Biomed. Mater.* 77 (2018), pp. 649–659. DOI: 10.1016/j.jmbbm.2017.10.022 (cit. on pp. 39, 47, 49).

[188] M. Liu et al. "Identification of in vivo nonlinear anisotropic mechanical properties of ascending thoracic aortic aneurysm from patient-specific CT scans". In: *Sci. Rep.* 9.1 (2019), pp. 1–13. DOI: 10.1038/s41598-019-49438-w (cit. on pp. 39, 48).

[189] S. Farzaneh, O. Trabelsi, and S. Avril. "Inverse identification of local stiffness across ascending thoracic aortic aneurysms". In: *Biomech. Model. Mechanobiol.* 18.1 (2019), pp. 137–153. DOI: 10.1007/s10237-018-1073-0 (cit. on pp. 39, 58, 80, 96, 146).

[190] C. Zhu, J.-H. Seo, and R. Mittal. "Computational modelling and analysis of haemodynamics in a simple model of aortic stenosis". In: *J. Fluid Mech.* 851 (2018), pp. 23–49. DOI: 10.1017/jfm.2018.463 (cit. on pp. 40, 41, 44, 150).

[191] H. Mohammadi, R. Cartier, and R. Mongrain. "Derivation of a simplified relation for assessing aortic root pressure drop incorporating wall compliance". In: *Med. Biol. Eng. Comput.* 53.3 (2015), pp. 241–251. DOI: 10.1007/s11517-014-1228-9 (cit. on pp. 40, 150).

[192] V. Badeli et al. "Bayesian inference of multi-sensors impedance cardiography for detection of aortic dissection". In: *Int. J. Comput. Math. Electr. Electron. Eng.* 41 (2021), pp. 824–839. DOI: 10.1108/COMPEL-03-2021-0072 (cit. on pp. 40, 149).

[193] S Pasta et al. "In silico shear and intramural stresses are linked to aortic valve morphology in dilated ascending aorta". In: *Eur. J. Vasc. Endovasc. Surg.* 54.2 (2017), pp. 254–263. DOI: 10.1016/j.ejvs.2017.05.016 (cit. on pp. 40, 42, 150).

[194] A. Bauer et al. "Comparison of wall shear stress estimates obtained by laser Doppler velocimetry, magnetic resonance imaging and numerical simulations". In: *Exp. Fluids* 60 (2019), pp. 1–16. DOI: 10.1007/s00348-019-2758-6 (cit. on pp. 41, 57, 79, 149).

[195] B. Doyle et al. "An experimental and numerical comparison of the rupture locations of an abdominal aortic aneurysm". In: *J. Endovasc. Ther.* 16.3 (2009), pp. 322–335. DOI: 10.1583/09-2697.1 (cit. on pp. 41, 42, 151).

[196] G. Marom et al. "A fluid-structure interaction model of the aortic valve with coaptation and compliant aortic root". In: *Med. Biol. Eng. Comput.* 50.2 (2012), pp. 173–182. DOI: 10.1007/s11517-011-0849-5 (cit. on p. 43).

[197] R. Berguer, J. Bull, and K. Khanafer. "Refinements in mathematical models to predict aneurysm growth and rupture". In: *Ann. N. Y. Acad. Sci.* 1085 (2006), pp. 110–116. DOI: 10.1196/annals.1383.033 (cit. on pp. 44, 156).

[198] J. Lantz et al. "Numerical and experimental assessment of turbulent kinetic energy in an aortic coarctation". In: *J. Biomech.* 46.11 (2013), pp. 1851–1858. DOI: 10.1016/j.jbiomech.2013.04.028 (cit. on pp. 44, 48, 155).

[199] S. Stevens, W. Lakin, and W. Goetz. "A differentiable, periodic function for pulsatile cardiac output based on heart rate and stroke volume". In: *Math. Biosci.* 182.2 (2003), pp. 201–211. DOI: 10.1016/S0025-5564(02)00200-6 (cit. on p. 45).

[200] T. Koltukluoğlu and P. Blanco. "Boundary control in computational haemodynamics". In: *J. Fluid Mech.* 847 (2018), pp. 329–364. DOI: 10.1017/jfm.2018.329 (cit. on pp. 45, 48, 154).

[201] S. Attaran, H. Niroomand-oscuii, and F. Ghalichi. "A novel, simple 3D/2D outflow boundary model for blood flow simulations in compliant arteries". In: *Comput. Fluids* 174 (2018), pp. 229–240. DOI: 10.1016/j.compfluid.2018.08.006 (cit. on pp. 45, 58, 80, 96, 153).

[202] G. D. Santis et al. "Full-hexahedral structured meshing for image-based computational vascular modeling". In: *Med. Eng. Phys.* 33.10 (2011), pp. 1318–1325. DOI: 10.1016/j.medengphy.2011.06.007 (cit. on pp. 45, 48).

[203] F. Salvucci et al. "Assessment of pulsatile wall shear stress in compliant arteries: Numerical model, validation and experimental data". In: *31st Annual International Conference of the IEEE Engineering in Medicine and Biology Society: Engineering the Future of Biomedicine, Minneapolis, United States*. 2 September 2009, pp. 2847–2850. DOI: 10.1109/IEMBS.2009.5333648 (cit. on pp. 46, 49, 156).

[204] E. Bollache et al. "Descending aorta subject-specific one-dimensional model validated against in vivo data". In: *J. Biomech.* 47.2 (2014), pp. 424–431. DOI: 10.1016/j.jbiomech.2013.11.009 (cit. on pp. 46, 49, 155).

[205] A. Boccadifuoco et al. "Uncertainty quantification applied to hemodynamic simulations of thoracic aorta aneurysms: Sensitivity to inlet conditions". In: *Quantification of Uncertainty: Improving Efficiency and Technology*. Ed. by M. Elia, M. Gunzburger, and R. G. Springer: Cham, Switzerland, 2020, pp. 171–192. DOI: 10.1007/978-3-030-48721-8_8 (cit. on p. 47).

[206] M. Antonuccio et al. "Effects of the Distribution in Space of the Velocity-Inlet Condition in Hemodynamic Simulations of the Thoracic Aorta". In: 6 May 2020. DOI: 10.1007/978-3-030-45385-5_6 (cit. on p. 47).

[207] R. D. Johnston, M. Ghasemi, and C. Lally. "Inverse material parameter estimation of patient-specific finite element models at the carotid bifurcation: The impact of excluding the zero-pressure configuration and residual stress". In: *Int. J. Numer. Method. Biomed. Eng.* 39.1 (2022), e3663. DOI: 10.1002/cnm.3663 (cit. on p. 53).

[208] S. Parikh et al. "Biomechanical Characterisation of Thoracic Ascending Aorta with Preserved Pre-Stresses". In: *Bioengineering* 10.7 (2023). DOI: 10.3390/bioengineering10070846 (cit. on p. 53).

[209] T. Sasaki, K. Takizawa, and T. E. Tezduyar. "Medical-image-based aorta modeling with zero-stress-state estimation". In: *Comput. Mech.* 64 (2019), pp. 249–271. DOI: 10.1007/s00466-019-01669-4 (cit. on p. 53).

[210] M. W. Gee, C. Förster, and W. Wall. "A computational strategy for prestressing patient-specific biomechanical problems under finite deformation". In: *Int. J. Numer. Method. Biomed. Eng.* 26.1 (2010), pp. 52–72. DOI: 10.1002/cnm.1236 (cit. on p. 53).

[211] A. Updegrove et al. "SimVascular: an open source pipeline for cardiovascular simulation". In: *Ann. Biomed. Eng.* 45 (2017), pp. 525–541. DOI: 10.1007/s10439-016-1762-8 (cit. on pp. 53, 56, 57, 78, 95).

[212] R. Kikinis, S. D. Pieper, and K. G. Vosburgh. "3D Slicer: a platform for subject-specific image analysis, visualization, and clinical support". In: *Intraoperative imaging and image-guided therapy*. Springer, 2013, pp. 277–289 (cit. on pp. 56, 77).

[213] Y. Bazilevs et al. "Isogeometric fluid-structure interaction: theory, algorithms, and computations". In: *Comput. Mech.* 43.1 (2008), pp. 3–37. DOI: 10.1007/s00466-008-0315-x (cit. on pp. 57, 78).

[214] M. Selmi, H. Belmabrouk, and A. Bajahzar. "Numerical study of the blood flow in a deformable human aorta". In: *Appl. Sci.* 9.6 (2019), p. 1216. DOI: 10.3390/app9061216 (cit. on p. 58).

[215] I. E. Vignon-Clementel et al. "Outflow boundary conditions for three-dimensional finite element modeling of blood flow and pressure in arteries". In: *Comput. Methods Appl. Mech. Eng.* 195.29 (2006), pp. 3776–3796. DOI: 10.1016/j.cma.2005.04.014 (cit. on p. 59).

[216] D. P. Sokolis, H. Boudoulas, and P. E. Karayannacos. "Assessment of the aortic stress–strain relation in uniaxial tension". In: *J. Biomech.* 35.9 (2002), pp. 1213–1223. DOI: 10.1016/S0021-9290(02)00073-8 (cit. on p. 64).

[217] D. P. Sokolis. "Passive mechanical properties and structure of the aorta: segmental analysis". In: *Acta Physiol.* 190.4 (2007), pp. 277–289. DOI: 10.1111/j.1748-1716.2006.01661.x (cit. on p. 64).

[218] G. De Nisco et al. "Deciphering ascending thoracic aortic aneurysm hemodynamics in relation to biomechanical properties". In: *Med. Eng. Phys.* 82 (2020), pp. 119–129. DOI: 10.1016/j.medengphy.2020.07.003 (cit. on pp. 65, 87).

[219] A. Mourato et al. "Computational modelling and simulation of fluid structure interaction in aortic aneurysms: a systematic review and discussion of the clinical potential". In: *Appl. Sci.* 2.2 (2022), pp. 0–38204. DOI: 10.3390/app12168049 (cit. on p. 75).

[220] M. Hoeijmakers et al. "Combining statistical shape modeling, CFD, and meta-modeling to approximate the patient-specific pressure-drop across the aortic valve in real-time". In: *International journal for numerical methods in biomedical engineering* 36.10 (2020), e3387. DOI: 10.1002/cnm.3387 (cit. on p. 75).

[221] M. Bonfanti et al. "A simplified method to account for wall motion in patient-specific blood flow simulations of aortic dissection: Comparison with fluid-structure interaction". In: *Med. Eng. Phys.* 58 (2018), pp. 72–79. DOI: 10.1016/j.medengphy.2018.04.014 (cit. on p. 75).

[222] S. Epstein et al. "Reducing the number of parameters in 1D arterial blood flow modeling: less is more for patient-specific simulations". In: *American Journal of Physiology-Heart and Circulatory Physiology* 309.1 (2015), H222–H234. DOI: 10.1152/ajpheart.00857.2014 (cit. on p. 75).

[223] A. Ghavamian, S. J. Mousavi, and S. Avril. "Computational Study of Growth and Remodeling in Ascending Thoracic Aortic Aneurysms Considering Variations of Smooth Muscle Cell Basal Tone". In: *Frontiers in Bioengineering and Biotechnology* 8 (2020). DOI: 10.3389/fbioe.2020.587376 (cit. on p. 75).

[224] J. D. Laubrie, S. J. Mousavi, and S. Avril. "About prestretch in homogenized constrained mixture models simulating growth and remodeling in patient-specific aortic geometries". In: *Biomechanics and modeling in mechanobiology* 21.2 (2022), pp. 455–469. DOI: 10.1007/s10237-021-01544-3 (cit. on p. 75).

[225] S. J. Mousavi, S. Farzaneh, and S. Avril. "Patient-specific predictions of aneurysm growth and remodeling in the ascending thoracic aorta using the homogenized constrained mixture model". In: *Biomechanics and modeling in mechanobiology* 18 (2019), pp. 1895–1913. DOI: 10.1007/s10237-019-01184-8 (cit. on p. 75).

[226] T. J. Hughes and J. Lubliner. "On the one-dimensional theory of blood flow in the larger vessels". In: *Mathematical Biosciences* 18.1 (1973), pp. 161–170. ISSN: 0025-5564. DOI: 10.1016/0025-5564(73)90027-8 (cit. on p. 80).

[227] J. Frosen et al. "Flow-induced, inflammation-mediated arterial wall remodeling in the formation and progression of intracranial aneurysms". In: *Neurosurgical Focus FOC* 47.1 (2019). DOI: 10.3171/2019.5.FOCUS19234 (cit. on p. 87).

[228] L. Boussel et al. "Aneurysm Growth Occurs at Region of Low Wall Shear Stress". In: *Stroke* 39.11 (2008), pp. 2997–3002. DOI: 10.1161/STROKEAHA.108.521617 (cit. on p. 87).

[229] P. Reymond et al. "Physiological simulation of blood flow in the aorta: Comparison of hemodynamic indices as predicted by 3-D FSI, 3-D rigid wall and 1-D models". In: *Med. Eng. Phys.* 35.6 (2013), pp. 784–791. ISSN: 1350-4533. DOI: 10.1016/j.medengphy.2012.08.009 (cit. on p. 88).

[230] E. Soudah et al. "A reduced-order model based on the coupled 1D-3D finite element simulations for an efficient analysis of hemodynamics problems". In: *Computational Mechanics* 54 (2014), pp. 1013–1022. DOI: 10.1007/s00466-014-1040-2 (cit. on p. 88).

[231] W. Jin and J. Alastruey. "Arterial pulse wave propagation across stenoses and aneurysms: assessment of one-dimensional simulations against three-dimensional simulations and in vitro measurements". In: *Journal of the Royal Society Interface* 18.177 (2021), p. 20200881. DOI: 10.1098/rsif.2020.0881 (cit. on p. 88).

[232] M. Bonfanti et al. "A simplified method to account for wall motion in patient-specific blood flow simulations of aortic dissection: Comparison with fluid-structure interaction". In: *Medical Engineering & Physics* 58 (2018), pp. 72–79. ISSN: 1350-4533. DOI: 10.1016/j.medengphy.2018.04.014 (cit. on p. 88).

[233] M. Liu et al. "Computation of a probabilistic and anisotropic failure metric on the aortic wall using a machine learning-based surrogate model". In: *Computers in Biology and Medicine* 137 (2021), p. 104794. ISSN: 0010-4825. DOI: 10.1016/j.compbiomed.2021.104794 (cit. on p. 89).

[234] L. Liang, W. Mao, and W. Sun. "A feasibility study of deep learning for predicting hemodynamics of human thoracic aorta". In: *Journal of Biomechanics* 99 (2020), p. 109544. ISSN: 0021-9290. DOI: 10.1016/j.jbiomech.2019.109544 (cit. on p. 89).

[235] X. Tang and C. Wu. "A predictive surrogate model for hemodynamics and structural prediction in abdominal aorta for different physiological conditions". In: *Computer Methods and Programs in Biomedicine* 243 (2024), p. 107931. ISSN: 0169-2607. DOI: 10.1016/j.cmpb.2023.107931 (cit. on p. 89).

[236] R. Alizadeh, J. K. Allen, and F. Mistree. "Managing computational complexity using surrogate models: a critical review". In: *Research in Engineering Design* 31.3 (2020), pp. 275–298. DOI: 10.1007/s00163-020-00336-7 (cit. on p. 93).

[237] S. Donmazov et al. "Review of machine learning techniques in soft tissue biomechanics and biomaterials". In: *Cardiovascular Engineering and Technology* (2024), pp. 1–28. DOI: 10.1007/s13239-024-00737-y (cit. on p. 93).

[238] G. Su, L. Peng, and L. Hu. "A Gaussian process-based dynamic surrogate model for complex engineering structural reliability analysis". en. In: *Struct. Saf.* 68 (2017-09), pp. 97–109. DOI: 10.1016/j.strusafe.2017.06.003 (cit. on p. 93).

[239] T. Saida and M. Nishio. "Transfer learning Gaussian process regression surrogate model with explainability for structural reliability analysis under variation in uncertainties". en. In: *Comput. Struct.* 281.107014 (2023-06), p. 107014. DOI: 10.1016/j.compstruc.2023.107014 (cit. on p. 93).

[240] A. Hashemi, J. Jang, and J. Beheshti. "A Machine Learning-Based Surrogate Finite Element Model for Estimating Dynamic Response of Mechanical Systems". In: *IEEE Access* 11 (2023), pp. 54509–54525. DOI: 10.1109/ACCESS.2023.3282453 (cit. on p. 93).

[241] R. Moura et al. "A finite element-based machine learning framework to predict the mechanical behavior of the pelvic floor muscles during childbirth". en. In: *Expert Syst. Appl.* 250.123953 (2024-09), p. 123953. DOI: 10.1016/j.eswa.2024.123953 (cit. on p. 93).

[242] P. Di Achille et al. "Gaussian Process regressions for inverse problems and parameter searches in models of ventricular mechanics". en. In: *Front. Physiol.* 9 (2018-08), p. 1002. DOI: 10.3389/fphys.2018.01002 (cit. on p. 93).

[243] L. Liang et al. "Synergistic integration of deep neural networks and finite element method with applications of nonlinear large deformation biomechanics". en. In: *Comput. Methods Appl. Mech. Eng.* 416.116347 (2023-11), p. 116347. DOI: 10.1016/j.cma.2023.116347 (cit. on p. 93).

[244] R. Moura et al. "Patient-specific surrogate model to predict pelvic floor dynamics during vaginal delivery". en. In: *J. Mech. Behav. Biomed. Mater.* 160.106736 (2024-12), p. 106736. DOI: 10.1016/j.jmbbm.2024.106736 (cit. on p. 93).

[245] S. S. Sajjadinia, B. Carpentieri, and G. A. Holzapfel. "Bridging diverse physics and scales of knee cartilage with efficient and augmented graph learning". In: *IEEE Access* 12 (2024), pp. 86302–86318. DOI: 10.1109/ACCESS.2024.3416872 (cit. on p. 93).

[246] L. Geronzi et al. "Computer-aided shape features extraction and regression models for predicting the ascending aortic aneurysm growth rate". en. In: *Comput. Biol. Med.* 162.107052 (2023-08), p. 107052. DOI: 10.1016/j.compbiomed.2023.107052 (cit. on p. 95).

[247] L. Grassi et al. "Evaluation of the generality and accuracy of a new mesh morphing procedure for the human femur". In: *Medical Engineering & Physics* 33.1 (2011), pp. 112–120. ISSN: 1350-4533. DOI: https://doi.org/10.1016/j.medengphy.2010.09.014. URL: https://www.sciencedirect.com/science/article/pii/S1350453310002109 (cit. on p. 95).

[248] B. Mensel et al. "MRI-based Determination of Reference Values of Thoracic Aortic Wall Thickness in a General Population". In: *European Radiology* 24.9 (2014-05), 2038–2044. ISSN: 1432-1084. DOI: 10.1007/s00330-014-3188-8. URL: http://dx.doi.org/10.1007/s00330-014-3188-8 (cit. on p. 96).

[249] A. Duprey et al. "In Vitro Characterisation of Physiological and Maximum Elastic Modulus of Ascending Thoracic Aortic Aneurysms Using Uniaxial Tensile Testing". In: *European Journal of Vascular and Endovascular Surgery* 39.6 (2010-06), 700–707. ISSN: 1078-5884. DOI: 10.1016/j.ejvs.2010.02.015. URL: http://dx.doi.org/10.1016/j.ejvs.2010.02.015 (cit. on p. 96).

[250] R. Phellan et al. "Real-time biomechanics using the finite element method and machine learning: Review and perspective". In: *Medical Physics* 48.1 (2021), pp. 7–18. DOI: https://doi.org/10.1002/mp.14602. eprint: https://aapm.onlinelibrary.wiley.com/doi/pdf/10.1002/mp.14602. URL: https://aapm.onlinelibrary.wiley.com/doi/abs/10.1002/mp.14602 (cit. on p. 98).

[251] L. Liang et al. "A deep learning approach to estimate stress distribution: a fast and accurate surrogate of finite-element analysis". In: *Journal of The Royal Society Interface* 15.138 (2018-01), p. 20170844. ISSN: 1742-5662. DOI: 10.1098/rsif.2017.0844. URL: http://dx.doi.org/10.1098/rsif.2017.0844 (cit. on p. 98).

[252] K. Ghazi et al. "Instantaneous Whole-Brain Strain Estimation in Dynamic Head Impact". In: *Journal of Neurotrauma* 38.8 (2021-04), 1023–1035. ISSN: 1557-9042. DOI: 10.1089/neu.2020.7281. URL: http://dx.doi.org/10.1089/neu.2020.7281 (cit. on p. 98).

APPENDIX A

Numerical approaches for simulating cardiovascular systems: Applications, advantages, limitations and references

Table A.1: Summary of applications, advantages and limitations of different numerical techniques applied for *in silico* cardiovascular analysis

Numerical Techniques	WSS	BP	PWV	WS	Strain	Advantages	Limitations
Finite Element Method	✪	✪	✪	✪	✪	Wide implementation in computing platforms. Ability to handle complex geometries. Preferred to develop CSM models	Requires mesh generation and is more computationally demanding than FVM and FDM

Finite Volume Method	✪	✪	✪	✔	✔	Wide implementation in commercial and open-source softwares. Preferred to perform CFD simulations	It induces complexity in mesh generation and requires more interpolation algorithms
Finite Difference Method	✔	✔	✔	✔	✔	Easier to implement efficient simulations in rectangular or box-shaped computational domains	Challenging to implement in complex geometric models, particularly for geometries with curved shapes
Extended Finite Element Method	✔	✔	✔	✪	✪	Useful to study crack propagation. It does not require mesh refinement or adaptative meshes	Not recommended for crack branching problems, 3D domains and highly heterogeneous or non-linear media
0D	✖	✪	✖	✖	✖	Possibility of coupling with 3D models in order to mimic the flow resistance imposed by the downstream vasculatures	Only describes the global behaviour of the system
1D	✔	✔	✪	✖	✖	Allow quick computations of PWV	Provide incomplete descriptions of the aortic hemodynamics
2D	✔	✔	✪	✖	✔	Easier to implement than 3D simulations and quicker to compute results	As computer processing and 3D solvers have increased these simulations lost relevance
Virtual FLux Method	✪	✪	✔	✖	✖	Resorts to GPU which allows quicker computations. Enables flow calculation in curved surfaces using Cartesian grids	Challenging to implement patient-specific geometries
Regularized Lattice Boltzmann Method	✪	✪	✖	✖	✖	Designed to run on parallel architectures. Simple implementation and fixed regular grid	Stability problems in particular in heterogeneous media and thermal applications

Radial Point Interpolation Method	✔	✔	✪	✪	✪	Does not require mesh generation	Still a newly developed technology that requires further development
Smooth Particle Hydrodynamics	✔	✪	✪	✪	✪	Meshless and GPU based method which allows for quicker computations	It does not capture well flow viscous features. Hard to implement inlet and outlet boundary conditions
Machine Learning	✪	✪	✪	✪	✪	Wide range of possible applications. Regarding numerical modelling it is mainly applied to pre and post-processing tasks	Hard to implement. Highly impacted by the quality of the training data sets

WSS – Wall Shear Stress; **BP** – Blood Pressure; **PWV** – Pulse Wave Velocity; **WS** – Wall Stress; ✪ – Preferred; ✔ – Adequate but not preferred; ✖ – Not adequate;

Table A.2: Studies focused on analyzing the biomechanical environment of healthy and diseased aortas. n = 31 articles.

Work	Approach	Solver	Anatomy	Boundary Conditions	Flow		Wall	Main Remarks	Aim of the work	Grade
[158]	CSM (XFEM)	Abaqus	AD (I)	LP; Axial DF	—	—	HGO	The propagation of AD is more likely to occur in larger and deeper tears	Study the effect of tear orientation on AD progression	Low
[56]	CFD (FEM;FVM)	SimVascular; Fluent	AAA (PS-CT)	I: CV (0.25 $m\,s^{-1}$); O: 0P	L	N	—	Downstream of the abdominal bifurcation, recirculation zones, supraphysiological WSS and long particle residence time were found	Assess geometrical parameters influence on AAA and its branches hemodynamics	Low
[176]	CFD (FVM)	Fluent	Coarction (I)	I:FR ; O:WM	L	MM-E-E	—	One-phased and MM-EE rheological models produced similar results for high velocity regimens	Investigate the influence of coarction on aortic hemodynamics	Low
[164]	FSI (FEM;FVM)	Ansys	Aortic Valve (I)	I:PoT ; O: —	L	N	NH ; S-VK	High bending stiffness causes a reduction in opening area of the AV; Low bending stiffness may induce flapping oscillations	Assess the effect of the leaflets bending stiffness on FSI simulation	Low
[66]	FSI (FEM;FVM)	Ansys	ATAA (PS-MRI)	I:VF ; O: FR & WM	L	C	LEI	Stiffer aortas usually present abnormal WS distributions; Increased peripheral resistance is correlated with increase in WSS	Evaluate the hemodynamic and structural changes in ATAA behaviour for different wall material properties	High

[22]	FSI (FEM)	COMSOL	ATAA (PS-Echo)	I:FR ; O:CP	L	N	HGO	Significant differences in wall strain, blood pressure, WSS and turbulence were found between normative and hypertensive loading	Analysis of ATAA biomechanics under hypertensive and normative conditions	Low
[115]	CSM (FEM)	House-hold code	ATAA (I)	LP (120 – 160 mmHg); PrS ; DF	—	—	D	The stress field in MFS patients was mainly circumferential oriented, almost uniform and presented higher WS magnitude	Numerically characterize ATAA biomechanics in MFS patients	Low
[172]	CSM (FEM)	Ansys	AAA (PS-CT/MRI ; I)	LP (120 mmHg)	—	—	N-H ; R-V	PWS increased with maximum diameter, asymmetry and turtuosity and decreased with wall thickening	Evaluation of the influence of different geometrical features on PWS	Low
[57]	CFD (FVM)	CFX	AD (PS-CT)	I:FR ; O:PoT	$k-\epsilon$	N	—	WSS in the FL were significantly higher; Peak vortical flow appears at aortic tear initiation points	Further investigate the pathogenesis and progression of AD	Low
[61]	CFD (FVM)	Star-CCM +	Aortic Arch (PS-CT)	I:VP ; O:FR	L	C-Y	—	The flow on the aortic arch presented higher velocity near the inner wall, and clockwise helical and recirculating flow	Investigate the hemodynamics in the aortic arch	Low
[149]	CFD (FVM)	Fluent	AD (PS-CT)	I:PoT ; O:PoT	L	N	—	Pressure and WSS seem to be well correlated with tear location	Evaluate the influence of tear location and tear size on AD hemodynamics	Low

[58]	CFD (FVM)	Fluent	TAA(PS-CT)	I: CV (5 L/min); O:WM	RNG $k-\epsilon$	N	—	Abnormal WSS was correlated with intimal layer (mal)functioning; High OSI was correlated with regions of high probability of rupture	Assess the hemodynamic variations between healthy and TAA patients	Low
[27]	CFD (FVM)	—	TS (PS-MRI)	I:FR ; O:CP	L	Q	—	Anatomical variations contributed to increased WSS and recirculation zones where the n-N effects were significant	Assess how anatomical changes of TS patients influences aortic hemodynamics	Low
[180]	CFD (FEM)	CRIMSON	AD (I)	I:FR ; O:WM	L	N	—	AD induces increased blood pressure; The FL location is only impactful on blood pressure and velocities on the inner curvature	Evaluate AD hemodynamic alterations associated with anatomical variations	Low
[182]	FSI (FEM)	Abaqus	AD (I)	I:FR ; O:PoT	EM	N	LEI	Distally to the flap, lower velocities and higher flow turbulence were found	Assess the hemodynamic and structural features on a flap blood interaction	Moderate
[173]	CFD (FVM)	CFX	TAA (PS-MRI)	I:FR ; O:FR ; WM	$k-\omega$ SST	N	—	Vortices were formed at the entrance of the SA which originated flow turbulence and recirculation zones	Study the hemodynamics on SA	High
[174]	CFD (FVM)	Fluent	Abdominal Stenosis (I)	—	L	N	—	As the blockage increases the mean flow velocity and WSS magnitude also increases; The changes were significant for arterial blockage above 50%	Evaluate the hemodynamics on abdominal stenosis of different blockage degrees	Low

[171]	FSI (FEM;FVM)	Ansys	AAA (I)	I:PoT ; O:CP	L	N	LEI	AAA hemodynamics were characterized by the formation of two vortex which were appointed as the dominant aspect of fluid dynamics	Study the influence of vessel dilation and aspect ratio on the hemodynamics	Low
[179]	FSI (FEM)	ADINA	Sinus of Valsava (PS-MRI)	I:FR ; O:PoT	L	N	LEI	Vortices are formed in the LV and travel towards aorta; Higher pressure and WSS were found in the aorta	Compute the hemodynamics inside the LV and aortic sinuses	High
[159]	FSI (RLBM;VFM)	Own code	Sinus of Valsava (I)	I:FR ; O:PoT	LES	N	—	The formation of two vortices near the aortic root was evidenced and correlated with high WSS and diminished blood supply to the myocardium	Assess WSS distributions on sinus of Valsava patients	Low
[156]	CFD (FDM)	—	TA (PS-CT)	I:FR ; O:0P	L	N	—	All the tested geometries produce a swirled flow on the TA	Investigate effect of aortic torsion on the blood flow	Low
[178]	FSI	Abaqus	BAV (I)	I:PoT; O:PoT	L	N	LEI	BAV caused more turbulence near the aortic root, and higher velocity and WSS	Evaluate the influence of BAV on blood flow	Moderate
[153]	FSI (FEM;FVM)	Ansys	AD (PS-CT)	I:VF ; O:FR	L	N	RV	In BAV patients an intrinsic disturbed blood flow which contributes to an asymmetric and elevated WS distribution was evidenced	Study the main differences in hemodynamics and WS between BAV and TAV patients	Low

[21]	CFD (FVM)	Fluent	AD (PS-CT)	I:FR ; O:0P	L	N	—	The pressure imbalance between the TL and FL is responsible for the delamination of aortic wall	Elucidate the mechanisms of longitudinal propagation of AD	Low
[151]	CSM (FEM)	Abaqus	DTAA (PS-CT)	LP (120 mmHg)	—	—	RV	Positive correlation between PWS and aneurysm growth	Presented new correlations between PWS and aneurysm growth	Low
[145]	FSI (FEM;FVM)	Abaqus ; Fluent	AAA (PS-CT)	I: FR ; O: PoT	L	N	RV	Aneurysm induced WSS magnitude increase (3 fold) and contributed to disturbed flow patterns	Evaluate the differences in hemodynamics between healthy subjects and AAA	Low
[69]	FSI (FEM;FVM)	Ansys	Stenosis (PS-CT)	I: FR ; O: PoT	L	PL	LEI	Wall deformation was low but still produced significantly different numerical results	Investigate the effects of pulsatile flow and flexible walls on aortic flow	Low
[177]	FSI (FEM;FVM)	Ansys	Aorta (PS-MRI)	I:FR ; O:WM ; EP	$k-\epsilon$	N	LEI	The model accurately estimated flow patterns presenting close agreement with MRI data for lower velocity regimens; WSS is highly influenced by wall motion	Evaluate the flow dynamics on healthy aorta, in particular WSS distributions	High
[76]	CFD (FVM)	CFX	AD (PS-CT)	I:FR ; O:0P	$k-\omega$	Q	—	Disturbed flow and strong recirculation within both the TL and FL were found	Study the flow in AD and assess the crucial features to aneurysm dilation	Low

[175]	CFD (FVM)	Fluent	Stenosis; Coarc-tion (I)	I:FR ; O:—	$k-omega$	N	—	The combination of coarction and stenosis highly influenced WSS and pressure distributions and induced the formation of secondary flow patterns	Study the effect of pulsatile flow on hemodynamics of stenosed and coarcted aortas	Low
[62]	CFD (FVM); CSM (FEM)	CFX; VAS-COPS	AAA (PS-CT)	I:FR ; O:PoT	L	C-Y	—	Significant hemodynamic and structural differences were found between healthy subjects and AAA patients	Study hemodynamic and structural features of AAA	Low
[68]	CFD (FVM)	Fluent	Aortic Arch (I)	I:FR; O:FR	L	PL	—	Modelling the aortic root motion influenced the numerical results; Intimal thickening occurred in low OSI and WSS regions	Show the potential of numerical tools to recreate the hemodynamics of the aortic arch	Low

Table A.3: Works on numerical models applied to study aortic all microstructure. n = 14 articles.

Work	Approach	Solver	Anatomy	Boundary Conditions	Flow		Wall	Main Remarks	Aim of the work	Grade
[127]	FSI (FEM)	Abaqus	TA (PS-MRI)	I:FP; O:CP	L	N	O; HGO	Geometrical factors highly influence the hemodynamic patterns; Wall compliance was the dominant factor for the overall aortic mechanical behaviour	Assess the viability of using *in vitro* silicone models to mimic vascular tissue	Moderate
[119]	CSM (FEM)	—	AD (RVol)	Fluid injection	—	—	N-H ; F	The maximum pressure prior to tearing is highly dependent on local geometry and material properties	Assess which location of the aortic wall is more propense to dissect	Low
[126]	CSM (FEM)	Abaqus	AD (RVol)	UT	—	—	HGO	Glucose treated elastin presented increased peeling force, energy release rate and interlamellar strength	Evaluate the effect of elastin glycation on AD progression	Moderate
[185]	CSM (FEM)	Own code	AD (RVol)	UT	—	—	LEI	In biaxial conditions the rupture is likely to occur in any direction; Organization and fiber properties are the main contributors to aortic strength	Assess the relevant changes in aortic wall microstructure during rupture	Low
[189]	CSM (FEM)	Abaqus	ATAA (PS-CT)	DF ; LP (80 mmHg)	—	—	HGO	Extensional stiffness (higher in the ascending aorta) and high rupture risk were statistically correlated	Develop a technique to non-invasely identify aortic wall mechanical properties	High

[32]	CSM (FEM)	—	AD (RVol)	DF ; LP (80 – 600 mmHg) ; Tor	–	—	HGO	AD development is consequence of in-plane shear stresses created by the heterogeneity of aortic wall properties and FL propagation occurs mainly due to the secondary blood flow	Study the mechanisms that explain the beginning and progression of AD	Low
[33]	CSM (FEM)	—	Aortic Media (RVol)	BT	—	—	Y ; NH	The developed model captured the overall response only for physiological pressure ranges	Present a new micromechanically based wall constitutive model	Moderate
[138]	CSM (FEM)	MatLab	Aorta (RVol)	Axial DF	—	—	N-H ; LEI	Collagen fibers present higher strength and stiffness but lower failure stretch when compared to elastin; Collagen breakage is the governing tissue failure mechanism	Study the microstructural response of the aortic wall to rupture	Moderate
[184]	CSM (FEM)	MatLab	Aorta (RVol)	Axial DF	—	—	N-H ; LEI	Collagen fibers oriented in loading direction were more solicited	Study the response of aortic wall microstructure under UT conditions	Low
[125]	CSM (FEM)	Own-Code	Aorta (RVol)	LP (100 – 160mmHg)	—	—	HGO	Elastin fibers have a dominant role for lower strains	Study microstructure components of the aortic wall under hypertensive conditions	Low

[183]	FSI (FEM)	Abaqus	AAA (PS-CT)	I:FR ; O:RF	L	N	HI	The materials presented similar mechanical properties to vascular tissue; PWV results were consistent with FSI simulation findings	Assess if certain phantom materials are good replicates of vascular tissue	Moderate
[186]	FSI (FVM)	ACE +	TA (PS-MRI)	I:FR ; O:FR	L	N	LEI	The proposed method may be used to evaluate if the considered material parameters are suitable	Present a new method for arterial wall compliance assessment	Low
[120]	CSM (FEM)	Matlab	AS (I)	BT	—	—	2D F	Ascending aorta (more compliant) and AS tissue presented significant different material properties	Evaluate ATAA and AS material properties differences	Moderate
[148]	CSM (FEM)	—	AAA (PS-CT)	LP	—	—	LEI	Aneurysmal growth was correlated with elevated aortic stiffness	Evaluate the aortic microstructure alterations promoted by abnormal WS distributions	Low

Table A.4: Works regarding improvements or development of diagnosing metrics or techniques. n = 16 articles.

Work	Approach	Solver	Anatomy	Boundary Conditions	Flow		Wall	Main Remarks	Aim of the work	Grade
[192]	CSM (FEM)	COMSOL	AD (I)	Specific Voltage	—	—	—	The use of Bayesian approach outperformed regular multi-sensor impedance cardiography methodology	Intended to simulate the propagation of trans-thoracic electric pulses	Low
[124]	CSM (FEM)	—	ATAA (PS-CT)	LP (80 – 120 mmHg) ; PrS	—	—	HGO	The developed ML tool outperformed other rupture risk estimation methods	Identify the locations where the aortic rupture is more likely to occur	Low
[19]	CFD (FVM)	Fluent	ATAA (PS-CT)	I:CV ; O:WM	L	C	—	A combination of hemodynamic, wall parameters and circulating biomarkers may be a suitable method to assess the risk of acute complications	Investigate the relation between WSS and aortic wall strain and the presence of biomarkers	Low
[194]	CFD (FVM)	Open-FOAM	AAA (I)	I:FR ; O: 0G	L	N	—	Laser Doppler velocimetry is the preferred technique to estimate WSS	Evaluate the gold-standard method to estimate WSS	Moderate
[28]	CFD (FVM)	Open-FOAM	AAA (I)	I: FR ; O: 0G	RANS	N	—	Magnetic resonance velocimetry captured better the flow turbulence and better predicted WSS when compared to WSS	Present validated numerical descriptions of AAA blood flow to improve MRV efficiency	Moderate
[163]	CFD (2D)	—	Aorta	I: FR ; O: Imp	L	K-V	LEI	The developed model found good agreement with *in vivo* data and outperformed regular rigid wall simulations	Develop a validated realistic model of the aorta that is able to evaluate PWV	High

[190]	CFD (FVM)	—	AS (I)	I:CV ; O:—	DNS	N	—	Murmurs source location is not correlated with stenosis degree and is not coincident with stenosis location	Enhance auscultation by studying post-stenosis hemodynamics	Low
[154]	CFD (FEM)	MatLab	Aorta (PS-MRI)	I: PoT; O: PoT	L	N	—	The circumferential component of WSS presented good correlation with disturbed flow	Implement a method to estimate WSS different components	Low
[18]	CFD (FVM)	Fluent	ATAA ; AI (PS-MRI)	I:VF ; O:FR ; WM	L	C	—	Inflow jet impingement against the aortic wall creates a non-homeostatic WSS distribution	Study the role of altered hemodynamics on aortic rupture risk	High
[162]	CFD (1D)	—	AAA	I:FR ; O:RF	L	N	LEI	Aortic compliance alterations may be a good monitoring metric for diagnosing aneurysms which can be estimated via ultra-sound measurements	Develop a new diagnosing technique of aneurysms based on 1D modelling	Moderate
[193]	FSI (FEM ; FVM)	Abaqus ; Fluent	BAV (PS-CT)	I: FR ; O:WM	L	N	P	BAV patients showed increased WSS and WS when compared to TAV patients	Evaluation of new ascending aortic dilatation risk predictors	Low
[191]	CFD (2D)	LS-Dyna	AS	I:PoT ; O:0P	L	N	LEI	Systolic transvalvular pressure gradient is useful to evaluate the degree of stenosis	Improve the diagnosis efficiency of aortic stenosis	Low
[155]	CFD (FEM)	MatLab	Aorta (PS-MRI)	I: PoT ; O: PoT	L	N	—	Wall deformation highly impacted the WSS magnitude	Develop a new technique to evaluate WSS distributions in the aorta	Low

[121]	CFD (0D)	Excel	CS	I: PoT; O:R	—	—	F	The proposed methodology presented good estimation when constant compliance was applied	Develop a new technique to measure cardiac stroke volume	Low
[151]		Abaqus	DTAA (PS-CT)	LP (120 mmHg)	—	—	RV	Positive correlations between PWS and aneurysm growth were found	Study the rupture of aneurysms	Low
[195]	CSM (FEM)	Abaqus	AAA (I)	DF	—	—	O	The numerical results accurately predicted the sites of rupture	Simulate the rupture in aneurysms using *in silico* and *in vitro* experiments	Moderate

Table A.5: Contributions that aimed to augment numerical modelling of healthy and diseased aortas. n = 38 articles.

Work	Approach	Solver	Anatomy	Boundary Conditions	Flow		Wall	Main Remarks	Aim of the work	Grade
[52]	FSI (FEM)	SimVascular	ATAA (PS-CT)	I:FR ; O:WM	L	N	N-H	The developed method contributed to improve convergence	Develop a novel method for separately mesh the fluid and solid domains	Low
[53]	FSI (FEM)	SimVascular	TA (PS-MRI)	I: VP-MRI ; O: WM	L	N	LEI	WSS presented significant differences for different inlet flow wave forms	Evaluate the numerical results sensitivity to the inlet flow-rate waveform	Low
[60]	CFD (FVM)	OpenFOAM	ATAA (PS-CT)	I:FR ; O:PoT	$k-\omega$ SST	C-Y	—	Turbulence and n-N behaviour of blood is not relevant to be modeled in ATAA	Evaluate the relevance of modelling turbulence and n-N behaviour	Low
[79]	FSI (FEM)	SimVascular	AD (PS-CTA)	I: VP ; O: WM ; PrS ; EP	L	N	N-H	The inclusion of two-way FSI, PrS and adequate wall and flap material properties improved the numerical results agreement with *in vivo* data	Assess the relevance of modelling realistic wall and dissection flap deformation on AD	High
[54]	CFD (0D)	SISCA	AAA	I:PoT; O:-PoT	L	N	—	Certain estimated model parameters presented significant differences between healthy and diseased subjects	Estimate coefficients of 0D models using ARMA approach which may assist on clinical diagnosis	Low
[63]	CFD (FVM)	Fluent	ATAA (PS-MRI)	I:VF; O:FR ; WM	L	C-Y	—	ROM and RBF mesh morphing allow to explore new results interactively and almost in real time	Assess the relevance of using mesh morphing and ROM techniques	Low

[14]	CSM (FEM)	Abaqus	AAA (I)	LP (120 mmHg); DF	—	—	HGO	Intima present an early exponential stiffening which contributed to the load-bearing of the aortic wall	Evaluate the intima layer load-bearing effect on aged aortas	Low
[170]	CSM (RPIM)	—	AAA (I)	LP	—	—	LEI	FEM and RPIM models produced similar results	Test the viability of using RPIM methods	Low
[67]	FSI (FEM; FVM)	Ansys	Coarction (PS-MRI)	I: VP; O:OP	L	C	LEI	FSI simulations increase in relevance for decreased wall stiffness	Assess the relevance of resorting to FSI simulations	High
[169]	CFD (SPH)	—	AAA (PS-CT)	I:VP ; O:PoT ; DF	L	N	—	Moving wall simulations produced more realistic hemodynamics	Present a novel tool to predict AAA hemodynamics	Low
[152]	CFD (FVM)	—	ATAA (PS-MRI)	I:VP ; O:FR	L	N	—	Stroke volume and cardiac cycle duration presented significant influence on the numerical results	Explore the sensitivity of the blood-to-wall LDL transfer to inlet BC	Low
[17]	CFD (FVM)	Fluent	ATAA (PS-MRI)	I:VP ; O:WM	L	N	—	Significant hemodynamic changes appeared only for a 60% increase in aneurysm diameter	Address the effects of geometrical changes on hemodynamics	Low
[55]	CFD (SPH)	—	AAA (I)	I:FR ;O:PoT ; DF	L	N	—	The model was able to accurately reproduce the biomechanical behaviour of the aorta	Present a novel technique to perform FSI simulations using SPH and moving BC	Low
[201]	FSI (FEM)	ADINA	Aorta (I)	I:FR ; O: 2D	L	N	LEI	The developed BC is able to accurately model pulse wave reflection	Present a new model to apply as an outlet BC	Low

[200]	CFD (FEM)	Open-FOAM	Aorta (PS-MRI)	—	L	N	—	The presented technique outperformed classical CFD approaches	Present a inverse method to estimate *in vivo* BC	Moderate
[123]	FSI (FEM ; FVM)	Ansys	ATAA (PS-MRI/CT)	I:FR ; O:WM	L	N	HGO	Both WSS and WS presented significant differences between the simplest approaches and FSI models	Assess if FSI formulation is more accurate than CFD or CSM analysis	Low
[80]	CFD (FVM)	Star-CCM +	SA (PS-CT)	I:FR ; O:FR	L	N	—	For modelling SA assuming pulsatile, laminar and n-N flow are key factors	Provide insights into SA modelling adequate numerical settings	Low
[122]	CSM (FEM)	Abaqus	TA (I)	LP (10 – 16 kPa)	—	—	HGO	FEM models can successfully train ML tools with considerable reduction in computational time	Estimate the reference configuration of human TA resorting to ML tools	Low
[113]	FSI (FEM ; FVM)	Ansys	Aorta (PS-CT)	I:FR ; O:FR	L	N	NH	Rigid wall simulations overestimate pressure and WSS driven metrics	Assess how the intramural pressure changes with wall stiffness	Low
[114]	FSI (FEM)	Abaqus ; Fluent	Coarction (PS)	I:FR ; O:FR; WM	L	N	PH	Automated mesh generation can be useful to reduce the reporting time	Reduce the computational effort of grid generation	Low
[64]	FSI (FEM ; FVM)	Ansys	AD (PS-CT)	I:FR ; O:WM	$k-\omega$ SST	C-Y	RV	FSI models have increased accuracy but for AD the required computational time can be excessive	Assess the hemodynamic changes and the stresses on a flap blood interaction	Low
[150]	FSI (FEM ; FVM)	Abaqus ; Fluent	Coarction (I)	I:PoT ; O:RF	L	N	MR	Numerical dissipation and diffusion are mainly ruled by spatial and time discretization	Study the effects of coarction on pulse wave reflection	Low

[139]	CFD (FVM)	Open-FOAM	Aorta(I)	I: FR ; O:—	DNS	N	—	No significant changes were found using DNS for turbulence modelling	Study the impact of modelling the turbulence of blood flow	Low
[204]	CFD (1D)	—	DTA	I:FR ; O:WM	L	N	—	PWV, total arterial resistance and compliance were calculated and validated against MRI data	Evaluate the application of 1D modelling on cardiovascular medicine	High
[160]	CFD (0D)	—	AV	—	—	—	—	No relevant conclusion were presented besides the fact that it was suggested as realistic	Mathematical model that recreates AV dynamics	Low
[112]	CFD (1D)	—	Aorta	I:FR ; O:WM	L	N	—	Numerical results closely reproduced velocity, PWV and area changes	Evaluate the efficiency of using 1D models to estimate PWV	High
[198]	CFD (FVM)	CFX	Coarction (PS-MRI)	I:VP ; O:FR ; PoT	LES	N	—	TKE may be a good indicator of abnormal or pathophysiological flow condition	Compare the results of CFD and MRI data	High
[178]	FSI (FEM)	Abaqus	BAV (I)	I:PoT ; O:PoT	L	N	CFN	The CSM simulation overestimated by 30% the coaptation area, 55% the contact pressure and 170% the closure time	Evaluate the difference of modelling AV with CSM or FSI	Low
[156]	CFD (FDM)	—	TA (SemiPS-CT)	I:FR ; O:0P	L	N	—	All the tested geometries produce a swirled flow somewhere on the TA	Investigate the blood flow in TA focusing on the effect of torsion	Low
[146]	CSM (FEM)	Abaqus	AAA (PS-CT)	LP (120 mmHg)	—	—	PH	Using patient-specific parameters had significant impact on the results	Evaluate the impact of considering patient-specific material properties	Low

[157]	CFD (FDM)	—	Aorta (I)	I:VP ; O:PoT	L	N	—	Under transient conditions inlet and outlet BC significantly altered the numerical results	Assess the sensitivity of numerical results to the chosen BC	Low
[203]	CFD (1D)	MatLab	Aorta	VP ; PoT	L	N	—	The developed model presented good agreement with *in vivo* data	Novel method to estimate WSS distribution	High
[147]	CFD (FVM)	Fluent	Abdominal aorta (I)	I: CV ($0.234\ \mathrm{m\,s^{-1}}$) ; O:—	$k-\epsilon$	N;C-Y	—	Small differences in WSS were found between different rheological models	Explore the hemodynamics on the bifurcation of the abdominal aorta	Moderate
[110]	CFD (1D)	—	Aorta	I:FR ; O: FR ; PoT	L	N	—	Energy losses at bifurcations had a secondary effect on the blood flow and wall viscoelasticity might have a significant effect on PWV	Explore the effects on PWV of energy loss and fluid inertia	Moderate
[81]	CFD (FEM)	Fidap	AAA (I)	I:FR ; O:0G	$k-\epsilon$	n-N	—	It is relevant to model n-N behaviour and turbulence in AD	Evaluate the influence of pulsatile, turbulent and n-N flow	Low
[197]	CFD (FEM)	Fidap	AAA (I)	I:FR ; O:0G	$k-\epsilon$	n-N	—	High blood pressure and turbulence were postulated as contributors to aneurysm rupture	Same as [81]	Low
[161]	CFD (0D)	—	CS	—	—	—	—	The model was able to simulate hemodynamic waveforms at different heart frequencies and heart diseases	Developed a new numerical model of the cardiovascular system	High

[111]	CFD (1D)	—	AV	PoT	L	N	—	Blood pressure, PWV and wall properties presented good agreement with theory and empirical data	Develop a model that estimated the hemodynamics of the AV	Low

0G- Zero Gradient; **0P**- Zero Pressure; **AoI**- Aortic Insufficiency; **AS**- Aortic Stenosis; **BT**- Biaxial Tension; **C**- Carreau; **CFN**- Collagen Fiber Network model; **CP**- Constant Pressure; **CS**- Cardiovascular System; **CV**- Constant Velocity; **C-Y**- Carreau-Yasuda; **D**- Demiray; **DF**- Displacement Field; **EM**- Empirical Model; **EP**- External Pressure; **FR**- Flow Rate; **F**- Fung exponentially stiffening material; **HGO**- Holzapfel-Gasser-Ogden; **HI**- Hyperelastic Isotropic; **iFR**- instantaneous Wave-free Ratio; **I**- Idealized; **Imp**- Impedance; **K-V**- Kelvin-Voigt; **L**- Laminar; **LDL**- Low-Density Lipoprotein; **LEI**- Linear, Elastic and Isotropic; **LP**- Luminal Pressure; **LV**- Left Ventricule; **MFS**- Marfan Syndrome; **MM-EE**- Multi-Phase Euler-Euler model; **M-R**- Mooney-Rivlin; **MRV**- Magnetic Ressonance Velocimetry; **n-N**- non-Newtonian; **N**- Newtonian; **N-H**- Neo-Hookean; **O**- 3rd order Ogden model; **OSI**- Oscillatory Shear Index; **PH**- Polynomial Hyperelastic constitutive model; **PL**- Power-Law; **PoT**- Pressure over Time; **PrS**- Prestress; **PS**- Patient-Specific; **Q**- Quemada; **R**-Resistance; **RBF**-Radial Basis Function; **RF**-Reflection Free; **RV**-Raghavan and Vorp; **RVol**- Representative Volume; **SA**- Saccular Aneurysms; **S-VK**- Saint-Vennant Kirchhoff; **TA**- Thoracic Aorta; **Tor**- Torsion; **TKE**- Turbulent Kinetic Energy; **TS**- Turner Syndrome; **UT**- Uniaxial Tension; **VP**- Velocity Profile; **WM**- WindKessel Model; **Y**- Yeoh Model